Experimental study on tungsten EUV spectroscopy in LHD for high-temperature plasma diagnostics

LIU Yang

Doctor of Philosophy

Department of Fusion Science
School of Physical Sciences
SOKENDAI (The Graduate University for Advanced Studies)

Experimental study on tungsten EUV spectroscopy in LHD for high-temperature plasma diagnostics

LIU Yang

Doctor of Philosophy

Department of Fusion Science
School of Physical Sciences
The Graduate University for Advanced Studies

2018 School Year

Abstract

ITER (International Thermonuclear Experimental Reactor) under construction in France is a next-generation tokamak device aimed at carrying out burning plasma experiments based on D-T (deuterium-tritium) nuclear reaction and the first operation is now scheduled on 2025. Materials for plasma-facing components (PFCs) in ITER must have a good capability of tolerating an extremely large thermal heat load, in addition to capabilities of reducing the erosion and tritium retention rates because a long-pulse discharge with fusion output of 500MW is planned. Then, tungsten is used instead of carbon material as the most suitable material for the PFCs in the ITER tokamak instead of carbon materials which have been used for many years in toroidal devices. However, the line radiation loss from tungsten ions is huge because of the large atomic number. Once the tungsten concentration exceeds a certain threshold level in the core plasma, the plasma performance is significantly degraded. In addition, heavy impurities such as tungsten tend to accumulate in the central plasma region due to the neoclassical effect. In the ITER operation, therefore, the tungsten density, n_W, must be maintained at a low level against the electron density, n_e, e.g., $n_W/n_e<10^{-5}$. The tungsten transport study is extremely important for controlling the tungsten accumulation in the plasma core and the tungsten influx in the plasma edge. As a matter of course, development of the tungsten diagnostic method is also important. At present, however, understanding of tungsten spectra for a quantitative analysis on the tungsten ion is entirely insufficient, while the tungsten spectrum has been qualitatively understood based on several experimental and theoretical studies which have been carried out so far. Based on the physics requirement mentioned above, study on tungsten spectroscopy has been initiated in Large Helical Device (LHD). The electron temperature range of ITER divertor, scrape-off layer (SOL) and edge plasma is about the same as that of LHD neutral-beam-heated plasmas. Therefore, the present study on tungsten spectroscopy in LHD can give valuable information for the edge diagnostics of ITER.

Tungsten spectra have been observed in LHD by injecting a coaxial tungsten pellet to identify the line emissions in extreme ultraviolet (EUV) range of 10-500 Å. All the tungsten spectra in the present study have been measured in the neutral-beam-heated discharge using two EUV spectrometers working in wavelength ranges of 10-130 Å and 50-500 Å, respectively. A lot of line emissions from low-ionized tungsten ions of W^{4+}, W^{6+} and W^{7+} are observed for the first time in the toroidal device in addition to line

emissions from highly ionized tungsten ions of W^{41+} - W^{45+}. Measured line emissions are carefully identified based on the NIST (National Institute of Standards and Technology) database. Wavelengths of the line emissions determined in the present study show a good agreement with the NIST database. The result is summarized in a table with information on blended lines which is evaluated from the shape and peak position in radial profiles of the line emissions.

Up-down asymmetry of the tungsten line emission has been examined in LHD. For the purpose two space-resolved EUV spectrometers working in wavelength ranges of 10-130 Å and 30-500 Å are utilized to observe the full vertical profile of tungsten line emissions by simultaneously measuring upper- and lower-half plasmas of LHD, respectively. The radial profile of local emissivity is reconstructed from the measured vertical profile in the overlapped wavelength range of 30-130 Å. The up-down asymmetry is then examined against the local emissivity profile of WXXVIII existing in the pseudo-continuum spectrum called unresolved transition array (UTA). The result shows a nearly symmetric profile, suggesting a good availability in the present diagnostic method for the impurity asymmetry study. Although the up-down symmetry has been observed in several tokamaks for medium- and high-Z impurities, the present result may indicate a difference in the neoclassical transport, in particular, effect of ∇B, between tokamak and LHD. Through the present result, it is evidently confirmed that the tungsten profile data obtained in LHD can be analyzed as a function of magnetic surfaces.

The UTA spectra observed in wavelength range of 15 Å to 70 Å have been studied to determine the spectral component at unit wavelength interval, e.g. $\Delta\lambda$=0.11Å at 30Å and $\Delta\lambda$=0.22 Å at 50Å). At first, the UTA line intensity is analyzed against central electron temperature at temperature recovery phase after the pellet injection to examine the presence of blended lines. Next, vertical profiles measured with two space-resolved EUV spectrometers are analyzed against electron temperature profiles for further precise investigation of the UTA spectra. For the analysis the local emissivity profile is reconstructed from the measured vertical intensity profiles with Abel inversion method based on magnetic surface structures calculated by VMEC (Variational Moments Equilibrium Code) code. It is then possible to investigate the ionization stage of tungsten ions composing the UTA. As a result, it is found that several wavelength intervals are composed of only a single ionization stage, e.g. 29.47-30.47 Å (W^{26+}), 30.69-31.71 (W^{25+}), 32.16-33.32 Å (W^{24+}), 47.94-48.15 Å (W^{24+}), 48.81-49.03 Å (W^{26+}) and 49.24-49.46 Å (W^{27+}). These wavelength intervals are applicable to the tungsten diagnostics. The result of the line component analysis on the tungsten UTA is summarized in tables with

information of blended lines for all wavelength intervals at wavelength ranges of 27.20-33.32Å and 47.72-52.79Å.

Based on the result mentioned above, density profiles of the W^{24+}, W^{25+} and W^{26+} ions are analyzed from the radial profile measured at wavelength intervals of 32.16-33.32, 30.69-31.71 and 29.47-30.47 Å, respectively. In order to evaluate the ion density, a photon emission coefficient for the W^{24+}, W^{25+} and W^{26+} ions is calculated using a collisional-radiative (CR) model in which a principal quantum number up to n = 7 and 7515-13772 J-resolved fine-structure levels are taken into account for one ion. The tungsten density profiles of W^{24+}, W^{25+} and W^{26+} ions are thus obtained from the local emissivity profile and the photon emission coefficient. The peak density of these tungsten ions is compared between the present CR model and CL version of ADAS (Atomic Data and Analysis Structure) code. It is found that the tungsten density calculated with CR model is roughly five times bigger than the tungsten density estimated from the injected pellet size, while the density calculated from the ADAS code is fairly close to the density estimated from the pellet size, i.e. difference within two times. A cascade process from higher excited levels may enhance the photon emission coefficient in the ADAS code calculation and resultantly the tungsten density calculated with the ADAS code is smaller. A total tungsten ion density, n_W, in the vicinity of $\rho = 0.7$ where the W^{24+} ion locates is also estimated from the W^{24+} ion density based on the fractional abundance in ionization equilibrium calculated with ADAS code.

As the supplement study, effects of neutrons and γ-rays on charge-coupled device (CCD), which is widely used as a detector of vacuum spectrometers in fusion devices, have been examined at deuterium plasma experiments in LHD. Totally 3.7×10^{18} neutrons have been yielded with energies of 2.45 MeV (D-D neutron) and 14.1 MeV (D-T neutron) during the deuterium experiment over four months. Meanwhile, the γ-rays are also radiated from plasma facing components and laboratory structural materials in a wide energy range, i.e., 0.01-12.0 MeV, through the neutron capture. It is well known that these neutrons and γ-rays bring serious problems to the CCD system. Then, several CCDs of vacuum ultraviolet (VUV) / EUV / X-ray spectrometers installed at different distances from LHD are examined to study the effect of neutrons and γ-rays. The result indicates that the CCD noise count per neutron, N_{CCD}/S_n, decreases as a function of distance from CCD to LHD plasma center, L, e.g. $N_{CCD}/S_n=10^{-6}$ counts/n at L=7m and $N_{CCD}/S_n=5\times10^{-8}$ counts/n at L=10.5m. An additional CCD placed in a special shielding box made of 10 cm thick polyethylene containing 10% boron and 1.5 cm thick lead is also used for the detailed analysis. As a result, it is found that the CCD has no damage in the present neutron yield of LHD. The data analysis of CCD signals in the shielding box shows that the background

signal noise caused by the γ-ray is a little smaller than that caused by the neutron, i.e., 41% from γ-rays and 59% from neutrons. It is also found that the noise can be partly removed by an accumulation of CCD frames or software programming.

Contents

1. Introduction.....1

1.1 Magnetically confined fusion.....1

1.2 Impurities in fusion plasma.....3

1.3 Large Helical Device and spectrometers.....7

1.4 Objective and structure of the thesis.....11

References.....13

2. Observation of tungsten line emissions in wavelength range of 10-500 Å.....17

2.1 Introduction.....17

2.2 Experimental setup.....18

2.3 Experimental results.....19

2.4 Summary.....30

References.....31

3. Up-down asymmetry investigation of tungsten distribution using two EUV spectrometers.....33

3.1 Introduction.....33

3.2 Experimental setup.....34

3.3 Experimental Results.....37

References.....41

4. Component investigation of ionization stages on tungsten UTA spectra.....43

4.1 Introduction.....43

4.2 Experimental setup.....46

4.3 Wavelength calibration of EUV spectrum.....48

4.4 Component investigation of UTA spectra based on electron temperature.....51

4.4.1 UTA spectrum at 15-70 Å.....51

4.4.2 Analysis of tungsten UTA at 15-45 Å.....58

4.4.3 Analysis of tungsten UTA at 45-70 Å.....60

4.5 Component investigation of UTA spectra based on radial profile measurement...63

4.5.1 Precise re-evaluation of tungsten UTA lines at 27-34 Å using radial profiles.....63

4.5.2 Precise re-evaluation of tungsten UTA lines at 47-53 Å using radial profiles.....69

4.5.3 Comparison of radial profiles of UTA lines between two different wavelength ranges of 27-34 Å and 47-53 Å.....73

4.6 Summary.....76

References.....77

5. Density evaluation of tungsten W^{24+}, W^{25+} and W^{26+} ions using unresolved transition array at 27-34 Å.....79

5.1 Introduction.....79

5.2 Experimental results.....80

5.2.1 Typical discharge with tungsten pellet injection.....80

5.2.2 Calculation of photon emission coefficients.....86

5.2.3 Error estimation in local emissivity profile analysis.....88

5.2.4 Evaluation of W^{24+}-W^{26+} ion density profiles.....90

5.3 Discussions on the tungsten ion density.....97

5.4 Summary.....99

References.....100

6. Effect of neutron and γ-ray on charge-coupled device for vacuum/extreme ultraviolet spectroscopy in deuterium discharges of Large Helical Device.....101

6.1 Introduction.....101

6.2 Experimental setup.....102

6.3 Experimental results.....104

6.3.1 Signal noise on CCDs of VUV, EUV and X-ray spectrometers during D-D experiment.....104

6.3.2 Examination of signal noise induced by neutron and γ-ray using shielding CCD.....108

6.3.3 Reduction of signal noise.....111

6.4 Summary.....113

References.....113

7. Summary and Conclusion.....115

Acknowledgements.....119

Publications.....121

List of figures

1.1 Diagram of triple product, $n_iT_i\tau_E$, versus ion temperature, Ti, obtained in different magnetically confined fusion devices.....2

1.2 Ionization energy, E_i, as a function of ionization stage of tungsten ions, W^{q+}. Electron temperature ranges of ITER at $T_e = E_i$ are indicated with horizontal dashed lines for edge ($0.9 \leq \rho \leq 1.0$), SOL and divertor plasmas at 1-4, 0.2-1.0 and 0.03-0.20 keV, respectively. Electron temperature range of LHD NBI plasmas is also denoted with gray-hatched area. Ionization stages in W UTA spectra are denoted with solid triangles for WXXII-XL (W^{21+}-W^{39+}).....5

1.3 Bird's eye of LHD.....8

2.1 Time behaviors of port-through NBI power, line-averaged electron density, central electron temperature, total radiation power and plasma stored energy. A coaxial pellet with tungsten wire size of 0.05 mmϕ × 0.7 mmL is injected at t = 4.33 s.....20

2.2 Temporal evolutions of radial profiles of electron temperature, T_e and electron density just before (t=4.3 s) and after (4.4-5.2 s) the pellet injection.....21

2.3 EUV spectra of tungsten emission lines observed in LHD at 10-35 Å, 35-55 Å, 55-90 Å, 90-120 Å, 120-155 Å, 155-190 Å, 190-225 Å, 225-260 Å, 260-295 Å, 295-330 Å, 330-365 Å, 365-400 Å, 400-435 Å, 435-470 Å and 470-500 Å.....22

2.4 Tungsten UTA spectra at central electron temperatures of 0.42, 0.87, 1.63, 1.94 and 2.45 keV.....25

2.5 Vertical profiles of WXLII (W^{41+}) (130.93 Å $\leq \lambda \leq$ 131.25 Å), WXLIV (W^{43+}) (126.05 Å $\leq \lambda \leq$ 126.37 Å) and WXLV (W^{44+}) (132.72 Å $\leq \lambda \leq$ 133.06 Å).....27

3.1 Side view of two space-resolved EUV spectrometers.....34

3.2 Discharge waveform with tungsten pellet injection at 4.8s; NBI port-through power, line-averaged electron density, central electron temperature, plasma stored energy and total radiation power.....36

3.3 Tungsten UTA spectra at t = 5.3 s measured with EUV_Long2 and EUV_Short2. It should be noticed that the apparent spectral resolution is not good in both the EUV_Long2 and EUV_Short2 because the binning is made in the CCD horizontal pixel for faster sampling time.....37

3.4 Vertical profiles of WXXVIII at lower- and upper-half plasma radii at t = 5.3 s

measured with EUV_Long2 and EUV_Short2, respectively, and lower-half profile superimposed on upper-half profile.....38

3.5 Local emissivity profiles of WXXVIII at lower- and upper-half plasma radii reconstructed with Abel inversion method.....39

4.1 Ionization energy, E_i, as a function of charge state of W ions, W^{q+}. Electron temperature ranges of ITER at $T_e = E_i$ are indicated with horizontal dashed lines for edge ($0.9 \leq \rho \leq 1.0$), SOL and divertor plasmas as 1-4, 0.2-1.0 and 0.03-0.20 keV, respectively. Electron temperature range of LHD NBI plasmas is denoted with gray-hatched area. Ionization stages in W UTA spectra are denoted with solid triangles at WXXII-XLIV (W^{21+}-W^{43+}). WI (W^{0+}), WIV-VII (W^{3+}-W^{6+}) and WXLV-XLVI (W^{44+}-W^{45+}) have been already identified in visible, VUV and EUV wavelength ranges, respectively.....45

4.2 Typical EUV spectrum at 10-75 Å in NBI discharges of LHD with carbon divertor plates and stainless steel first wall. Several well-known carbon and oxygen lines are observed in the spectrum.....47

4.3 Cubic polynomial fitting with ten well-known emission lines and deviation of experimentally determined wavelengths from theoretically calculated wavelengths as a function of channel numbers of CCD, N.....49

4.4 Optical layout of EUV_Short spectrometer. Two axes of X and Y are perpendicular and parallel to 2400 grooves/mm grating surface, respectively. CCD moves along X axis to change the wavelength interval for observation. Distances from entrance slit to grating center (X=0, Y=0) and from grating center to focal plane are 237 and 235 mm, respectively. Angle of incidence, α, is fixed to 88.65° and output angles, β, is a function of wavelength, e.g. 75.31° (β_2) at 135 Å and 86.88° (β_1) at 5 Å.....50

4.5 Time behaviors of NBI port-through power, line-averaged electron density, central electron temperature, total radiation power and plasma stored energy. A coaxial graphite pellet (0.6 mm^{ϕ} × 0.6 mm^{L}) with tungsten wire size of 0.15 mm^{ϕ} × 0.6 mm^{L}, which is the maximum size of tungsten to avoid the radiation collapse, is injected at t = 3.8 s.....53

4.6 Tungsten spectra with UTA in wavelength range of 15-70 Å at t = 4.37 s (0.60 keV), 4.50 s (0.94 keV) and 4.67 s (1.34 keV), and CCD channel number at intensity peak of three emission lines of W^{27+} at 47.88-47.96 Å, W^{28+} at 48.85-48.92 Å and W^{27+} at 49.34-49.41 Å as a function of central electron temperature, T_{e0}.....54

4.7 Intensity of tungsten UTA lines at each wavelength interval of (a) to (o) in range of 19 $\leq \lambda \leq$ 33 Å as a function of central electron temperature, T_{e0}. The intensity is normalized to central electron density, n_{e0}. The wavelength interval is denoted at the top-right corner in each figure. The ionization stages are estimated from the electron temperature at the intensity peak denoted with vertical arrows.....56

4.8 Intensity of tungsten UTA lines at each wavelength interval of (a) to (h) in range of 47 $\leq \lambda \leq$ 54 Å as a function of central electron temperature, T_{e0}. The intensity is normalized to central electron density, n_{e0}. The wavelength interval is denoted at the top-right corner in each figure. The ionization stages are estimated from the electron temperature at the intensity peak denoted with vertical arrows.....59

4.9 Time behaviors of tungsten UTA line intensities at wavelength intervals of 27.18-27.24 Å, 28.46-28.53 Å, 29.89-29.95 Å, 31.17-31.23 Å and 32.31-32.37 Å consisting of a single ionization stage of tungsten ions. The intensity is normalized to central electron density, n_{e0}. Tungsten pellet is injected at 3.82 s.....61

4.10 Time behaviors of NBI port-through power, line-averaged electron density, central electron temperature and total radiation power in two discharges with different tungsten pellet sizes; #125854 (solid lines): 0.1 $mm^{\phi} \times 0.7$ mm^{L} injected at t = 4.0 s and #130889 (dashed lines): 0.05 $mm^{\phi} \times 0.7$ mm^{L} injected at t = 4.8 s.....62

4.11 Tungsten spectrum with UTA lines at 27 - 34 Å measured with EUV_Short2 spectrometer. Radial profile of tungsten UTA is analyzed at each wavelength interval indicated with two adjacent vertical lines. The wavelength interval is roughly 0.1 Å and exact values are listed in Table 1. Five wavelength intervals denoted with grey-hatched region are identified as UTA emission in a single ionization stage which is denoted with horizontal arrow.....63

4.12 Electron temperature profiles, vertical intensity profiles and local emissivity profiles of tungsten UTA emission line at wavelength interval of 32.28 Å $\leq \lambda \leq$ 32.39 Å (W^{24+}) at three different central electron temperatures of T_{e0} = 1.38 keV, 1.73 keV and 2.15 keV.....65

4.13 Normalized plasma radius at peak position in vertical intensity profiles of tungsten UTA as a function of central electron temperature, T_{e0}, for three different ionization stages of tungsten ions of W^{24+} (solid squares: 32.28 Å $\leq \lambda \leq$ 32.39 Å), W^{25+} (solid diamonds: 31.14 Å $\leq \lambda \leq$ 31.25 Å) and W^{26+} (solid circles: 29.91 Å $\leq \lambda \leq$ 30.02 Å).....66

4.14 Tungsten spectrum with UTA lines at 47 - 53 Å measured with EUV_Long2

spectrometer. Radial profile of tungsten UTA is analyzed at each wavelength interval indicated with two adjacent vertical lines. The wavelength interval is roughly 0.2 Å and exact values are listed in Table 2. Three wavelength intervals denoted with grey-hatched region are identified as UTA emission in a single ionization stage which is denoted with horizontal arrow.....69

4.15 Electron temperature profiles, vertical intensity profiles and local emissivity profiles of tungsten UTA emission line at wavelength interval of 48.81 Å ≤ λ ≤ 49.03 Å (W^{24+}) at three different central electron temperatures of T_{e0} = 1.30, 1.37 and 1.86 keV.....71

4.16 Electron temperature and density profiles in #125854 at t = 4.3 s and # 130889 at t = 5.3 s.....72

4.17 Vertical intensity profiles of W^{27+} emissions at 28.38 Å ≤ λ ≤ 28.48 Å and 49.24 Å ≤ λ ≤ 49.46 Å, W^{26+} emissions at 29.80 Å ≤ λ ≤ 29.91 Å and 48.81 Å ≤ λ ≤ 49.03 Å and W^{24+} emissions at 32.28 Å ≤ λ ≤ 32.39 Å and 47.94 Å ≤ λ ≤ 48.15 Å.....75

5.1 Discharge waveform with tungsten pellet injected at 4.3 s; NBI input power, line-averaged electron density, central electron temperature, total radiation power, plasma stored energy, emission intensity from W^{24+} ions at wavelength interval of 32.18-33.34 Å, intensity of W^{25+} emission line at wavelength interval of 30.69-31.71 Å, and intensity of W^{26+} emission line at wavelength interval of 29.36-30.47 Å.....82

5.2 Electron temperature and density profiles at t = 4.2, 4.4, 4.9, 5.7 and 6.1 s.....83

5.3 Tungsten UTA spectrum at wavelength range of 18-36 Å measured by EUV_Short. Shaded area indicates a wavelength interval in which UTA emission lines are composed of a single ionization stage.....84

5.4 Fractional abundance of W^{22+}-W^{34+} calculated with ADAS code at $n_e = 4 \times 10^{13}$ cm^{-3}, and total photon emission coefficient of W^{24+} (32.16-33.32 Å), W^{25+} (30.69-31.71 Å) and W^{26+} (29.47-30.47) calculated with the present CR model and ADAS code.....85

5.5 Photon emission coefficients of W^{24+} (32.16-33.32 Å), W^{25+} (30.69-31.71 Å) and W^{26+} (29.47-30.47 Å) from the present CR model against normalized radius at t = 4.7 s.....87

5.6 Line-integrated vertical intensity at 32.16-33.32 Å taken at Δt = 0.3 s after tungsten pellet (tungsten wire: 0.05 mm^{ϕ} × 0.7 mm^{L}) injection, observation chord length, local emissivity after Abel inversion for β = 0.44% (8020) at R_{ax} = 3.60 m, and normalized errors of line-integrated vertical intensity, I_{error}/I, observation chord length, L_{error}/L_{chord} and local emissivity, $\varepsilon_{error}/\varepsilon$ for different β and pressure profiles.....89

5.7 Vertical intensity and local emissivity profiles of W^{24+} at wavelength interval of 32.16-

33.32 Å plotted at different central electron temperatures of T_{e0} = 2.19, 1.95 and 1.82 keV.....91

5.8 Density profiles of W^{24+} ions at T_{e0} = 2.19, 1.95 and 1.82 keV using photon emission coefficient calculated with the present CR model and ADAS code. Electron temperature where the vertical intensity profile of W^{24+} (32.16-33.32 Å), W^{25+} (30.69-31.71 Å) and W^{26+} (29.47-30.47 Å) takes the maximum value as a function of normalized radius at the intensity maximum.....92

5.9 Time trace of total tungsten density in the vicinity of ρ = 0.7 calculated at peak value of W^{24+} ion density profile.....94

5.10 Electron density and temperature profiles and tungsten density profiles of W^{24+} , W^{25+} and W^{26+} ions at t = 4.7 s.....95

5.11 Electron temperature and W^{24+} ion density profiles at Δt = 0.1 s after pellet injection (0.06 mm^{ϕ} × 0.7 mm^{L}) in different electron densities of 2.5 × 10^{13} cm^{-3}, 3.2 × 10^{13} cm^{-3} and 4.7 × 10^{13} cm^{-3}.....96

5.12 Electron temperature and W^{24+} ion density profiles at Δt = 0.1 s after pellet injection with different tungsten pellet seizes of 0.03 mm^{ϕ} × 0.7 mm^{L}, 0.05 mm^{ϕ} × 0.7 mm^{L} and 0.06 mm^{ϕ} × 0.7 mm^{L} 98

6.1 Arrangement of two EUV spectrometers (EUV_Short and EUV_Long), three VUV spectrometers (106RVUV, 109LVUV and 102RVUV), one Johann-type x-ray crystal spectrometer (XCS) and one additional CCD in LHD.....103

6.2 CCD images taken from EUV_Long2 in NBI discharge before D-D experiment with exposure time of 61.48 ms (#130543: N_{CCD} = 0.1 × 10^{8} counts/s, T_e=1.2 keV, n_e=3.5 × 10^{13} cm^{-3}, P_{NBI}=18.7 MW), NBI deuterium discharge during D-D experiment with exposure time of 61.21 ms (#138430: N_{CCD}=1.5 × 10^{8} counts/s, S_n=1.2 × 10^{15} n/s, T_e=3.4 keV, n_e=2.1 × 10^{13} cm^{-3}, P_{NBI}=15.1 MW) and hydrogen ECH discharge after D-D experiment with exposure time of 61.21 ms (#143782: N_{CCD}=0, T_e=1.8 keV, n_e=4.5 × 10^{13} cm^{-3} , P_{ECH}=2.5 MW).....104

6.3 Time behaviors of input power of NBI and ECH, neutron production rate and total noise count rate in the additional CCD.....105

6.4 Total noise count rate normalized by neutron production rate, N_{CCD} / S_n, against distance from CCD to plasma center (R_{ax}=3.60m) of LHD, L, for XCS, EUVShort, EUVLong, 106RVUV, 109LVUV, 102RVUV and additional CCD without shielding denoted with Naked CCD.....106

6.5 CCD without shielding, CCD with lead, CCD with polyethylene contained 10% boron and CCD with polyethylene contained 10% boron and lead.....108

6.6 Total noise count rate normalized by neutron production rate, N_{CCD} / S_n, against neutron production rate, Sn, for CCD without shielding and shielded with lead, polyethylene contained 10% boron and polyethylene plus lead.....110

6.7 Raw EUV spectrum from a single CCD frame (5 ms exposure) measured with EUV_Long at t = 4.5 s in deuterium discharge (#138430), EUV spectrum averaged with 80 CCD frames during 4.3-4.7 s (#138430), raw EUV spectrum from a single CCD frame measured at t = 5.0 s in hydrogen discharge (#130543), vertical profile of HeII at 303.780 Å measured with EUV_Long2 at t = 4.5 s in deuterium discharge (#138430), vertical HeII profile with software noise removal modified vertical HeII profile measured in hydrogen discharge (#130543).....112

List of tables

Table 1.1 Main parameters of LHD.....7
Table 1.2 Spectrometers in LHD used for the present thesis.....10
Table 2.1 Summary of spectral identification of tungsten line emissions.....28
Table 4.1 Component analysis of tungsten UTA at each wavelength interval in 27-34 Å..68
Table 4.2 Component analysis of tungsten UTA at each wavelength interval in 47-53 Å..73

Chapter 1

Introduction

1.1. Magnetically confined fusion

Development of new energy source instead of fossil fuels is one of critical issues to continue the present social activities due to the limited and localized deposits in the deep earth. Many kinds of energy sources have been developed over past few decades, i.e. wind energy, solar energy, tidal energy, geothermal energy, fission energy and so on. The renewable energies have the future possibilities to solve the present problem, while intrinsic weak points exist in each renewable energy. For example, the electric power produced from the solar energy strongly depends on the weather condition, and it is impossible to actively control the power output. Since the nuclear fission reactor is fully radioactive, management of the radioactive waste is a serious problem at present.

Thermonuclear fusion is one of the attractive energy sources because the output energy is controllable and management of the radioactive waste is much easier than the fission reactor. Considering the cross-section in the fusion reaction, the most promising process for the fusion reactor is to use D-T reaction [1] expressed by

$$D + T \rightarrow {}^4He\ (3.52\ MeV) + n\ (14.06\ MeV), \qquad (1.1)$$

where D, T, ^{4}He and n are the deuterium, tritium, α particle and neutron, respectively. The natural abundance of deuterium isotope is ~0.015% against hydrogen, and it is expected to extract from the seawater because one liter seawater contains 30 mg deuterium. Tritium can be generated from lithium-6 by colliding with neutrons. Since the natural abundance of lithium-6 is only 0.0065%, the lithium-6 is also planned to extract from the seawater in which 0.17mg lithium-6 is contained in one liter seawater. The tritium is produced in the blanket of fusion reactor surrounding the vacuum vessel for plasma production. The thermonuclear power given by eq. (1.1) consists of two parts. The neutron with a kinetic energy of 14.06 MeV leaves the plasma without any interaction with bulk particles, and contributes to the electric power generation in the blanket. The α particle with kinetic energy of 3.52 MeV contributes to the maintenance of high-temperature plasmas through collisions with bulk electrons and ions as a unique heating source in the steady fusion reactor.

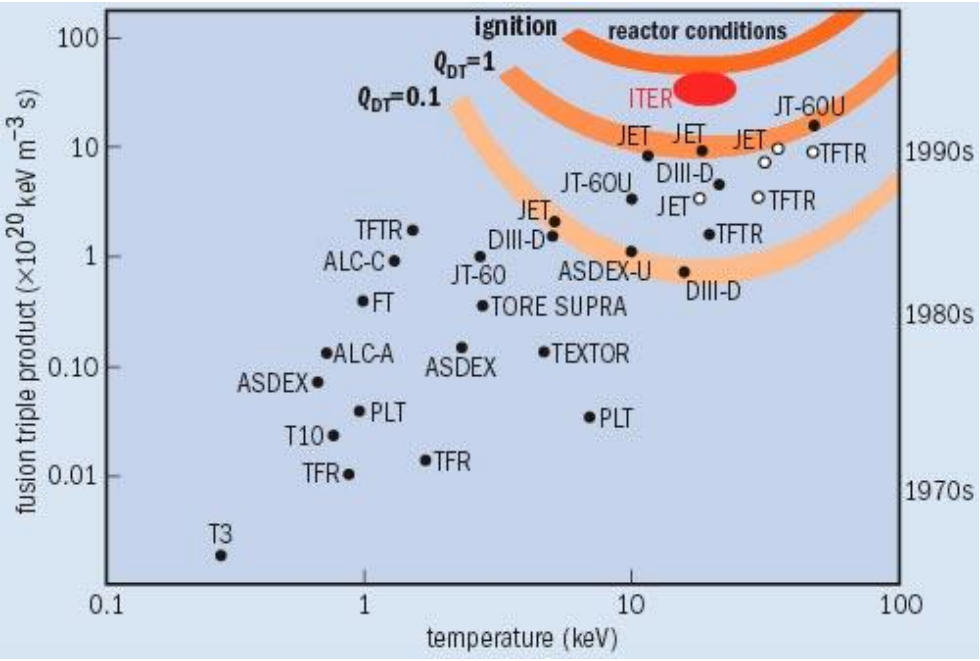

Fig. 1.1 Diagram of triple product, $n_iT_i\tau_E$, versus ion temperature, T_i, obtained in different magnetically confined fusion devices [2].

When the energetic α particle is sufficiently confined in plasmas, the ignition condition necessary for the self-sustainment of D-T burning plasmas is given by Lawson criterion [3] of

$$n_i T_i \tau_E > 3\times10^{21}\ m^{-3}\cdot keV\cdot s, \qquad (1.2)$$

where n_i, T_i, τ_E are the ion density, ion temperature and energy confinement time, respectively. In practice, the precise values in eq. (1.2) depend on the profiles of n_i and T_i. In fusion research there are two directions to obtain the ignition condition, i.e. magnetic confinement using toroidal devices [4] and inertial confinement using high-power laser [5]. The magnetic confinement fusion can steadily generate the thermonuclear fusion power, while the inertial confinement fusion basically provides a pulse operation in the fusion reactor. Over past several decades, the magnetic confinement fusion devices called tokamak [6] and stellarator [7] have been mainly developed, and the plasma performance has been steadily improved and recently it becomes possible to achieve the ignition condition, as shown in Fig. 1.1. So far, many toroidal devices have been built in the world, i.e. LHD [8], JT-60U [9], DIII-D [10], JET [11], ASDEX-U [12] and W7-X [13], and the fusion research has been extensively carried out for the plasma performance improvement in addition to further understanding of the toroidal plasma. Based on the confirmation of size scaling on the plasma performance which is the most important result from such toroidal devices, International Thermonuclear Experimental Reactor (ITER) [14] is now under construction in France as the first reactor scale magnetic fusion device. ITER is expected to perform a steady-state discharge of D-T burning plasmas. The most important goal of ITER is to demonstrate a clear path toward the DEMO reactor by showing the feasibility on steady-state operation of the burning plasma and an insignificant impact on the environment [15].

1.2. Impurities in fusion plasma

Impurities always exist in fusion plasmas. It is well known that the impurity limits the operational region of fusion plasmas through radiation power loss. In general, the impurity is produced through collisions of plasma particles with plasma facing components called sputtering. Therefore, typical impurity spices based on the sputtering are carbon or

tungsten as a divertor material and iron as a first wall material. In the burning plasma, on the other hand, α particles, i.e. He^4, also becomes the impurity, which is called 'helium ash'.

The radiation loss from impurities consists of bremsstrahlung continuum and spectral line emissions including recombination radiation. In fusion research the bremsstrahlung is important in high-density discharges because the upper limit of discharges is restricted by the increased bremsstrahlung, if MHD instability can be ignored. In practice, the density limit in tokamaks is often observed in Marfes [16, 17], detached plasmas [18, 19] and disruptive density limit [20, 21]. In case of low-Z impurities, such as carbon (Z = 6), the radiation loss is very low because such impurities become fully stripped ions in high-temperature plasmas due to the low ionization energy. Then, the low-Z impurity usually brings a fuel dilution in fusion plasmas affecting the high impurity density concentration, e.g. $n_C/n_e \sim 10^{-2}$. In case of high-Z impurities, such as tungsten (Z=74), on the other hand, the impurity is not fully stripped in the core plasma due to the high ionization energy. Therefore, the cooling rate, i.e. radiation power per ion, of the high-Z impurity is much larger than that of the low-Z impurity because it rapidly increases with the atomic number of impurities. For example, the carbon radiation power exceeds 10% of the total fusion power in a fusion reactor at $n_C/n_e \sim 10^{-1}$, while the tungsten has the same radiation power at $n_W/n_e \sim 10^{-4}$ [22]. Therefore, transport study of the high-Z impurity is very important in fusion research. In general, the core impurity density largely depends on transport processes occurring within a few centimeters of the last closed flux surface (LCFS). Impurity neutrals originating from the plasma facing components are ionized in the divertor region and then impurity ions move upstream toward the scrape-off layer (SOL). Once the high-Z impurity enters the core plasma, it tends to accumulate in the plasma center due to the neoclassical effect. If the impurity screening effect is dominant in the SOL or core region of plasmas, the impurity accumulation can be reduced [23-25].

In ITER, the use of tungsten has been decided for the divertor material instead of carbon material because of the favorite capabilities of tolerating an extremely large thermal heat load, reducing the erosion and tritium retention rates. However, when the tungsten density concentration in the plasma central region exceeds a threshold level, e.g., $n_W/n_e > 10^{-5}$, the large radiation loss dramatically lowers the plasma performance [26]. Therefore, the quantitative diagnostic of tungsten ions is extremely important for controlling the tungsten concentration and maintaining a good plasma performance.

Recently, in many tokamaks the tungsten divertor has been installed to obtain experimental data for the ITER operation [27, 28]. In addition, tungsten behavior has been extensively studied in many fusion devices based on spectroscopic techniques [29-34]. The

result indicates that the radial distribution of tungsten ions often shows an asymmetric profile. Up-down and in-out asymmetries are reported for not only the tungsten but also argon and nickel [35-40]. The reason is mainly attributed to the neoclassical effect [41] on poloidal flows and the centrifugal effect due to externally applied torque which leads to toroidal flows exceeding the impurity thermal velocity, $v_{\varphi,z}/v_{th,z} > 1$ [42]. Anomalous radial transport [43] may be also sensitive to the asymmetric profile formation. Such strong poloidal asymmetries lead to misinterpretation of measured radial profile data, if the radial profile is measured at half of plasmas and analyzed as a function of magnetic surfaces. Therefore, it is extremely important to examine whether the profile is asymmetric or symmetric. For the purpose, a full radial profile, i.e. radial profiles at upper and lower half plasmas, has to be measured to check the asymmetry/symmetry before analyzing the radial profile in detail.

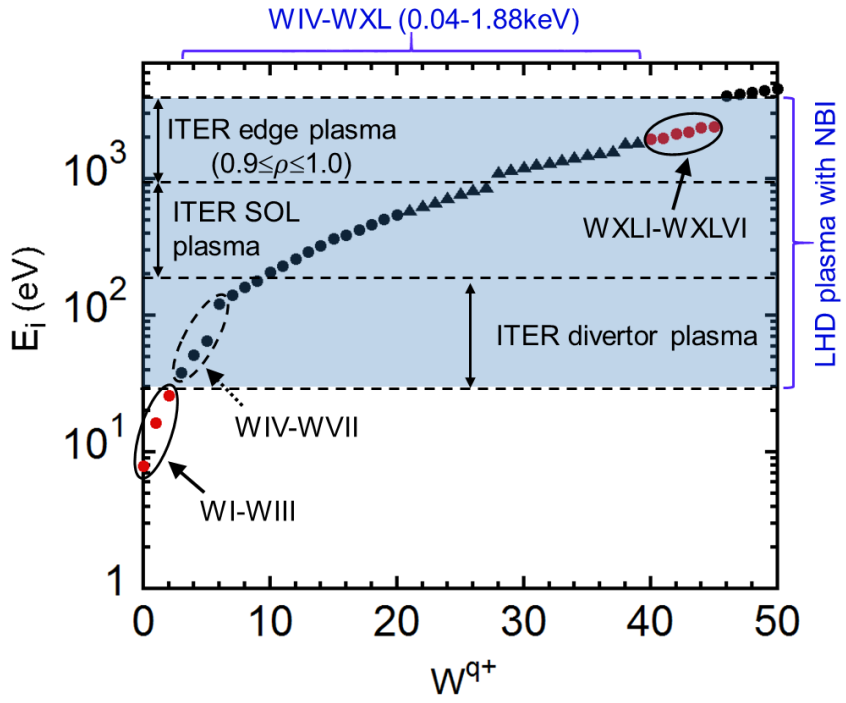

Fig. 1.2 Ionization energy, E_i, as a function of ionization stage of tungsten ions, W^{q+}. Electron temperature ranges of ITER at $T_e = E_i$ are indicated with horizontal dashed lines for edge ($0.9 \leq \rho \leq 1.0$), SOL and divertor plasmas at 1-4, 0.2-1.0 and 0.03-0.20 keV, respectively. Electron temperature range of LHD NBI plasmas is also denoted with gray-hatched area. Ionization stages in W UTA spectra are denoted with solid triangles for WXXII-XL (W^{21+}-W^{39+}).

At present, on the other hand, understanding of the tungsten spectra for diagnostics and transport study is still insufficient [44-46], whereas knowledges on the spectral structure and atomic data of light- and medium-Z impurities such as carbon and iron are accurately obtained through data accumulation over past several decades based on numerous works in both fields of plasma spectroscopy and atomic physics [45-50]. The ionization energy, E_i, of tungsten ions is plotted in Fig. 1.2 as a function of charge states [51]. If the electron temperature at a plasma radius where a tungsten ion locates is equal to the ionization energy, E_i, of tungsten ions, the electron temperature parameter range in LHD discharges maintained by neutral beam injection (NBI) can be indicated in the figure, as denoted with shaded area. Electron temperature ranges of edge, scrape-off layer (SOL) and divertor plasmas of ITER are also denoted with arears surrounded by horizontal dashed lines [52, 53]. Since the central electron temperature of ITER is very high, e.g. 20keV, the charge state of tungsten ions are also sufficiently high, e.g. W^{70+}-W^{72+}. The atomic configuration of such ions is relatively simple because such ions have only a few orbital electrons. It means the quantitative analysis of tungsten line emissions from such ions is rather straightforward. On the contrary, the tungsten ions staying in edge plasmas of ITER have many orbital electrons and form a complicated atomic structure. When spectral lines from these tungsten ions with many orbital electrons are spectroscopically studied in detail, the result can give valuable information for the edge plasma diagnostics of ITER in addition to a contribution to the atomic physics.

A neutral tungsten emission, WI (W^0), is observed in visible range at 4009 Å [54-58]. The neutral line has been now widely used for study of the plasma wall interaction [59-61]. Line emissions from WII-WIII (W^{1+}-W^{2+}) are found in JET and LHD at visible range [62, 63]. Line emissions from weakly ionized tungsten ions, WIV-WVII (W^{3+}-W^{6+}), are observed in vacuum ultraviolet (VUV) range of 500-1500 Å using a 3 m space-resolved VUV spectrometer with good spectral resolution, while the VUV spectrometer is not installed on ITER. The ion temperature is then evaluated from Doppler broadening analysis of WV-WVI (W^{4+}-W^{5+}) lines [64]. The WXL1-WXLVI (W^{40+}-W^{45+}) lines have been already observed in many fusion devices at the vicinity of 60 Å and 130 Å in extreme ultraviolet (EUV) range and qualitatively analyzed in detail [65-69]. For the tungsten diagnostic in the EUV range, however, a big gap still exists between W^{2+} and W^{40+} ions because the tungsten spectrum changes to pseudo-continuum spectrum called unresolved transition array (UTA) in the gap. The ionization energy of these ions ranges in an energy gap between 0.04 and 1.88 keV. At present, any quantitative analysis on the tungsten UTA is difficult. Further qualitative and quantitative studies on the tungsten UTA spectra

composing of WIV-WXL (W^{3+}-W^{39+}) are necessary for tungsten diagnostics in the edge, SOL and divertor plasma regions of ITER shown in Fig. 1.2.

Table 1.1 Main parameters of LHD

Major radius (R)	3.5-4.2 m
Minor radius (a)	0.50-0.65 m
Plasma volume (V_p)	20-30 m^3
Magnetic field (B_t)	< 3 T
ECRH power (P_{ECRH})	3.7 MW
ICRF power (P_{ICRF})	2 MW
Total NBI power (P_{NBI})	28 MW
Central electron temperature (T_{e0})	20 keV
Central ion temperature (T_{i0})	10 keV
Central electron density (n_{e0})	1×10^{12}-1×10^{15} cm^{-3}

1.3. Large Helical Device and spectrometers

Large Helical Device (LHD) [70] shown in Fig. 1.3 is the superconducting stellarator which can produce quiescent plasmas without toroidal plasma current. The LHD plasma is basically confined by a pair of superconducting helical coils with poloidal/toroidal pitch numbers of l/m = 2/10. Based on the unique magnetic configuration, a double-null separatrix is intrinsically created with edge stochastic magnetic field layer. The helical coils create the rotational transform and magnetic shear. A typical value of the rotational transform at standard magnetic axis position of R_{ax} = 3.60 m is 0.35 at plasma center and 1.4 at plasma edge. Three sets of superconducting poloidal coils are also set up to control the plasma axis position, the plasma elongation and the leakage magnetic field. In addition, ten pairs of resonant magnetic perturbation (RMP) coils with m/n = 1/1 mode are installed on the top and bottom of the vacuum vessel, as shown in Fig. 1.3. The magnetic field structure of LHD is entirely three dimensional, and resultantly the edge

magnetic field becomes fully stochastic, while the divertor configuration is clearly formed as a built-in divertor [71]. The stochastic magnetic field layer called ergodic layer existing between the nested outermost flux surface and the separatrix is composed of the intersect of short and long magnetic field lines in range of $L_c \leq 2000$ m [72]. Here, L_c means the connection length of magnetic field lines. The main parameters of LHD are listed in Table 1.1.

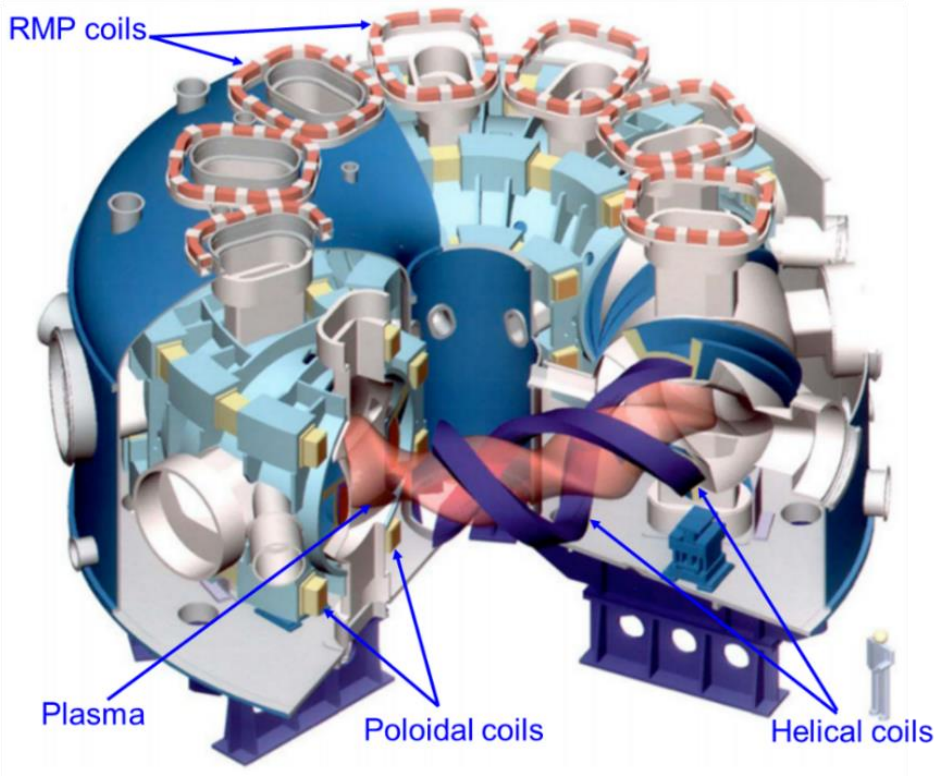

Fig. 1.3 Bird's eye of LHD.

The LHD plasma can be independently sustained by three different heating methods, i.e. neutral beam injection (NBI) [73], ion cyclotron range-of-frequency (ICRF) [74] heating and electron cyclotron resonance heating (ECH) [75]. The NBI system consists of three negative-ion-source-based NBI beams (n-NBI) with energy of 180 keV and two positive-ion-source-based NBI beams (p-NBI) with energy of 40 keV. The n-NBI mainly heats bulk electrons and is usually used for maintaining short pulse discharges in

wide plasma and discharge parameter ranges, while the p-NBI is specially characterized for the bulk ion heating in low-density discharges.

In LHD, various plasma diagnostic systems have been developed for physics and engineering studies. The diagnostic systems directly related to the present study are briefly explained in the following.

A multichannel far-infrared laser interferometer system (CH_3OH laser: 118.8 μm) with 13 vertical chords is installed on top and bottom diagnostic ports at vertically elongated plasma cross section for the measurement of spatial and temporal behaviors of the line-averaged electron density [76]. The electron density and temperature profiles are measured with a YAG Thomson scattering system along the major radius of LHD at a horizontally elongated plasma cross section [77]. The Thomson scattering system is optimized to measure the electron temperature from 50 eV to 10 keV [78]. The radiation power is monitored with a bolometer system [79] and the plasma stored energy is evaluated from diamagnetic flux measurement.

The electron temperature and density profiles from the Thomson scattering system cover the whole plasma region with spatial resolutions of 12-25 mm and temporal resolutions of 10-100 ms. Absolute values of the electron density from the Thomson scattering system is accurately calibrated using the line-integrated electron density measured with a millimeter interferometer. When the Thomson scattering system is not available for the necessary data analysis in the present thesis, the electron density profile is derived from line-integrated signals in the FIR interferometer system based on an Abel inversion technique.

In order to study the impurity transport, many kinds of spectrometers covering entirely different wavelength ranges from x-ray to visible have been developed in LHD. Specifications of the spectrometers used for the present thesis are listed in Table 1.2. Three vacuum ultraviolet (VUV) spectrometers, i.e. VUV102R, VUV106R and VUV109L, are used to monitor impurity line emissions in different wavelength ranges of 1550-2400 Å with wavelength dispersion of $d\lambda/dx$ = 0.88 Å/pixel, 1000-1850 Å with $d\lambda/dx$ = 0.88 Å/pixel and 300-1050 Å with $d\lambda/dx$ = 0.85 Å/pixel, respectively. These three VUV spectrometers are used to measure VUV lines from tungsten ions at lower ionization stages, i.e. WVI lines at 639.683 Å, 677.722 Å and 639.683×2 Å [80]. Two extreme ultraviolet (EUV) spectrometers called EUV_Long [81] and EUV_Short [82] are also used to monitor impurity line emissions in wavelength ranges of 30-650 Å and 10-130 Å, respectively. The EUV_Long and EUV_Short spectrometers are characterized by high temporal (Δt = 5 ms) and spectral resolutions ($d\lambda/dx$ = 0.149 Å/pixel at λ = 105 Å for EUV_Long and $d\lambda/dx$ =

0.051 Å/pixel at λ = 25 Å for EUV_Short) having no spatial resolution. Two space-resolved EUV spectrometers called EUV_Long2 [83] and EUV_Short2 [84] are installed on #10-O port of LHD for measuring a spatial distribution of impurity line emissions in wavelength rages of 30-650 Å and 10-130 Å, respectively. The EUV_Long2 spectrometer has a specific capability of scanning the observation chord horizontally during a single discharge [85]. A Johann-type x-ray crystal spectrometer (XCS) [86] is installed on #3-O port for monitoring the ion temperature in the central plasma region at every 5 ms by measuring Doppler broadening of He-like resonance line of ArXVII. A back-illuminated charge-coupled device (CCD) is used for all spectrometers mentioned above.

Table 1.2 Spectrometers in LHD used for the present thesis.

Spectrometer	Type	λ range (Å)	Spatial resolution	Number of viewing channels	Time resolution (ms)
VUV102R	Normal incidence	1550-2400	no	1	5
VUV106R	Normal incidence	1000-1850	no	1	5
VUV109L	Normal incidence	300-1050	no	1	5
EUV_Long	Grazing incidence	30-650	no	1	5
EUV_Short	Grazing incidence	10-130	no	1	5
EUV_Long2	Grazing incidence	30-650	15 mm	204	100
EUV_Short2	Grazing incidence	10-130	15 mm	204	100
X-ray crystal	Johann type	2d = 2.0-4.2 Å	no	1	5

1.4. Objective and structure of the thesis

The objective of the present thesis is to do qualitative and quantitative studies of the tungsten spectra in EUV range of 10-500 Å based on EUV spectroscopy. The electron temperature of neutral-beam heated plasmas in LHD typically ranges in 1 keV $\leq T_e \leq$ 4 keV, and then most of line spectra from tungsten ions are emitted in the EUV range of 10-500Å. Since the temperature range of NBI plasmas in LHD corresponds approximately to that of edge, SOL and divertor plasmas in ITER, a contribution to the tungsten diagnostics for ITER edge plasmas is also an objective in the present thesis. The thesis work has been carried out mainly by measuring temporal and spatial behaviors of tungsten line emissions in the EUV range emitted from NBI plasmas of LHD. Structure of the present thesis is briefly described in the following.

Chapter 1 provides an introduction on the fusion research based on magnetic confinement and the importance of impurity transport study, in particular, for tungsten ions. A brief introduction on LHD and diagnostic systems is also made including spectroscopic systems for tungsten spectroscopy.

Chapter 2 shows results on the identification of tungsten spectra in EUV range of 10-500 Å observed after injection of a coaxial tungsten pellet. All tungsten spectra have been measured in NBI-heated plasmas using two fast-time response EUV-Short and EUV_Long spectrometers with good spectral resolution. Measured tungsten line emissions are carefully identified based on the National Institute of Standards and Technology (NIST) atomic spectra database. The result is summarized in a table with information on blended lines which is obtained from the radial profile measurement of tungsten line emissions.

Chapter 3 shows results on the asymmetric study of tungsten line emissions. For the purpose, two space-resolved EUV spectrometers have been utilized to observe the full vertical profile of tungsten line emissions, i.e. simultaneous vertical profile measurement at upper- and lower-half plasmas of LHD by EUV_Short2 and EUV_Long2, respectively. The local emissivity profile is obtained by reconstructing the measured vertical profile in the overlapped wavelength range of 30-130 Å. A up-down asymmetry is examined by comparing two local emissivity profiles of WXXVIII which belongs to a pseudo-continuum tungsten spectrum called unresolved transition array (UTA).

Chapter 4 describes results on the component investigation of ionization stages on the tungsten UTA spectra. The UTA line intensity measured at 10-70 Å is analyzed against central electron temperature to examine the presence of blended lines. Vertical profiles of the tungsten UTA spectra are also analyzed against the electron temperature profile for

further precise investigation. It is found that the wavelength intervals of 49.24-49.46 Å, 48.81-49.03 Å and 47.94-48.15 Å, which are identified as W^{27+}, W^{26+} and W^{24+}, respectively, are applicable to the tungsten diagnostics. Results of the line component analysis on the tungsten UTA are summarized in tables for every wavelength interval with information of the ionization stage of blended lines.

Chapter 5 shows results on the ion density evaluation of tungsten ions. Density profiles of W^{24+}, W^{25+} and W^{26+} ions are analyzed from radial profiles of the UTA spectra at wavelength intervals of 32.16-33.32, 30.69-31.71 and 29.47-30.47 Å, respectively. It is found that those ions have similar densities of $1\text{-}2\times10^{9}$ cm^{-3}. A total tungsten ion density, n_W, in the vicinity of $\rho = 0.7$ where the W^{24+} ion locates is also estimated from the W^{24+} ion density based on the fractional abundance in ionization equilibrium calculated with Atomic Data and Analysis Structure (ADAS) code.

As a supplement report in the present thesis experimental results on the effect of neutrons and γ-rays on CCD are presented in Chapter 6. Signals of several CCDs installed on the VUV, EUV and X-ray spectrometers, which are placed at different locations on LHD, are examined to study the effect of neutrons and γ-rays. An additional CCD placed in a special shielding box made of 10 cm thick polyethylene containing 10% boron and 1.5 cm thick lead is also used for the detailed analysis. It is found that the background noise caused by the γ-ray and neutron is 41% and 59% to the total noise, respectively.

Chapter 7 summarizes important results obtained through the present thesis work.

References

[1] J. Wesson, Tokamaks, 4th edition, Oxford University Press, (2012).
[2] R. Pitts, R. Buttery and S. Pinches, Phys. World 19, 20 (2006)
[3] J.D. Lawson, the Proceedings of the Physical Society B70, 6 (1957).
[4] J. Ongena, R. Koch, R. Wolf and H. Zohm, Nat. Phys. 12, 398 (2016).
[5] D. Keefe, Ann. Rev. Nucl. Part. Sci. 32, 391 (1982).
[6] L.A. Artsimovich, Nucl. Fusion 12, 215 (1972).
[7] M. Wakatani, Oxford University Press, (1998).
[8] A. Komori et al., Nucl. Fusion 49, 104015 (2009).
[9] H. Ninomiya et al., Fusion Eng. Des. 51-52, 1015 (2000).
[10] J.L. Luxon, Nucl. Fusion 42, 614 (2002).
[11] J. Wesson, The Science of JET. JET Joint Undertaking (2000).
[12] A. Kallenbach et al., Nucl. Fusion 51, 094012 (2011).
[13] V. Bykov et al., Fusion Eng. Des. 84, 215 (2009).
[14] R. Aymar, P. Barabaschi, Y. Shimomura, Plasma Phys. Control. Fusion 44, 519 (2002).
[15] R. L. Hirsch, "Fusion Research: Time to Set a New Path," Issues in Science and Technology, 31, No. 4 (Summer 2015).
[16] B. Lipschultz et al., Nucl. Fusion 24, 977 (1984).
[17] W.M. Stacey, Phys. Plasmas 3, 2673-2678 (1996).
[18] A. Loarte et al., Nucl. Fusion 38, 331 (1998).
[19] G.F. Matthews, J. Nucl. Mater. 220, 104-116 (1995).
[20] J.A. Wesson et al., Nucl. Fusion 29, 641 (1989).
[21] M. Greenwald et al., Nucl. Fusion 28, 2199 (1988).
[22] J. Wesson, Tokamaks, 4th edition, Oxford University Press, (2012).
[23] S. Morita et al., Nucl. Fusion 53, 093017 (2013).
[24] C. Breton et al., Nucl. Fusion 31, 1774 (1991).
[25] M.R. Wade, W.A. Houlberg, L.R. Baylor, Phys. Rev. Lett. 84, 282 (2000).
[26] R. Neu et al., Fusion Eng. Des. **65**, 367 (2003).
[27] T. Hirai et al., Fusion Eng. Des. 82, 1839–1845 (2007).
[28] K. Krieger et al., J. Nucl. Mater. 266, 207-216 (1999).
[29] S. Morita et al., AIP Conf. Proc. 1545, 143–152 (2013).
[30] L. Zhang et al., Rev. Sci. Instrum. 86, 123509 (2015).
[31] T. Pütterich et al., Nucl. Fusion 50, 025012 (2010).
[32] C. Angioni et al., Nucl. Fusion 54, 083028 (2014).
[33] T. Nakano et al., Nucl. Fusion 49, 115024 (2009).

[34] M. Finkenthal et al., Phys. Lett. A 127, 255-258 (1988).
[35] T. Odstrcil et al., Plasma Phys. Control. Fusion 60, 014003 (2018).
[36] M.L. Reinke et al., Nucl. Fusion 53, 043006 (2013).
[37] M.L. Reinke et al., Phys. Plasmas 20, 056109 (2013).
[38] M.L. Reinke et al., Plasma Phys. Control. Fusion 54, 045004 (2012).
[39] H. Chen et al., Phys. Plasmas 7, 4567 (2000).
[40] J.E. Rice et al., Nucl. Fusion 37, 241 (1997).
[41] K. Indireshkumar et al., Phys. Fluids B 5, 1850 (1993).
[42] M.L. Reinke et al., Plasma Phys. Control. Fusion 54, 045004 (2012).
[43] T. Fulop et al., Phys. Plasmas 18, 030703 (2011).
[44] K. Asmussen et al., Nucl. Fusion 38, 967 (1998).
[45] J. Clementson et al., Phys. Scr. 81, 015301 (2010).
[46] J. Yanagibayashi et al., J. Phys. B: At. Mol. Opt. Phys. 43, 144013 (2010).
[47] H. Zhang et al., Jpn. J. Appl. Phys. 54, 086101 (2015).
[48] H. A. Sakaue et al., J. Phys.: Conf. Ser. 163, 012020 (2009).
[49] K. Mori, M. Otsuka, and T. Kato, At. Data Nucl. Data Tables 23, 195–294 (1979).
[50] S. Morita et al., Nucl. Fusion 53, 093017 (2013).
[51] A. Kramida et al., http://physics.nist.gov/asd for NIST Atomic Spectra Database (ver. 5.2) (last accessed September 3, 2017).
[52] E.J. Doyle et al., Nucl. Fusion 47, S18 (2007).
[53] ITER Physics Expert Group on Divertor, Nucl. Fusion 39, 2391 (1999).
[54] J. W. Coenen et al., J. Nucl. Mater. 463, 78–84 (2015).
[55] A. Geier, H. Maier, and R. Neu, Plasma Phys. Controlled Fusion 44, 2091–2100 (2002).
[56] A. Thoma et al., Plasma Phys. Controlled Fusion 39, 1487–1499 (1997).
[57] S. Morita et al., AIP Conf. Proc. 1545, 143–152 (2013).
[58] T. Nakano and the JT-60 Team, J. Nucl. Mater. 415, S327 (2011).
[59] R. Dux et al., J. Nucl. Mater. 390–391, 858–863 (2009).
[60] G. J. Van Rooij et al., J. Nucl. Mater. 438, S42–S47 (2013).
[61] V. Bobkov et al., J. Nucl. Mater. 438, S160–S165 (2013).
[62] C.J. van Rooij et al., J. Nucl. Mater. 438, S42-S47 (2013).
[63] T. Shikama et al., Wideband High-resolution Spectroscopy of Metallic Pellet Ablation Plasmas in LHD, Annual Report of National Institute for Fusion Science, 122 (2013)
[64] T. Oishi et al., Phys. Scr. 91, 025602 (2016).
[65] S. Morita et al., AIP Conf. Proc. 1545, 143–152 (2013).
[66] T. Nakano and the JT-60 Team, J. Nucl. Mater. 415, S327 (2011).
[67] T. Püutterich et al., Plasma Phys. Controlled Fusion 50, 085016 (2008).

[68] T. Püutterich et al., J. Phys. B: At. Mol. Opt. Phys. 38, 3071–3082 (2005).
[69] R. Radtke and C. Biedermann, Phys. Rev. A 64, 012720 (2001).
[70] A. liyoshi et al., Fusion Technol. 17, 169 (1990).
[71] N. Ohyabu et al., Nucl. Fusion 34, 387 (1994).
[72] A. Komori et al., Fusion Sci. Technol. 58, 1-11 (2010).
[73] M. Fujiwara et al., Plasma Phys. Control. Fusion 41, B157 (1999).
[74] T. Mutoh et al., Fusion Eng. Des. 26, 387 (1995).
[75] T. Shimozuma et al., Fusion Eng. Des. 53, 525 (2001).
[76] k. kawahata et al., Rev. Sci. Instrum. 70, 707 (1999).
[77] k. Narihara et al., Rev. Sci. Instrum. 72, 1122 (2001).
[78] Yamada I et al., Rev. Sci. instrum. 81, 10D522 (2010).
[79] Wurden G A and Peterson B J, Rev. Sci. Instrum. 70, 255 (1999).
[80] T. Oishi et al., Plasma Fusion Res. 10, 3402031 (2015).
[81] M. Chowdhuri et al., Rev. Sci. Instrum. 78, 023501 (2007).
[82] M.B. Chowdhuri et al., Appl. Opt. 47, 135-146 (2008).
[83] C.F. Dong et al., Rev. Sci. Instrum. 81, 033107 (2010).
[84] X.L. Huang et al., Rev. Sci. Instrum. 85, 043511 (2014).
[85] E.H. Wang et al., Rev. Sci. Instrum. 83, 043503 (2012).
[86] S. Morita and M. Goto, Rev. Sci. Instrum. 74, 2375 (2003).

Chapter 2

Observation of tungsten line emissions in wavelength range of 10-500 Å

2.1. Introduction

In ITER (International Thermonuclear Experimental Reactor), which is a next-generation device for fusion research carrying out D-T burning plasma experiments, the tungsten material is used for plasma facing components (PFCs) in divertor region, since several positive characteristics are confirmed in the tungsten, i.e. high melting point, low sputtering yield and low tritium retention [1,2]. A spectroscopic study of tungsten becomes then important for understanding of the tungsten transport in core and edge plasmas and accurate determination of the radiative cooling rate.

A neutral tungsten emission, WI, observed in visible range at 4009 Å [3,4] has been now widely used for the plasma wall interaction study [5,6]. Until now, any other tungsten lines have not been observed in the visible range above 4000 Å due to a lack of sufficient intensity. Line emissions from weakly ionized tungsten ions, WIV-VII, have been observed in vacuum ultraviolet (VUV) range of 500-1500 Å using a 3 m space-resolved VUV

spectrometer with good spectral resolution [7]. The WXLV (W^{44+}) and WXLVI (W^{45+}) emissions have been already observed from many devices in extreme ultraviolet (EUV) range in the vicinity of 60 Å and 130 Å [8,9]. However, the spectral investigation of tungsten line emissions over the whole EUV wavelength range is still insufficient. In particular, tungsten spectral lines emitted in longer wavelength range, e.g. 200-500 Å, are not well examined because it is believed that tungsten lines probably do not exist in such a long wavelength range, while a soft x-ray spectrometer observing the wavelength range of 150-400 Å is planned to install on ITER for divertor diagnostics [10]. In order to accurately identify the tungsten spectral line over the entire EUV wavelength range, observations have been made not only for wavelength spectra but also for radial profiles in Large Helical Device (LHD) by injecting a coaxial graphite pellet with a small amount of tungsten [11]. Since LHD does not need any plasma current for plasma confinement, discharges are entirely tolerant for the impurity buildup. Therefore, the pellet injection with a variety of tungsten concentrations is possible in LHD. As a result, it is possible to generate a bright tungsten light source based on the LHD discharge with neutral beam injection (NBI). As the electron temperature of neutral-beam heated plasmas in LHD typically ranges in 1 keV $\leq T_e \leq$ 4 keV, most of line spectra from tungsten ions are emitted in the EUV range of 10-500 Å. The tungsten spectra in 10-500 Å are carefully identified and the result is summarized in a table. Several line emissions from low-ionized tungsten ions are newly found in longer wavelength range of 200-500 Å.

2.2. Experimental setup

Two grazing-incidence EUV spectrometers called EUV_Short [12] and EUV_Long [13] are used for the present study to observe tungsten line emissions in the wavelength range of 10-130 Å and 30-500 Å, respectively. Both spectrometers have identical mechanical structures except for the grating and angle of incidence, i.e. a fixed entrance slit width of 30 μm, a gold-coated concave varied-lines-spacing (VLS) laminar-type holographic grating and a back-illuminated charge-coupled device (CCD: 1024 × 255 pixels, 26 × 26 μm^2/pixel) of which the long axis (1024 pixels) of CCD is set along the wavelength dispersion. The VLS grating is used to suppress the higher-order line emissions and stray light and to increase the reflectivity of EUV light on the grating, which leads to an improvement of the spectrometer throughput. The VLS grating with 2400 grooves/mm (1200 grooves/mm) for EUV_Short (EUV_Long) requires the angle of incidence of 88.6° (87.0°). A simultaneously observable

wavelength range, $\Delta\lambda$, of EUV_Short and EUV_Long is basically determined by the detector size along wavelength dispersion. The wavelength spectrum is sequentially obtained at each 5 ms interval with full-binning mode in CCD. Both spectrometers are installed on #10-O port at a distance of ~9.5 m away from the plasma center and the tungsten pellet is also injected at the same port.

A space-resolved EUV spectrometer called EUV_Long2 [14] is installed for impurity profile measurement at wavelength range of 30-500 Å. The long axis of CCD is set perpendicular to the wavelength dispersion direction for the vertical profile measurement. The CCD is routinely operated in sub-image mode with five-pixel binning in the long axis and two-pixel binning in the short axis. The resultant CCD output signal shows an image of vertical profile versus wavelength with size of 204 × 127 channels. The temporal resolution of EUV_Long2 is generally 100 ms. The total vertical observation range in the profile measurement is nearly 0.5 m of which the range corresponds to half the vertical plasma diameter at the horizontally elongated plasma cross section.

2.3. Experimental results

A series of experiments on the tungsten spectroscopic study have been done in LHD with tungsten pellet injection. A coaxial-structured tungsten pellet with a thin tungsten wire inserted into a polyethylene or graphite cylindrical tube is injected to NBI hydrogen discharges with speed of ~200 m/s. The tungsten spectra in EUV range are measured in hydrogen discharges at magnetic axis position of R_{ax} = 3.6 m and toroidal magnetic field of B_T = -2.75 T. The minus sign of B_T means magnetic field in counter-clockwise direction.

A typical discharge with tungsten pellet injection is shown in Fig. 2.1. The pellet is injected at t = 4.33 s. As the tungsten wire with 0.05 mm diameter and 0.7 mm length is used in the discharge, the number of injected tungsten atoms is approximately 8.6×10^{16}. The discharge is maintained by three negative-ion-source-based NBIs (n-NBI#1-#3) with energy of 180 keV during 3.6-6.2 s and two positive-ion-source-based NBIs (p-NBI#4-#5) with energy of 40 keV during 6.2-8.2 s, as shown in Fig. 2.1(a). Line-averaged electron density, n_e, central electron temperature, T_{e0}, total radiation power, P_{rad}, and plasma stored energy, W_p, are shown in Figs. 2.1(b)-2.1(e), respectively. After tungsten pellet injection, ne and P_{rad} quickly increase, while T_{e0} slowly decreases and W_p stays almost constant. The T_e and n_e profiles at different discharge timings during t = 4.3-5.2 s are shown in Figs. 2.2(a) and

2.2(b), respectively. Data at t = 4.3 s indicates T_e and ne profiles just before the tungsten pellet injection. Although the T_e decreases and the ne increases after the tungsten pellet injection, both radial profiles are almost unchanged. It indicates that the tungsten injection does not disturb so much the discharge condition.

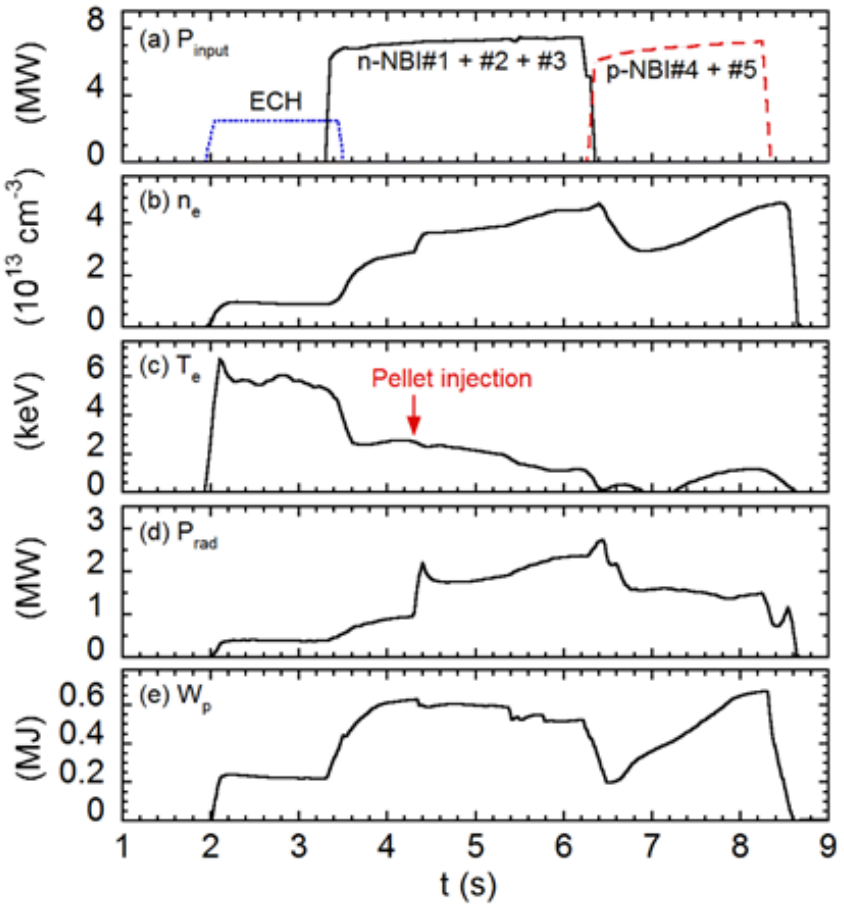

Fig. 2.1 Time behaviors of (a) port-through NBI power, (b) line-averaged electron density, (c) central electron temperature, (d) total radiation power and (e) plasma stored energy. A coaxial pellet with tungsten wire size of 0.05 mmϕ × 0.7 mmL is injected at t = 4.33 s.

The tungsten spectra at wavelength range of 10-500 Å observed with EUV_Short and EUV_Long spectrometers are carefully identified, as shown in Figs. 2.3(a)-2.3(o). The shot number, central electron temperature and data acquisition timing after pellet injection are

indicated for each spectrum. The spectra in Figs. 2.3(a) and 2.3(b) are measured by EUV_Short with spectral resolution of 0.051 Å at λ = 25 Å and 0.067 Å at λ = 45 Å. The spectra in Figs. 2.3(c)-2.3(o) are measured by EUV_Long with spectral resolution of 0.149 Å at λ = 105 Å and 0.270 Å at λ = 450 Å. Therefore, the uncertainty in the spectral wavelength determination is estimated to be 0.05 Å for short wavelength range and 0.015-0.03 Å for long wavelength range of which the values are calculated as one tenth of the spectral resolution. The emission lines are carefully identified based on NIST atomic spectra database and previous studies [8,15,16]. In Fig. 2.3, the tungsten line emissions are denoted with dotted arrows and line emissions from other impurity ions are denoted with solid arrows. The wavelength scale in abscissa of Fig. 2.3 is determined by linear interpolation and extrapolation based on the accurate wavelengths of well-known transitions in C, O, N and Fe impurity ions.

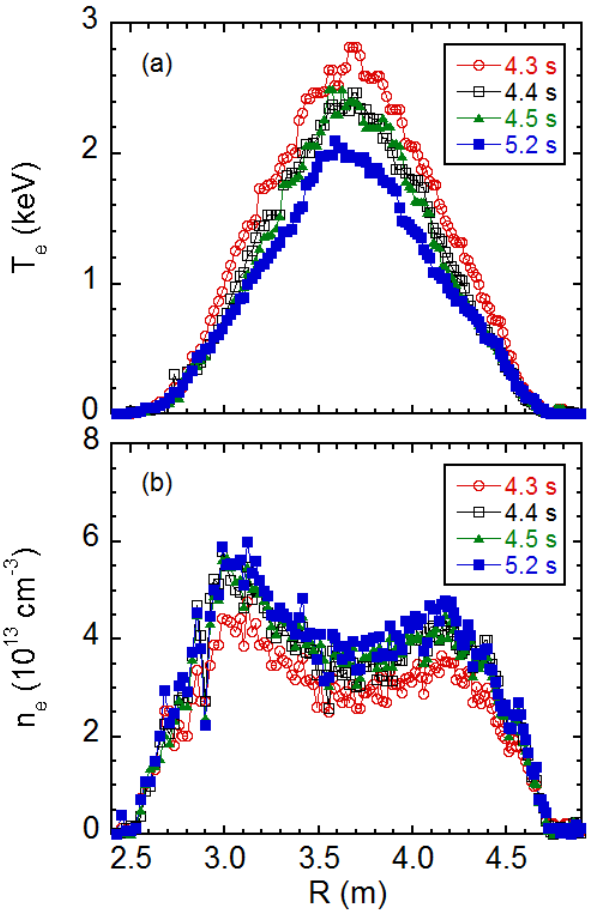

Fig. 2.2 Temporal evolutions of radial profiles of (a) electron temperature, T_e and (b) electron density just before (t=4.3 s) and after (4.4-5.2 s) the pellet injection.

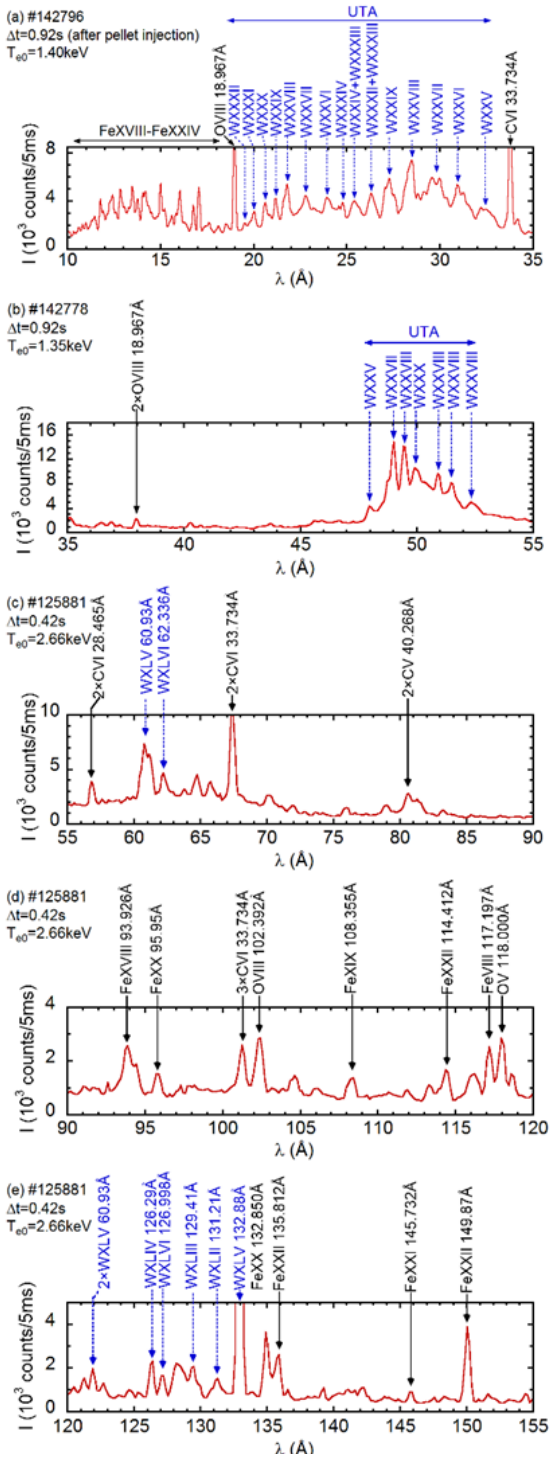

Fig. 2.3 EUV spectra of tungsten emission lines observed in LHD at (a) 10-35 Å, (b) 35-55 Å, (c) 55-90 Å, (d) 90-120 Å, (e) 120-155 Å, (f) 155-190 Å, (g) 190-225 Å, (h) 225-260 Å, (i) 260-295 Å, (j) 295-330 Å, (k) 330-365 Å, (l) 365-400 Å, (m) 400-435 Å, (n) 435-470 Å and (o) 470-500 Å.

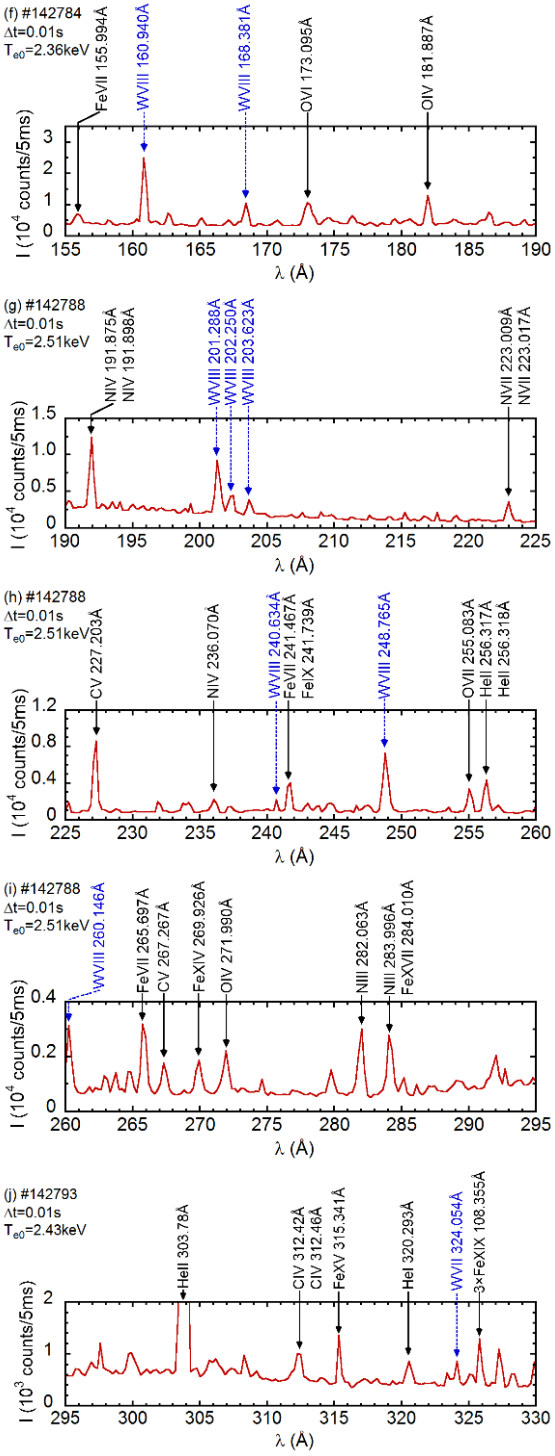

Fig. 2.3 (Continued.)

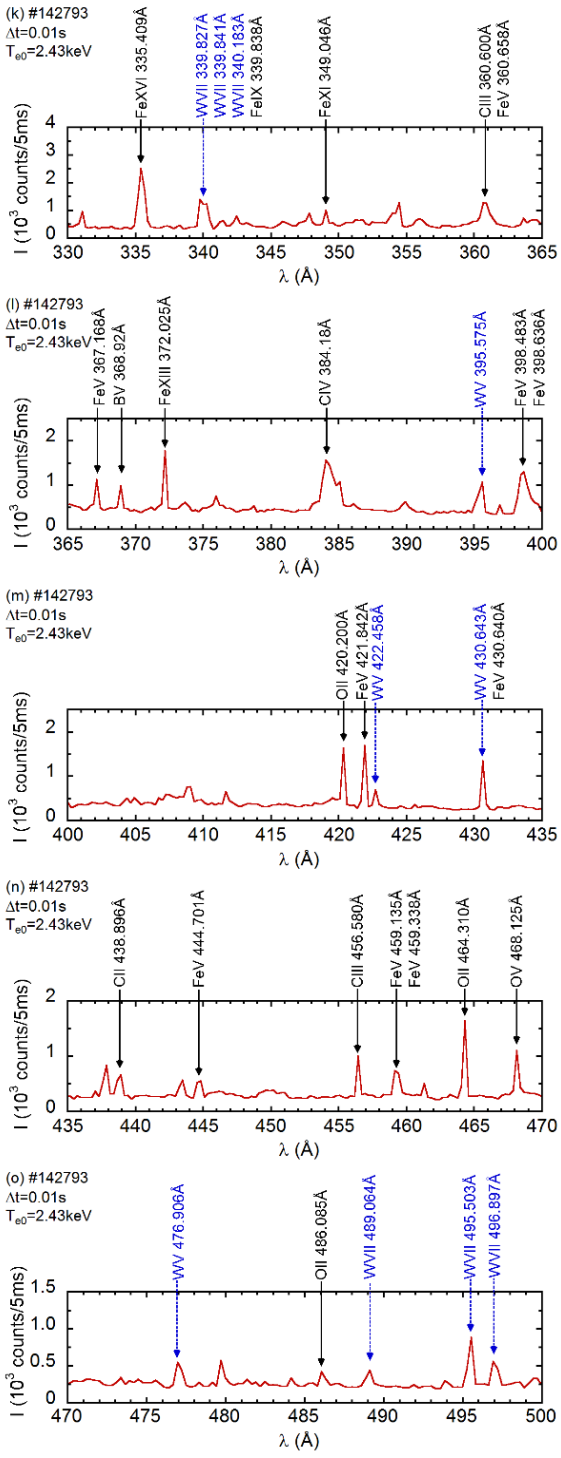

Fig. 2.3 (Continued.)

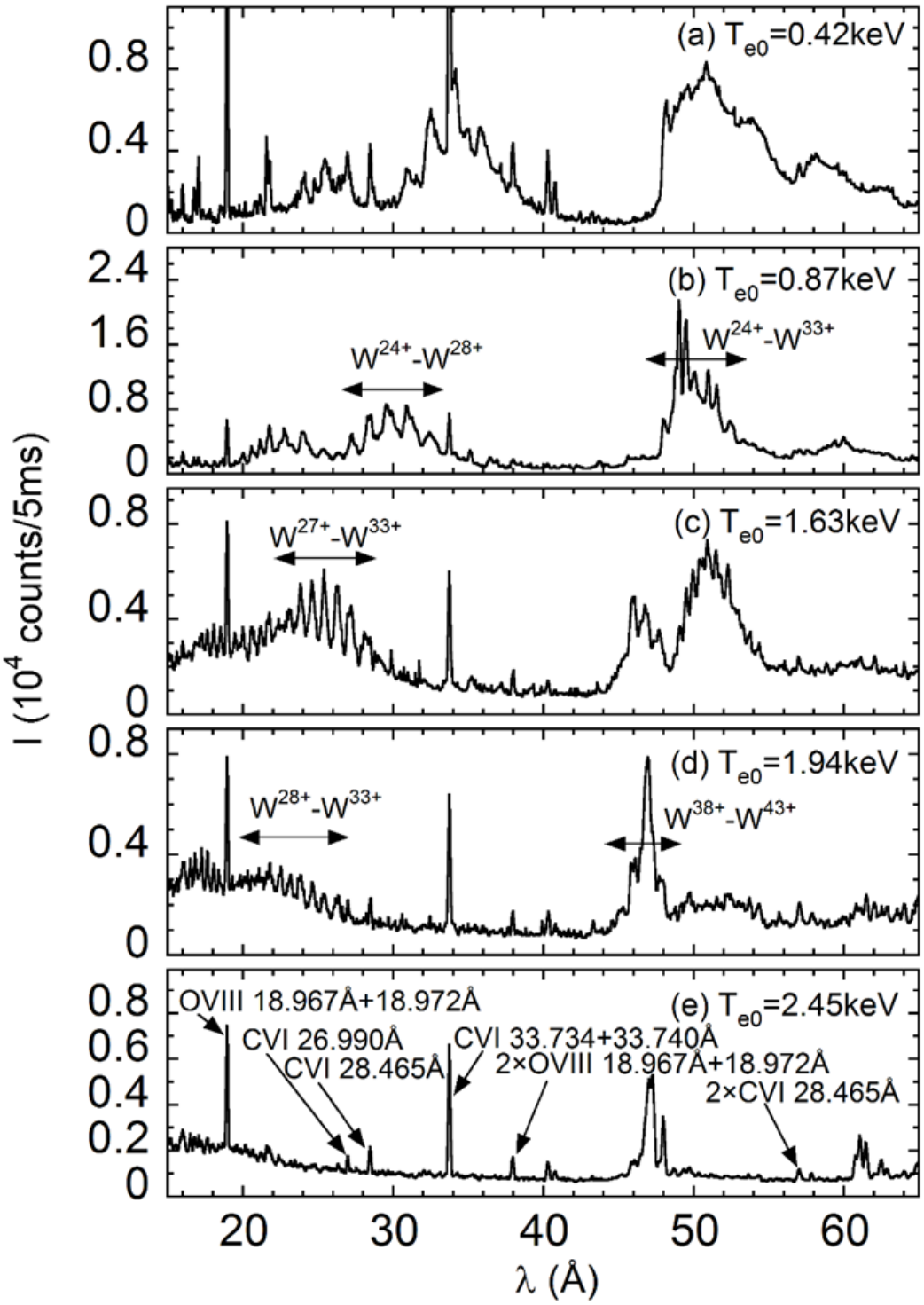

Fig. 2.4 Tungsten UTA spectra at central electron temperatures of (a) 0.42, (b) 0.87, (c) 1.63, (d) 1.94 and (e) 2.45 keV.

Two tungsten unresolved transition arrays (UTAs) appear at wavelength ranges of 19-35 Å and 48-53 Å as shown in Figs. 2.3(a) and 2.3(b), respectively. The UTA spectra are replotted in detail against different temperatures of T_{e0} = 0.42, 0.87, 1.63, 1.94 and 2.45 keV as shown in Figs. 2.4(a)-2.4(e), respectively. The UTA spectra composing of many tungsten ions largely move to shorter wavelength range with increase in T_e showing an increase in the ionization stage of tungsten ions and finally almost disappear when the T_e is sufficiently high (see Fig. 2.4(e)). As one can see from the figures, a simple spectral identification of the UTA is quite difficult. In the present study, therefore, the UTA spectra are excluded from a summary table described later. Recently, on the other hand, the UTA spectrum at 19-35 Å is attempted to understand by superposing two UTA CoBIT spectra [8]. A model calculation is also carried out to explain the LHD UTA spectrum [17]. In addition, the ionization stage of tungsten ions is determined at each wavelength interval of the UTA based on the profile measurement [16].

Tungsten line emissions from highly ionized ions are observed at T_{e0} = 2.66 keV, as shown in Figs. 2.3(c) and 2.3(e). These spectra are taken at 0.42 s after the pellet injection. The wavelength of a line emission identified as W^{44+} at 60.93 Å shown in Fig. 2.3(c) [18] is determined to be 60.87 Å in this study, while the line emission is clearly broadened. It is then estimated that the line is blended with W^{42+} and W^{43+} line emissions [19]. A line emission predicted at 62.187 Å is identified as W^{45+} with wavelength of 62.188 Å, while it is observed at 62.336Å in a previous work [18]. This emission line is also blended with tungsten emissions in lower ionization stages [19]. The blended line is estimated to be W^{39+} at 62.366 Å in EBIT result [18] and to be W^{44+} in HULLAC code [8]. Three line emissions measured at 126.29 Å, 126.998 Å, and 131.21 Å are identified as a single ionization of W^{43+}, W^{45+}, and W^{41+}, respectively [19,20]. A line emission measured at 129.45 Å in Fig. 2.3(e) is identified as W^{42+} [20,21]. A line emission measured at 132.88 Å is identified as W^{44+} [20,21]. It can be easily found because the intensity is very strong.

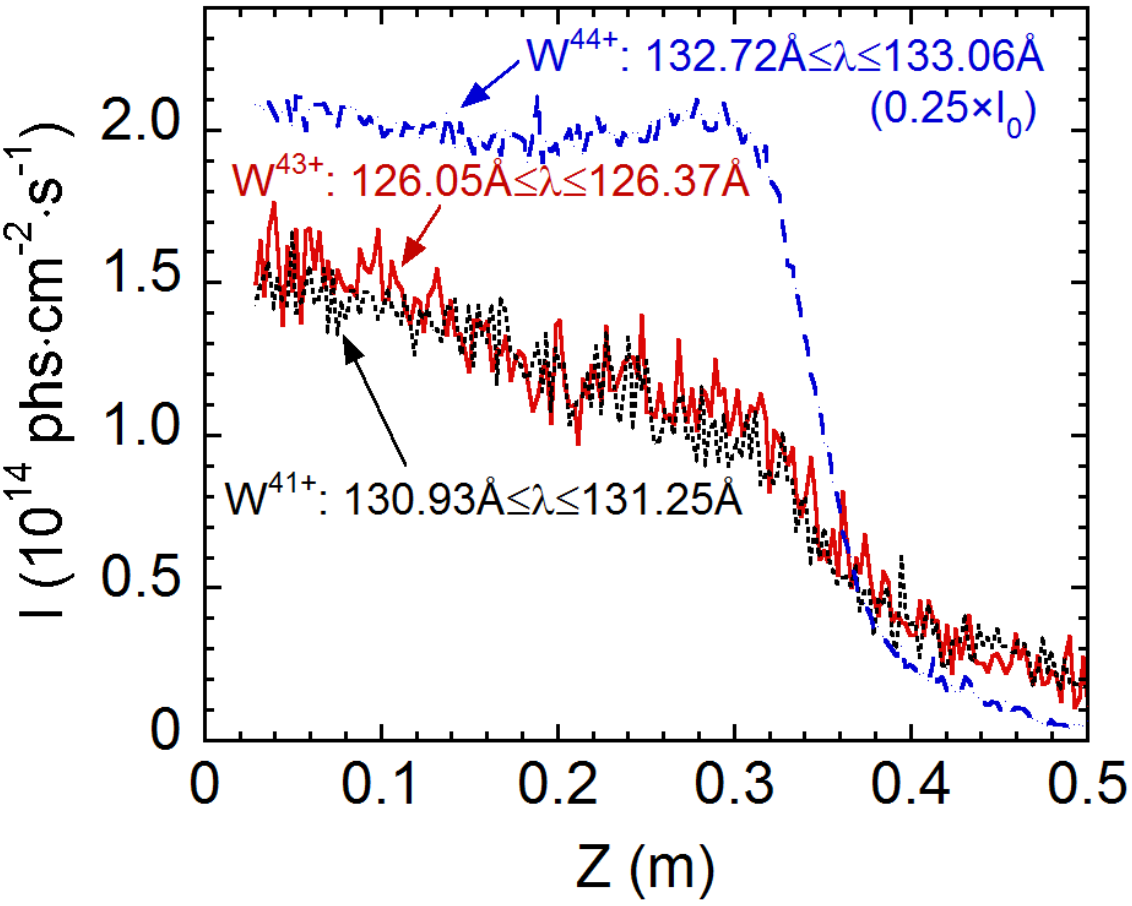

Fig. 2.5 Vertical profiles of WXLII (W^{41+}) (dotted line: 130.93 Å ≤ λ ≤ 131.25 Å), WXLIV (W^{43+}) (solid line: 126.05 Å ≤ λ ≤ 126.37 Å) and WXLV (W^{44+}) (dashed line: 132.72 Å ≤ λ ≤ 133.06 Å). The WXLV is blended with FeXX at 132.850 Å.

Table. 2.1 Summary of spectral identification of tungsten line emissions. The first column shows tungsten ionization stage and the second and third columns give the wavelengths of line emissions from NIST database and the present observation, respectively. Discrepancy between λ_{NIST} and λ_{obs} and relative spectral intensity are shown in the fourth and fifth columns, respectively. The status in the sixth column of 'Single' or 'Blended' means the emission line consists of a single ionization stage or is blended with other emission lines.

W^{q+}	λ_{NIST} (Å)	λ_{obs} (Å)	λ_{NIST} - λ_{obs} (Å)	Intensity (counts/5ms)	Status
WV (W^{4+})	395.575	395.571	0.004	1077	Single
	422.458	422.421	0.037	3523	Single
	430.643	430.629	0.014	1355	Blended (Fe^{4+})
	476.906	476.919	-0.013	553	Single
WVII (W^{6+})	324.054	324.098	-0.044	866	Single
	339.827	339.749	0.078	1407	Blended
	339.841	339.992	-0.151	1233	Blended
	340.183	340.235	-0.052	1243	Blended
	489.064	489.099	-0.035	445	Single
	495.503	495.509	-0.006	889	Single
	496.897	496.906	-0.009	564	Single
WVIII (W^{7+})	160.940	160.998	-0.058	26330	Single
	168.381	168.405	-0.024	10560	Single
	201.288	201.266	0.022	9240	Single
	202.250	202.249	0.001	4341	Single
	203.623	203.630	-0.007	3864	Single
	240.634	240.667	-0.033	2180	Single
	248.765	248.765	0	7307	Single
	260.146	260.241	-0.095	3148	Single
WXLII (W^{41+})	131.21	131.25	-0.04	1522	Single
WXLIII (W^{42+})	129.41	129.45	-0.04	2084	Blended
WXLIV (W^{43+})	126.29	126.21	0.08	1651	Single
WXLV (W^{44+})	60.93	60.87	0.06	7387	Blended (W^{42+},W^{43+})
	132.88	132.90	-0.02	16051	Blended (Fe^{19+})
WXLVI (W^{45+})	126.998	127.017	-0.019	1752	Single
	62.336	62.188	0.148	4707	Blended

In the present identification mentioned above the reliability is also checked with the radial profile measured along the vertical direction. As an example of the profile measurement, vertical profiles of W^{43+} (126.05 Å ≤ λ ≤ 126.37 Å), W^{41+} (130.93 Å ≤ λ ≤ 131.25 Å) and W^{44+} (132.72 Å ≤ λ ≤ 133.06 Å) obtained with EUV_Long2 are plotted in Fig. 2.5. The emission lines at 126.05-126.37 Å and 130.93-131.25 Å can be evaluated as a single ionization stage of W^{43+} and W^{41+}, respectively, due to the centrally peaked profile. However, the vertical profile extracted at 132.72-133.06 Å is clearly different having a shoulder at Z = 0.3 m. The blended line is estimated to be Fe^{19+} at 132.850 Å because the T_e at the shoulder position is close to the ionization energy of Fe^{19+} ions.

A lot of EUV line emissions from low-ionized tungsten ions of W^{4+}, W^{6+} and W^{7+}, are clearly observed at long wavelength range of 155-500 Å just after the tungsten pellet injection. A time duration at which such line emissions can be observed with relatively strong intensities is very short, e.g. 15 ms corresponding to 3 CCD frames. Until now WVIII spectra are observed at 175-275 Å in MT-IM tokamak without identification due to a poor spectral resolution of 5 Å at [22]. The WVIII spectra are also studied in EBIT device and calculation [23-25]. In LHD, WVIII lines are clearly found at 155-295 Å in Figs. 2.3(f)-2.3(i). However, those spectra are entirely different from EBIT spectra. The reason seems to originate in a different density between two devices. There are many data on low-ionized tungsten in the NIST atomic spectra database [15]. In practice, most of these data originate in the spark experiment [26-29] and the tungsten spectra observed from the spark plasma with spectral resolution of 0.01Å are similar to the LHD spectra.

The WV and WVII lines can be identified at 295-500 Å in Figs. 2.3(j)-2.3(o). The WVII spectra are mainly studied at 180-450 Å in the SSPX spheromak and calculation due to less data from EBIT [25-27]. However, the spectra are also quite different from LHD spectra due to the same reason as EBIT. A study is also done at 180-450 Å in spark device on WVII [26,27] and WV [28,29]. The WV and WVII spectra from the spark are also identical to the LHD spectra.

The tungsten emission lines observed at 10-500 Å in the present study are summarized in Table 1 except for the UTA lines. In Table 1, the first column shows the tungsten ionization stage, and the second and third columns give the wavelengths from NIST database and the present observation, respectively. As described above the NIST data are based on identification results from the spark experiment. Discrepancies between λ_{NIST} and λ_{obs} indicated in the fourth column are obviously smaller than 0.1 Å for all observed emission lines except for two lines at λ_{obs} = 62.188 Å and λ_{obs} = 339.992 Å. The reason is due to a large influence from blended lines. The intensity at the spectral peak is shown in the fifth

column. The WVIII line at λ_{obs} = 160.998 Å is found to be the strongest in the wavelength range of 155-500 Å. The WV and WVII intensities are relatively weak and many lines are blended with other lines. The status of observed tungsten lines is denoted in the sixth column. In the case of 'Blended' ionization stages of the blended lines are also indicated.

2.4. Summary

Tungsten spectra are observed at wavelength range of 10-500 Å by injecting a coaxial tungsten impurity pellet in LHD. Two tungsten UTAs are observed at wavelength range of 10-55 Å. The UTA at 19-35Å moves toward shorter wavelength side with electron temperature and the UTA at 48-53 Å consisting of W^{24+}-W^{33+} ions gradually disappear with electron temperature. The UTA almost disappear at sufficiently high-temperature phase, e.g. T_{e0} = 2.66 keV and line emissions from highly ionized tungsten ions begin to be observed at 55-155 Å. Blended line emissions are examined by measuring the radial profile. A lot of line emissions from low-ionized tungsten ions of W^{4+}, W^{6+} and W^{7+} are clearly observed at 155-500 Å just after the tungsten pellet injection and identified based on the NIST database. All these line emissions are observed for the first time in the toroidal device, while the NIST data are based on the result from spark plasmas. The tungsten emission lines observed at 10-500 Å are summarized in the table except for the UTA lines. The present identification shows a good agreement with the NIST data base. In particular, tungsten spectra from low-ionized ions observed for the first time in the toroidal device will contribute to the tungsten impurity diagnostics in fusion research in addition to the accuracy improvement of atomic structure modeling.

References

[1]R. Neu et al., Nucl. Fusion **45**, 209 (2005).
[2]J. Roth et al., Plasma Phys. Control. Fusion **50**, 103001 (2008).
[3]J. W. Coenen et al., J. Nucl. Mater. **463**, 78-84 (2015).
[4]A. Geier, H. Maier, R. Neu, Plasma Phys. Control. Fusion **44**, 2091-2100 (2002).
[5]R. Dux et al., J. Nucl. Mater. **390-391**, 858-863 (2009).
[6]G. J. Van Rooij et al., J. Nucl. Mater. **438**, S42-S47 (2013).
[7]T. Oishi et al., Phys. Scr. **91**, 025602 (2016).
[8]S. Morita et al., AIP Conf. Proc. **1545**, 143-152 (2013).
[9]T. Nakano and the JT-60 Team, J. Nucl. Mater. **415**, S327 (2011).
[10] R. Barnsley, the Decennial IAEA Technical Meeting on Atomic, Molecular and Plasma Material Interaction Data for Fusion Science and Technology, Daejeon, South Korea, December 2014. https://www-amdis.iaea.org/meetings/AMPMI14/Presentations/AMPMI-2014-12-15-Talk-Barnsley-ITER-2by4.pdf
[11] X. Huang et al., Rev. Sci. Instrum. **85**, 11E818 (2014).
[12] M. B. Chowdhuri, S. Morita and M. Goto, Appl. Opt. **47**, 135-146 (2008).
[13] M. B. Chowdhuri, S. Morita and M. Goto, Rev. Sci. Instrum. **78**, 023501 (2007).
[14] C.F. Dong, S. Morita, M. Goto and H. Zhou, Rev. Sci. Instrum. **81**, 033107 (2010).
[15] A. Kramida et al., NIST Atomic Spectra Database (ver. 5.5.1) [Online] Available: http://physics.nist.gov/asd [2 November 2017] (2017).
[16] Y. Liu et al., J. Appl. Phys. **122**, 233301 (2017).
[17] I. Murakami et al., Nucl. Fusion **55**, 093016 (2015).
[18] S.B. Utter et al., Can. J. Phys. **80**, 1503-1515 (2002).
[19] T. Pütterich et al., Plasma Phys. Control. Fusion **50**, 085016 (2008).
[20] T. Pütterich et al., J. Phys. B: At. Mol. Opt. Phys. **38**, 3071-3082 (2005).
[21] Y. Ralchenko et al., J. Phys. B: At. Mol. Opt. Phys. **40**, 3861-3875 (2007).
[22] G. Veres et al., J. Quant. Spectrosc. Radiat. Transfer **56**, 295-301 (1996).
[23] J. Deprince and P. Quinet, Atoms **3**, 299-319 (2015).
[24] J. Clementson et al., Atoms **3**, 407-421 (2015).
[25] J. Clementson et al., J. Phys. B: At. Mol. Opt. Phys. **43**, 144009 (2010).
[26] J. Sugar and V. Kaufman, Phys. Rev. A **12**, 994 (1975).
[27] J.F. Wyart et al., Physica Scripta. **23**, 1069-1078 (1981).
[28] S.S. Churilov, R.R. Kildiyarova, Y.N. Joshi, Can. J. Phys. **74**, 145 (1996).
[29] R.R. Kildiyarova et al., Phys. Scripta **53**, 454 (1996).

Chapter 3

Up-down asymmetry investigation of tungsten distribution using two EUV spectrometers

3.1. Introduction

Study on the tungsten transport is therefore important for suppressing the impurity accumulation at plasma core and enhancing the impurity screening at plasma edge. Until now the impurity transport has been basically studied as a function of the magnetic surface. In high-Z impurities such as tungsten, however, the radial distribution often shows an asymmetric profile. Up-down and in-out asymmetry for argon, nickel and tungsten etc. are reported in JET [1] and Alcator C-mod [2]. Both the neoclassical [3] and anomalous radial transports [4] have been proved to be sensitive to the asymmetric profile formation. The strong poloidal asymmetry can lead to misinterpretation of measured data, if the full profile is not obtained in the experiment.

The tungsten transport study has been recently started in LHD using tungsten pellet injection. Full vertical profiles of tungsten line emissions have been successfully observed at upper- and lower-half plasma radii based on the simultaneous measurement using two

space-resolved EUV spectrometers. In order to check the availability of the present diagnostic method for impurity asymmetry study, the radial profiles of local emissivity after Abel inversion is compared in upper- and lower-half plasmas and up-down asymmetry is then examined for WXXVIII emission.

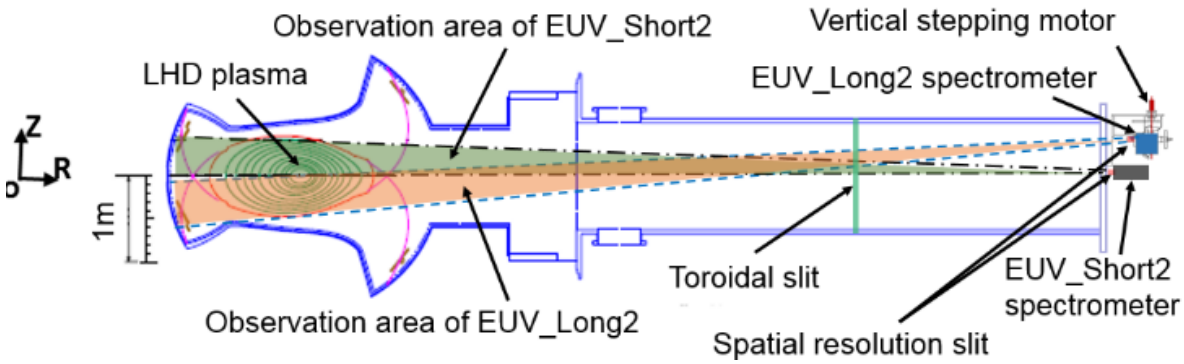

Fig. 3.1 Side view of two space-resolved EUV spectrometers.

3.2. Experimental setup

In #10-O port, two space-resolved EUV spectrometers, EUV_Long2 [5] and EUV_Short2 [6], are installed at a backside square port (size: 50 × 130 cm^2) of a cubic vacuum manifold in LHD for measuring the spatial distribution of impurity line emissions in the wavelength range of 30-500 Å and 10-130 Å, respectively. The LHD plasma at the port center is horizontally elongated with vertical diameter of $\Delta Z = \sim 1.0$ m including the stochastic magnetic field layer. A schematic diagram of two spectrometer arrangements is shown in Fig. 3.1. The cubic vacuum chamber shared by two spectrometers is evacuated by a magnetically floating turbo molecular pump and is kept in order of 10^{-8} torr. The optical axes of both spectrometers are perpendicular to the magnetic axis. The 1.2 m long toroidal slit with comb-like rectangular-corrugated apertures installed in the vacuum chamber 3 m away from spectrometers is used to calibrate the elevation angle of each observation chord. Both spectrometers have identical structures except for the number of grooves and angle of incidence of the grating, i.e. an entrance slit, a spatial resolution slit placed in front of the entrance slit, a gold-coated concave varied-lines-spacing (VLS) laminar-type holographic grating and a back-illuminated charge-coupled device (CCD) detector. The VLS grating with 1200 (2400) grooves/mm for EUV_Long2 (EUV_Short2)

covers the wavelength range of 30-500 Å (10-130 Å). Since a relatively long distance is required between the spectrometer and the plasma to observe a wider vertical plasma range, e.g. 0.5 m, which corresponds to half diameter at short axis of the elliptical LHD plasma, the spectrometers have to be placed at a long distance of 9452 mm from the plasma center to the spectrometer entrance slit. The large distance leads to a large multiplication factor, which slight depends on the spectral wavelength, e.g. 19.98 at CVI 33.74 Å and 19.65 at HeII 303.78 Å. The CCD is cooled down to -20 deg. by a Peltier device to reduce the thermal noise. The CCD has an effective area of 26.6×6.6 mm^2 with the total number of pixels of 1024×255 (26×26 μm^2/pixel). The vertical profile and spectrum are then recorded along the CCD long and short axes, respectively. The CCD detector is operated in two readout modes of full resolution image and sub-image. The full resolution image mode which can yield experimental data with the best spectral resolution is used only for the spectral resolution test and the line identification because the necessary exposure time is very long. The sub-image mode is used for routine measurement on the impurity profile. One kind of sub-images with 127×204 channels is usually used by summing up two adjacent pixels in short axis and five adjacent pixels in long axis. Thus, the spectra of impurity emissions are obtained with exposure time of 61.5 ms and sampling time of 100 ms. The spectral intensity measured by EUV spectrometers is absolutely calibrated on the basis of simultaneous profile measurement of bremsstrahlung continua in EUV and visible ranges. The vertical observation range of EUV_Short2 is fixed to the upper half plasma observation ($0 \leq Z \leq 50$ cm). In contrast the vertical observation range of EUV_Long2 ($\Delta Z \sim 53$ cm) can be freely selected by changing the vertical angle of the spectrometer optical axis. But the vertical angle change may create a systematic error in the absolute position of observation chords. The absolute position of observation chords in EUV_Short2 seems to be more accurate than that in EUV_Long2. Therefore, the vertical position calibration is frequently required for EUV_Long2 to accurately analyze the profile data.

In the present study, EUV_Long2 for lower-half observation is combined with EUV_Short2 for upper-half observation to provide the full vertical profile of tungsten emission lines in the overlapped wavelength range of 30-130 Å. In general LHD plasma discharges, CVI (33.73 Å) intensity is strong enough for the accurate positional calibration of all observation chords. Then, the positional calibration is carried out with the CVI vertical profile assuming that the CVI locates at the same radial position in both the upper- and lower-half plasmas. Thus, the up-down asymmetry study is possible for tungsten.

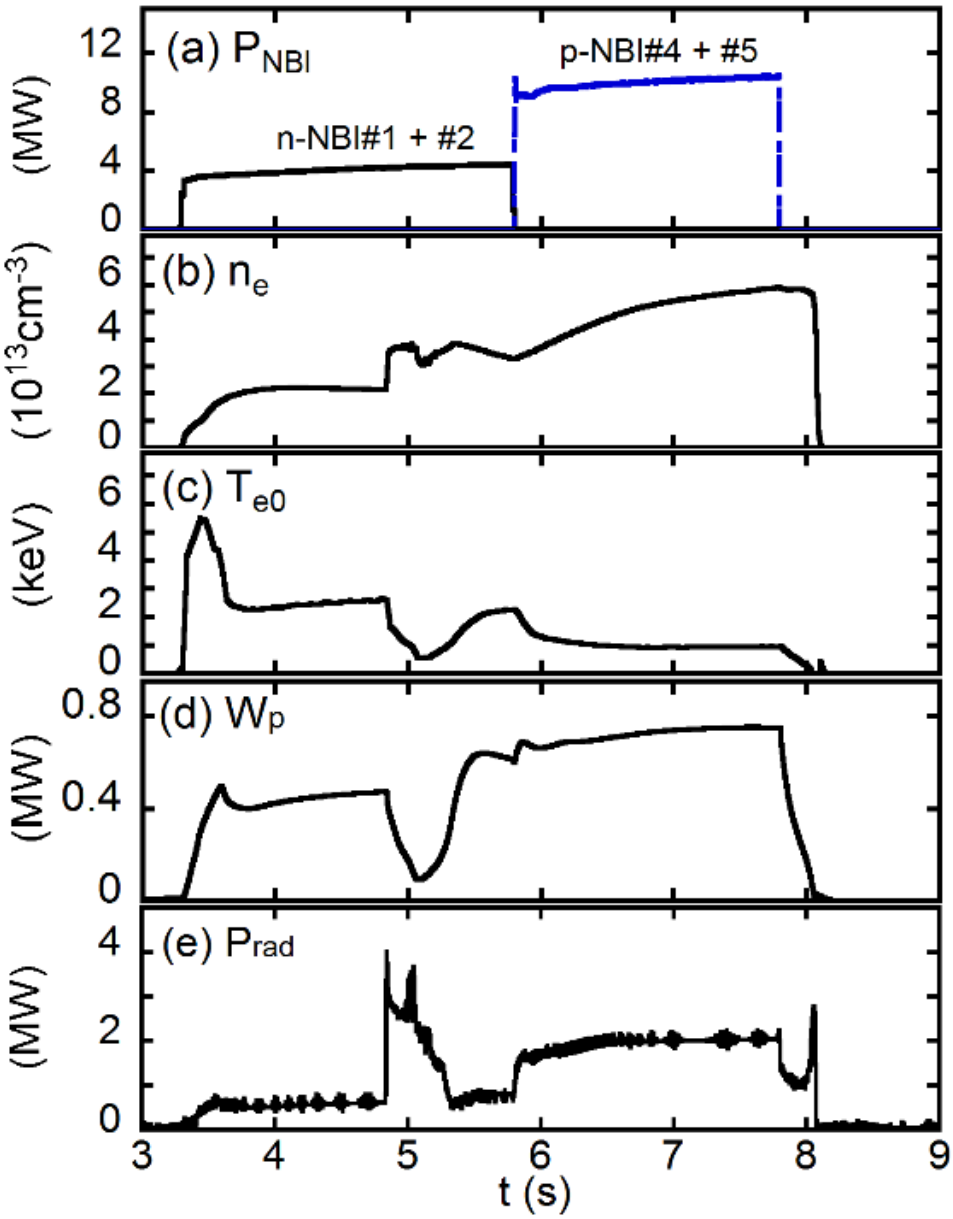

Fig. 3.2 Discharge waveform with tungsten pellet injection at 4.8s; (a) NBI port-through power, (b) line-averaged electron density, (c) central electron temperature, (d) plasma stored energy and (e) total radiation power.

3.3. Experimental Results

A series of experiments on the high-Z impurity study have been done in LHD by injecting an impurity pellet. EUV spectra from tungsten ions in high-ionization stages have been observed in LHD. A typical discharge with a relatively big coaxial tungsten pellet (tungsten wire: 0.05 mm in diameter × 0.7 mm in length, graphite cylinder: 0.7 mm in diameter × 0.7 mm in length) injected at horizontal mid-plane is shown in Fig. 3.2. The discharge is maintained by two negative-ion-source-based neutral beams (n-NBI#1 and #2) with energy of 180 keV during 4.7-5.7 s and by two positive-ion-source-based neutral beams (p-NBI#4 and #5) with energy of 40 keV. Line-averaged electron density, n_e, quickly increases at pellet injection of t = 4.8 s. It also gradually increases during p-NBI phase due to a reduction of edge particle screening. Central electron temperature, T_{e0}, and plasma stored energy, W_p, rapidly decrease and then slowly recover during n-NBI phase. Radiation power after rapid increase gradually decreases and reaches the original level after 0.5s of the pellet injection.

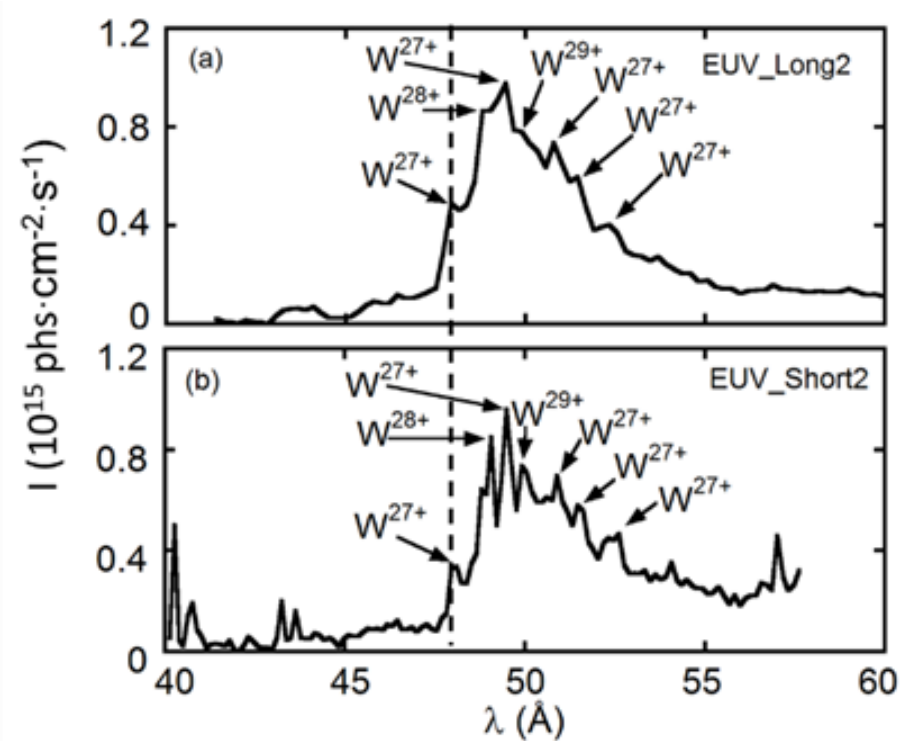

Fig. 3.3 Tungsten UTA spectra at t = 5.3 s measured with (a) EUV_Long2 and (b) EUV_Short2. It should be noticed that the apparent spectral resolution is not good in both the EUV_Long2 and EUV_Short2 because the binning is made in the CCD horizontal pixel for faster sampling time.

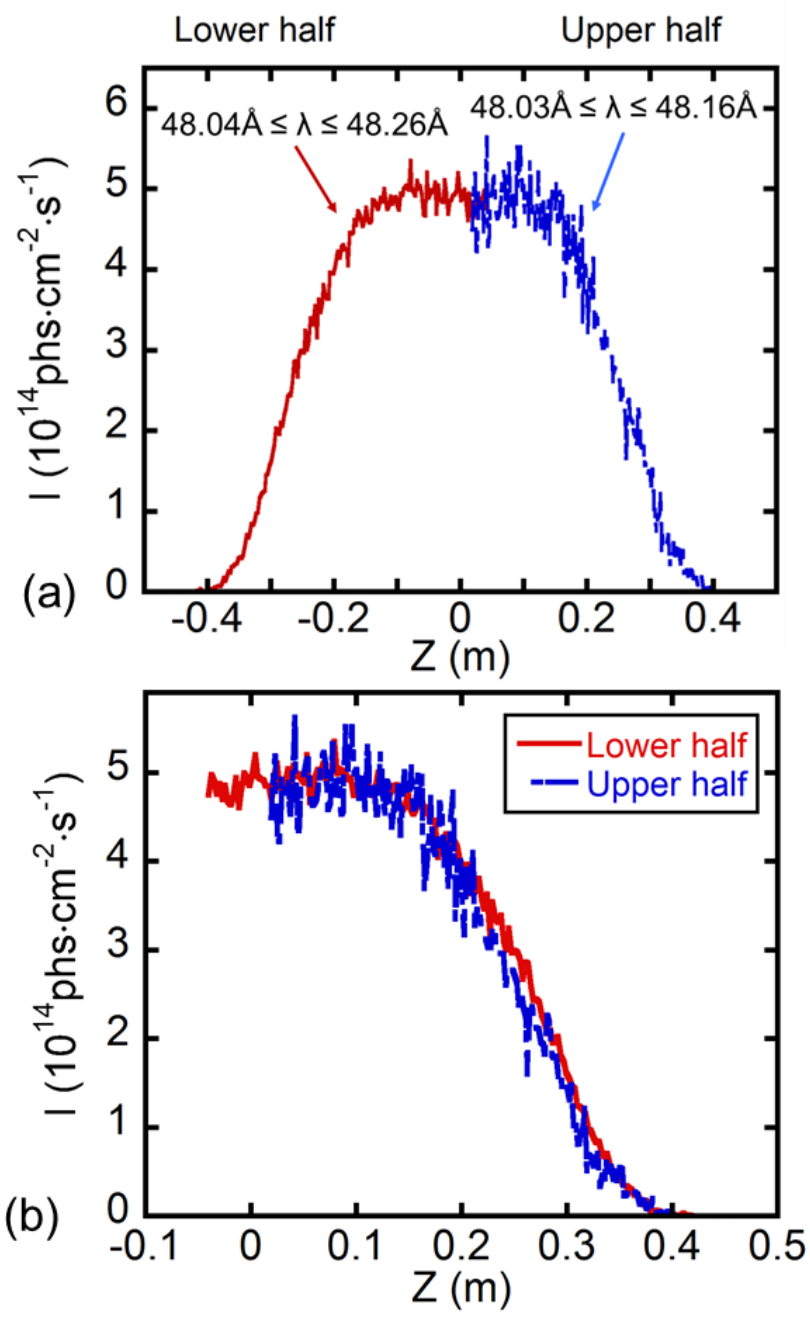

Fig. 3.4 (a) Vertical profiles of WXXVIII at lower- (solid line) and upper-half (dashed line) plasma radii at t = 5.3 s measured with EUV_Long2 and EUV_Short2, respectively, and (b) lower-half profile superimposed on upper-half profile.

The unresolved transition array (UTA) spectra from tungsten ions measured at 5.3 s are shown for EUV_Long2 and EUV_Short2 in Fig. 3.3 with wavelength range of 40-60 Å, while the observed ranges of EUV_Long2 and EUV_Short2 are 41-70 Å and 40-57 Å, respectively. The tungsten ionization stages are also denoted in the figures with arrows. It should be noted here that the tungsten ions seen in the UTA spectra are located in the plasma center at t = 5.3 s and the centrally peaked emission profile can give more accurate analysis on the up-down asymmetry. The identification is done with EUV spectra measured by a high-time response EUV_Short spectrometer without spatial resolution [7]. It is noted here that the spectral resolution of EUV_Short is considerably high in this wavelength range compared to EUV_Long [8], as shown in Fig. 3.3. The UTA spectra are usually appeared in the electron temperature range of 1-2 keV at wavelength interval of 45-70 Å. Since the UTA consists of many transitions from tungsten ions in different ionization stages and the spectral lines overlap each other, it is often difficult to extract an emission line.

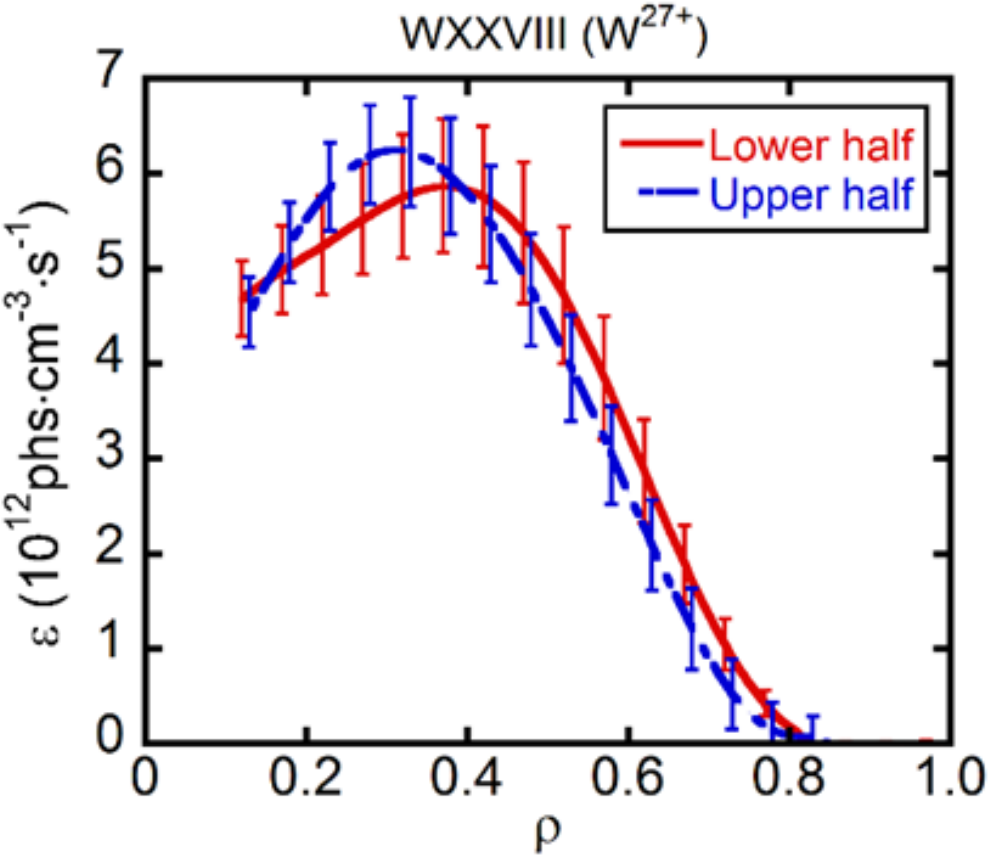

Fig. 3.5 Local emissivity profiles of WXXVIII at lower- (solid line) and upper-half (dashed line) plasma radii reconstructed with Abel inversion method.

The vertical profiles at 5.3 s (0.5 s after tungsten pellet injection) extracted from single channel near 48 Å are plotted in Fig. 3.4. The ionization stage of tungsten at the wavelength is believed to be W^{27+} ions. The lower-half profile in Fig. 3.4(a) is taken from EUV_Long2 data at wavelength interval of 48.04 Å $\leq \lambda \leq$ 48.26 Å and the upper-half profile is taken from EUV_Short2 data at wavelength interval of 48.03 Å $\leq \lambda \leq$ 48.16 Å. In order to extract the wavelength interval shown in Fig. 3.4(a), we have carefully checked the vertical profiles in the whole wavelength range of UTA shown in Fig. 3.3. In several profiles at different wavelengths in the UTA the second peak appears in addition to the central peak indicating certain tungsten emission from lower ionization stages is blended. Such data are avoided from the present analysis.

In order to examine the apparent up-down asymmetry, the lower-half profile is superimposed on the upper-half profile. The result is shown in Fig. 3.4(b). It is understood that the two vertical profiles almost overlap each other at every vertical position, suggesting no asymmetry obviously exists. Due to a different arrangement of EUV_Long2 and EUV_Short2 shown in Fig. 3.1, the observation chord length and angle in plasmas are slightly different between EUV_Long2 and EUV_Short2. The effect of different arrangements on the asymmetry study may be not negligible. Therefore, the up-down asymmetry is also examined against the local emissivity profile.

The radial profile of local emissivity is analyzed by reconstructing the measured vertical profile based on the Abel inversion method, in which the magnetic surface necessary for the analysis is calculated with VMEC code. The lower- and upper-half vertical profiles are separately analyzed based on the data in Fig. 3.4 with taking into account the wavelength-dependent intensity calibration factor for both the spectrometers. Since a relatively large spike noise appears in the vertical profile from EUV_Short2, which is caused by high-energy neutrals originating in NBI fast ions, a polynomial fitting is applied in analyzing the vertical profile. A series of intersections is obtained based on the observation chords and magnetic surfaces calculated with VMEC code, and unit chord length between two adjacent magnetic surfaces is then calculated for all the observation chords. The local emissivity, $\varepsilon(\rho)$, is then obtained by the following equation:

$$I(r) = \Sigma\, \varepsilon(\rho)\, \Delta l, \qquad (1)$$

where $I(r)$ and Δl represent the emission intensity in the vertical profile and unit chord length. The local lower- and upper-half emissivity profiles analyzed for WXXVIII emission are plotted in Fig. 3.5. It also shows the same result as Fig. 3.4(b). No significant difference showing the asymmetry is found at least in the present experimental condition.

It is then understood that the effect of different arrangements between the two spectrometers is entirely small.

In summary, the emissivity profile of tungsten ions is symmetric within the data uncertainty at the present discharge condition. It should be also mentioned that the present method of utilizing two space-resolved EUV spectrometers to simultaneously observe the full vertical profile can work well for the asymmetry study of heavier impurity ions.

References

[1] L.C. Ingesson, et al., Plasma Phys. Controlled Fusion 42, 161 (2000).
[2] K.D. Marr, et al., Plasma Phys. Controlled Fusion 52, 055010 (2010).
[3] K. Indireshkumar, et al., Phys. Fluids B 5, 1850 (1993).
[4] T. Fulop, et al., Phys. Plasmas 18, 030703 (2011).
[5] C.F. Dong, et al., Rev. Sci. Instrum. 81, 033107 (2010).
[6] X. Huang, et al., Rev. Sci. Instrum. 85, 043511 (2014).
[7] M.B. Chowdhuri, et al., Appl. Opt. 47, 135-146 (2008).
[8] M.B. Chowdhuri, et al., Rev. Sci. Instrum. 78, 023501 (2007).

Chapter 4

Component investigation of ionization stages on tungsten UTA spectra

4.1. Introduction

Tungsten with a large atomic number of 74 is planned to be used as the most suitable material for the PFCs in the ITER tokamak instead of carbon materials which have been used for many years in toroidal devices [1, 2]. However, the radiation loss from tungsten ions has a serious effect on plasma performance, once the tungsten concentration exceeds a certain threshold level in the core plasma. In the ITER operation, therefore, the tungsten density in plasma core, n_W, must be maintained at a low level against the electron density, n_e, e.g. $n_W/n_e < 10^{-5}$ [3]. The tungsten transport study is then extremely important for controlling the tungsten accumulation in the plasma core and reducing the tungsten influx in the plasma edge.

On the other hand, understanding of the tungsten spectra which are useful for the diagnostics and transport study is still insufficient at present [4-6], whereas the spectra and related atomic data in medium-Z elements such as iron are well understood in conducting

impurity diagnostics based on numerous past works which have been done in both fields of plasma spectroscopy and atomic physics [7-10]. Thus, study on the tungsten spectroscopy has been carried out in Large Helical Device (LHD) with graphite divertor plates and stainless steel first wall. Since the LHD discharge is totally tolerant for the impurity buildup due to the absence of the plasma current, the tungsten experiment is possible over a wide range of the tungsten concentration, which leads to higher brightness in tungsten line emissions. In LHD the tungsten spectra are observed by injecting a coaxial graphite pellet with a small amount of tungsten, because use of the traditional laser-blow-off method seems to be difficult due to the presence of a thick stochastic magnetic field layer surrounding the core plasma, which can largely enhance the impurity screening in the plasma peripheral region and reduce the impurity flux toward the main plasma [10].

The ionization energy, E_i, of tungsten ions is plotted in Fig. 4.1 as a function of charge state [11]. When the electron temperature at plasma radius where a certain tungsten ion stays is equal to the ionization energy, E_i, of the tungsten ion, the T_e range in neutral beam (NB) heated discharges of LHD can be also plotted in the figure, as denoted with shaded area. Electron temperature ranges at edge, scrape-off layer (SOL) and divertor plasmas of ITER are also denoted with areas surrounded by horizontal dashed lines [12, 13]. Since the central electron temperature of ITER is very high, the charge state of tungsten ions becomes also extremely high in the central plasma region, e.g. W^{70+}-W^{72+}. The atomic configurations of such ions are relatively simpler because such ions only have a few orbital electrons. It means the spectral analysis of line emissions from such Be- and Li-like tungsten ions is easier. On the other hand, the tungsten ions staying in edge plasmas of ITER still have many orbital electrons forming a complicated atomic structure. Therefore, the spectroscopic study on tungsten ions with many orbital electrons in LHD can give valuable information for the edge plasma diagnostics of ITER in addition to a contribution to the atomic physics.

Until now several spectral lines from tungsten ions in low charge states including neutral tungsten have been observed from magnetically confined fusion plasmas. A neutral tungsten emission, WI, has been observed in visible range at 4009 Å [14-18]. The neutral line has been now widely used for the plasma wall interaction study [19-21]. Line emissions from weakly ionized tungsten ions, WIV-VII, have been observed in vacuum ultraviolet (VUV) range of 500-1500 Å using a 3 m space-resolved VUV spectrometer with good spectral resolution. The ion temperature is then evaluated from Doppler broadening measurement of WV-VI lines [22]. The WXLV (W^{44+}) and WXLVI (W^{45+}) emissions have been already observed from many devices in extreme ultraviolet (EUV) range in the vicinity of 60 Å and 130 Å [17, 18, 23-25]. Those spectra can be basically isolated from other tungsten lines because the electronic configuration is relatively simple [17].

However, the understanding on spectral lines from WXXII (W^{21+}) to WXLIV (W^{43+}) is entirely insufficient due to the complicated electronic configuration.

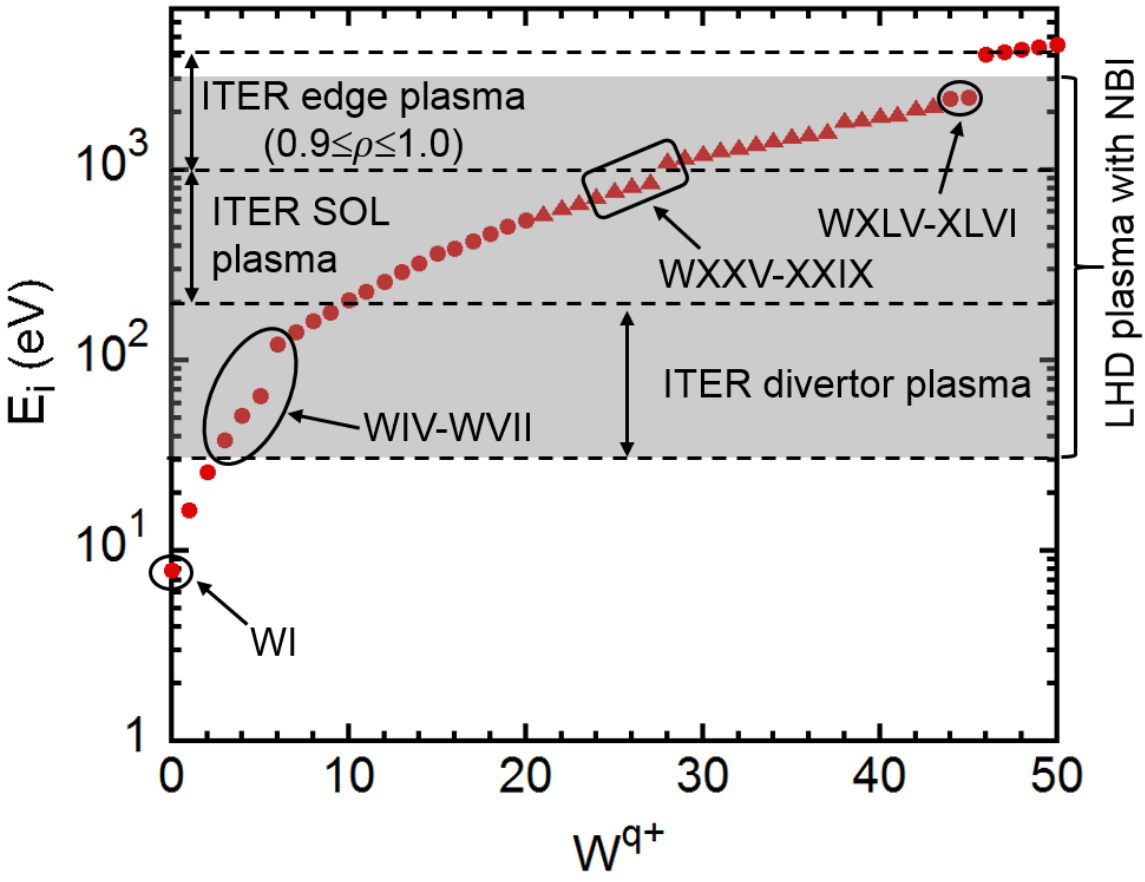

Fig. 4.1 Ionization energy, E_i, as a function of charge state of W ions, W^{q+}. Electron temperature ranges of ITER at $T_e = E_i$ are indicated with horizontal dashed lines for edge ($0.9 \leq \rho \leq 1.0$), SOL and divertor plasmas as 1-4, 0.2-1.0 and 0.03-0.20 keV, respectively. Electron temperature range of LHD NBI plasmas is denoted with gray-hatched area. Ionization stages in W UTA spectra are denoted with solid triangles at WXXII-XLIV (W^{21+}-W^{43+}). WI (W^{0+}), WIV-VII (W^{3+}-W^{6+}) and WXLV-XLVI (W^{44+}-W^{45+}) have been already identified in visible [14-18], VUV [22] and EUV [17, 18, 23-25] wavelength ranges, respectively.

Since a lot of tungsten emission lines from W^{21+} to W^{43+} ions are emitted at a narrow wavelength interval in the EUV range, a resultant spectrum becomes a pseudo-continuum called unresolved transition array (UTA) in fusion plasmas [23-35]. Therefore, the tungsten UTA spectra have been studied with EBIT and CoBIT [34] in which the tungsten spectra can be separately observed at each ionization stage. Based on these devices, tungsten lines in many ionization stages have been accurately identified by changing the electron beam energy. It is then attempted to reconstruct the UTA spectrum observed from LHD plasmas by superposing two UTA CoBIT spectra taken at different beam energies [17]. Although the LHD UTA spectrum can be roughly explained with the superposed CoBIT spectrum, a detailed analysis on the ionization stage in the UTA spectrum is still difficult. A model calculation has been also carried out to explain the LHD UTA spectrum by assuming the ionization equilibrium [35]. Effects of inner-shell excitations and configuration interaction are newly considered in the model, while a contribution from recombination processes is still remained as an open question. Nevertheless, the model calculation can well explain the LHD UTA spectrum by choosing a certain electron temperature. Despite those efforts, the present knowledge on the UTA spectra is still not applicable to the plasma diagnostics and transport study.

In the present paper alternative methods are attempted to investigate the component of ionization stages in the UTA at 20-70 Å by correlating the spectral intensity with electron temperature and by measuring the radial intensity profile. An accurate wavelength calibration is also done to determine a precise position of the wavelength interval in the UTA spectrum. The results are summarized in tables with determined ionization stages as a function of the wavelength interval.

4.2. Experimental setup

A grazing-incidence EUV spectrometer called EUV_Short is installed on LHD to observe impurity line emissions in the wavelength range of 10-130 Å. A typical value of the wavelength range is $\Delta\lambda$ = 65 Å (13 Å $\leq \lambda \leq$ 78 Å) at central wavelength of λ_0 = 40 Å. Many well-known line emissions from intrinsic impurities such as helium, carbon and iron exist in this wavelength range with strong emission intensities. Those emissions are useful for the precise wavelength calibration of the spectrometer. EUV_Short is characterized by high temporal and spectral resolutions, while it has no spatial resolution. In the present

study, the EUV_Short spectrometer is used not only for the line identification of tungsten emissions but also for the wavelength calibration of spectral lines measured by other two space-resolved spectrometers which have relatively lower spectral resolutions due to a multi-pixel binning in direction of the wavelength dispersion as described below.

In order to observe the tungsten spectra, a co-axial impurity pellet has been injected to neutral-beam heated LHD discharges. The co-axial impurity pellet consists of a cylindrical graphite or polyethylene bullet with a thin tungsten wire inserted in the center axis [36]. A cylinder with a length of 0.7 mm^{L} and a diameter of 0.7 mm^{ϕ} is generally used for spectroscopic study. The size of the impurity wire is adjusted in ranges of 0.03-0.3 mm^{ϕ} and 0.5-0.8 mm^{L} according to the atomic number of impurity and experimental conditions.

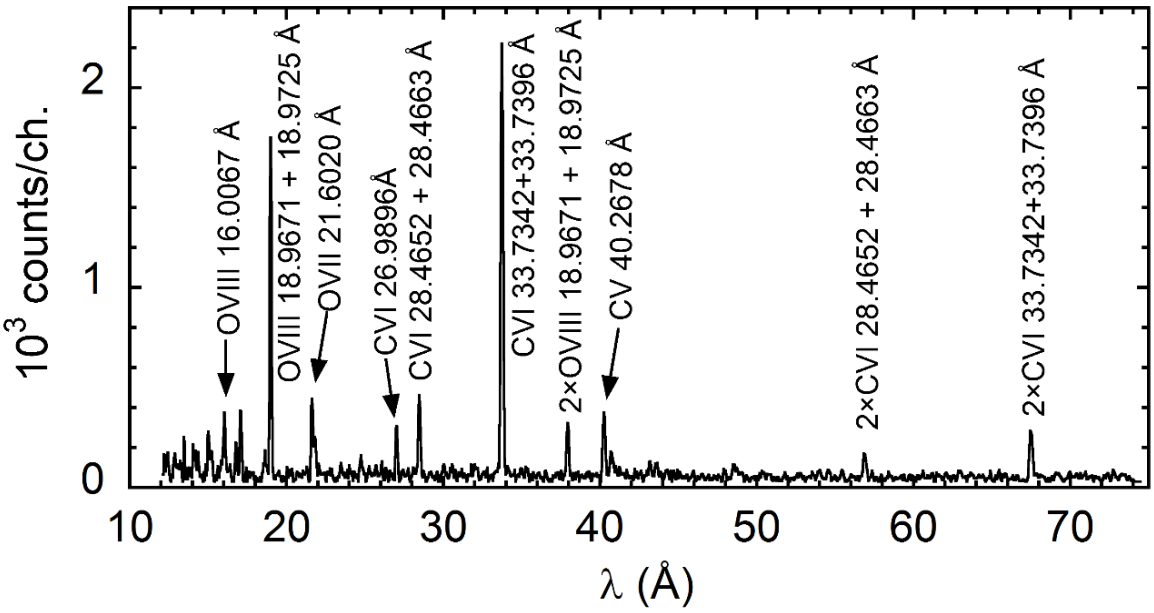

Fig. 4.2 Typical EUV spectrum at 10-75 Å in NBI discharges of LHD with carbon divertor plates and stainless steel first wall. Several well-known carbon and oxygen lines are observed in the spectrum.

4.3. Wavelength calibration of EUV spectrum

The EUV spectra of tungsten have been observed including the UTA spectra using the EUV_Short spectrometer with horizontal dispersion. Since the UTA with a lot of line emissions forms a pseudo-continuum spectrum, a precise wavelength calibration is needed to indicate an exact position of the spectrum. The wavelength position on the CCD is then experimentally calibrated using resonance transitions of light impurities because their wavelengths are accurately determined. Hydrogen-like carbon and oxygen lines are mainly used in the wavelength range of 10 Å $\leq \lambda \leq$ 70 Å, since helium-like transitions are relatively weak and other impurity line emissions are usually absent in general LHD discharges. In general, an effect of plasma rotation on the wavelength shift of impurity line emissions in edge plasmas is much less than 0.01 Å at λ = 50 Å, and the resultant wavelength shift is entirely smaller than the spectral resolution of the present EUV spectrometers.

A typical spectrum taken from EUV_Short is shown in Fig. 4.2. The 2p-1s first resonance transitions of CVI (33.7342 Å) and OVIII (18.9671 Å), the 3p-1s second resonance transitions of CVI (28.4652 Å) and OVIII (16.0067 Å) and 4p-1s resonance series transition of CVI (26.9896 Å) are clearly observed in addition to their second order light of OVIII (2 × 18.9671 Å), CVI (2 × 28.4652 Å) and CVI (2 × 33.7342 Å). When the electron density in LHD discharges is relatively high, e.g. $8x10^{13}cm^{-3}$, and the impurity line emissions are sufficiently strong, the $1s2p\text{-}1s^2$ first resonance transitions of helium-like CV (40.2678 Å) and OVII (21.6020 Å) can be also used for the wavelength calibration.

A typical result on the wavelength calibration is shown in Fig. 4.3(a) as a function of channel numbers of the CCD, N. Ten spectral lines emitted at wavelengths of λ_i are used in the calibration as mentioned above. The wavelength positions are plotted with solid circles in Fig. 4.3(a). A cubic polynomial fitting is then applied to link the ten spectral lines. The result is also shown in Fig. 4.3(a) with solid line. The wavelength position, λ_{exp}, is thus accurately obtained by the data fitting as a function of N as expressed in Fig. 4.3(a). Here, the number of CCD channels (1024 channels) in the horizontal axis is equal to the number of CCD pixels (1024 pixels) because the data are taken in the full binning mode.

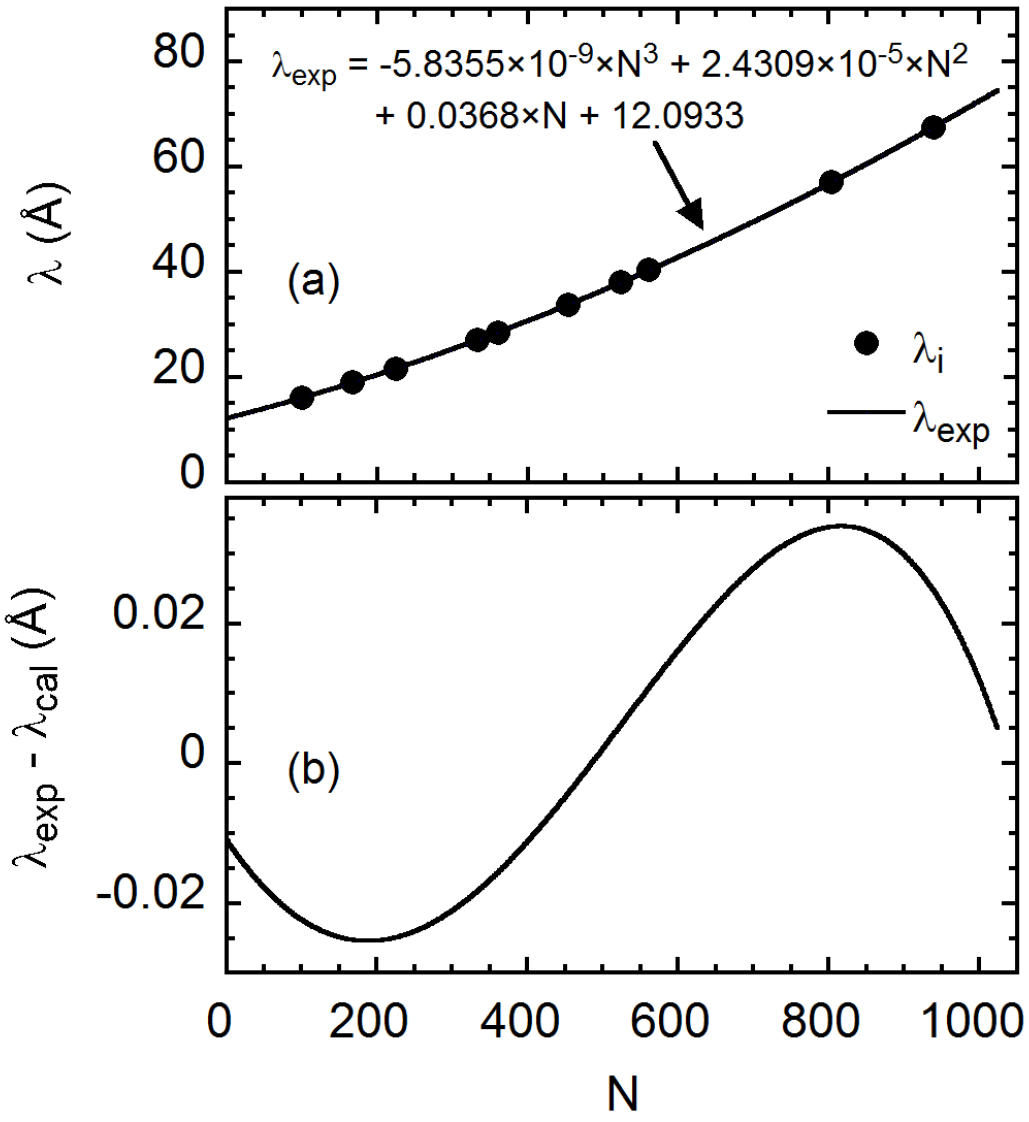

Fig. 4.3 (a) Cubic polynomial fitting (solid line: λ_{exp}) with ten well-known emission lines (solid circles: λ_i) and (b) deviation of experimentally determined wavelengths (λ_{exp}) from theoretically calculated wavelengths (λ_{cal}) as a function of channel numbers of CCD, N.

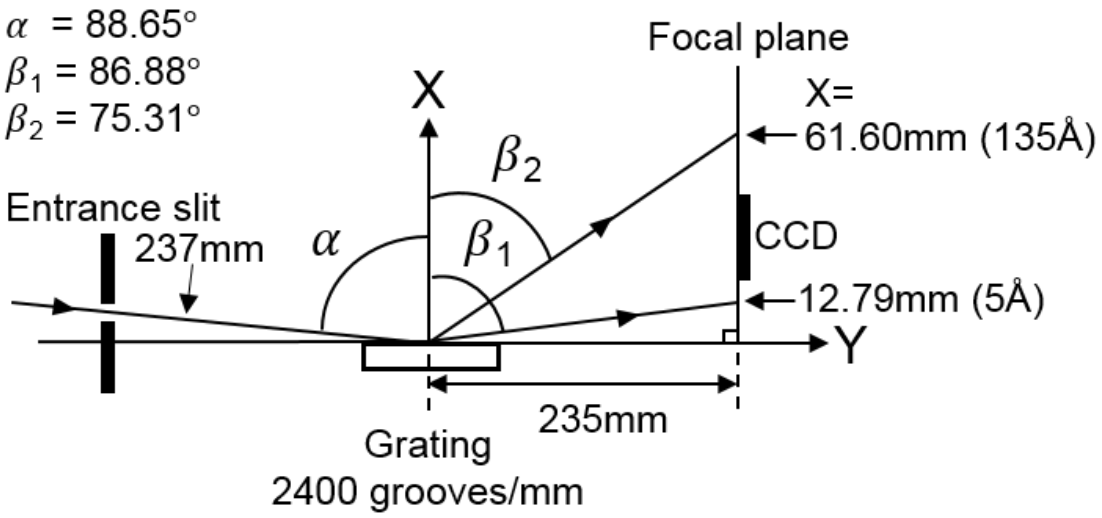

Fig. 4.4 Optical layout of EUV_Short spectrometer. Two axes of X and Y are perpendicular and parallel to 2400 grooves/mm grating surface, respectively. CCD moves along X axis to change the wavelength interval for observation. Distances from entrance slit to grating center (X=0, Y=0) and from grating center to focal plane are 237 and 235 mm, respectively. Angle of incidence, α, is fixed to 88.65° and output angles, β, is a function of wavelength, e.g. 75.31° (β_2) at 135 Å and 86.88° (β_1) at 5 Å.

The wavelength position can be also theoretically calculated from the spectrometer geometry. The EUV emissions from LHD plasmas are diffracted by the holographic grating after passing through an entrance slit, and then recorded by the CCD, as shown in Fig. 4.4. The diffracted EUV emission is focused on the focal plane as a function of wavelength, satisfying the following equation of

$$m\lambda = d\,(\sin\alpha + \sin\beta), \qquad (1)$$

where m, λ, d, α, and β stand for the diffraction order, the wavelength of incident light, the groove spacing of grating, the angle of incidence and the diffraction angle, respectively. As

the CCD is placed parallel to the X axis and the distance from the grating center to the focal plane is 235 mm, the wavelength position on the CCD, X_{CCD}, is given by

$$X_{CCD}(\lambda) = 235 \times \tan(90 - \beta). \quad (2)$$

Combining two equations of (1) and (2), we can obtain the theoretically calculated wavelength position, λ_{cal}.

The deviation of λ_{exp} from the λ_{cal} is plotted in Fig. 4.3(b) as a function of channel numbers of CCD. Here, the λ_{cal} is normalized to λ_{exp} at CVI (33.7342 Å) which is the strongest emission line in the EUV range. The difference between λ_{exp} and λ_{cal} indicates an obvious deviation between actual and designed dimensions in the setting of optical components. Although design parameters of the EUV spectrometer are mainly determined by the angle of incidence and the positions of entrance slit, grating and CCD, it is unknown at present which parameter the deviation is caused by. Anyway, the difference is within 0.025 Å. Then, the error in the wavelength determination can be estimated to be smaller than 0.01 Å.

4.4. Component investigation of UTA spectra based on electron temperature

4.4.1 UTA spectrum at 15-70 Å

A series of experiments on the tungsten UTA study have been carried out in LHD by injecting a tungsten pellet. A typical discharge with a tungsten pellet is shown in Fig. 4.5. A large coaxial tungsten pellet (tungsten wire: 0.15^{ϕ} mm in diameter × 0.6^{L} mm in length, polyethylene cylinder: $0.6^{\phi} \times 0.6^{L}$ mm) is injected from a mid-plane port at t = 3.8 s in neutral beam injection (NBI) discharges. Here, it is noted that the 0.15^{ϕ} mm tungsten pellet is the maximum size which can avoid the radiation collapse. The discharge is maintained by three negative-ion-source-based neutral beams (n-NBI#1, #2 and #3) with energy of 180 keV during 3.3-5.8 s (see Fig. 4.5(a)). After the pellet injection, the radiation power in Fig. 4.5(d) quickly increases reflecting huge radiation from tungsten ions. The

line-averaged electron density in Fig. 4.5(b) continues to increase from 2.5×10^{13} cm^{-3} to 6×10^{13} cm^{-3} during 0.4 s after the pellet injection. The number of particles injected by the pellet is $\Delta n_C = 6 \times 10^{18}$ and $\Delta n_W = 6.7 \times 10^{17}$ for carbon and tungsten, respectively. When C^{6+} and W^{45+} ions are regarded as the average ionization charges with the LHD plasma volume of 30 m^3, we obtain an average density rise caused by carbon and tungsten ions, i.e. $\Delta n_e(C) = 1.2 \times 10^{12}$ cm^{-3} and $\Delta n_e(W) = 1.0 \times 10^{12}$ cm^{-3}. Then, the total density rise caused by the tungsten pellet is estimated to be 2.2×10^{12} cm^{-3}. However, the real density rise is 4×10^{13} cm^{-3} as shown in Fig. 4.5(b) which is much larger than the estimation. In general LHD discharges, an effect of the particle screening is extremely large due to the presence of edge stochastic magnetic field layer [10]. When the edge temperature decreases below a certain threshold value, the screening effect immediately disappears from the edge plasma due to plasma size becomes smaller. Most of discharges after the large tungsten pellet injection show a disappearance of the edge screening effect. Therefore, the large density increase after the tungsten pellet injection is brought by an increase in hydrogen influx, but not by the pellet injection.

With increasing the electron temperature, the density begins to decrease. The density decay is very long and continues during the following 2 s until the end of constant NBI pulse at t = 5.8 s. The density continuously decreases from 6×10^{13} to 3×10^{13} cm^{-3} but the temperature continuously increases from 0.3 to 3.0 keV. Thus, the recombining phase just after the pellet injection entirely changes to the ionizing phase and the ionizing phase is maintained during the following 2 s. The ionization of tungsten ions sequentially proceeds in the plasma center as a function of time during the ionizing phase with temperature recovery. Therefore, the transport does not give a significant effect on the temporal behavior of tungsten line emissions during the temperature recovery phase. In addition, the effect of the transport is generally weak for partially ionized ions in high-Z impurities, e.g. ions composing the UTA lines, because the temperature window where such ions can exist is very narrow in the ionization equilibrium. The density effect on the ionization equilibrium is also small in the present density range.

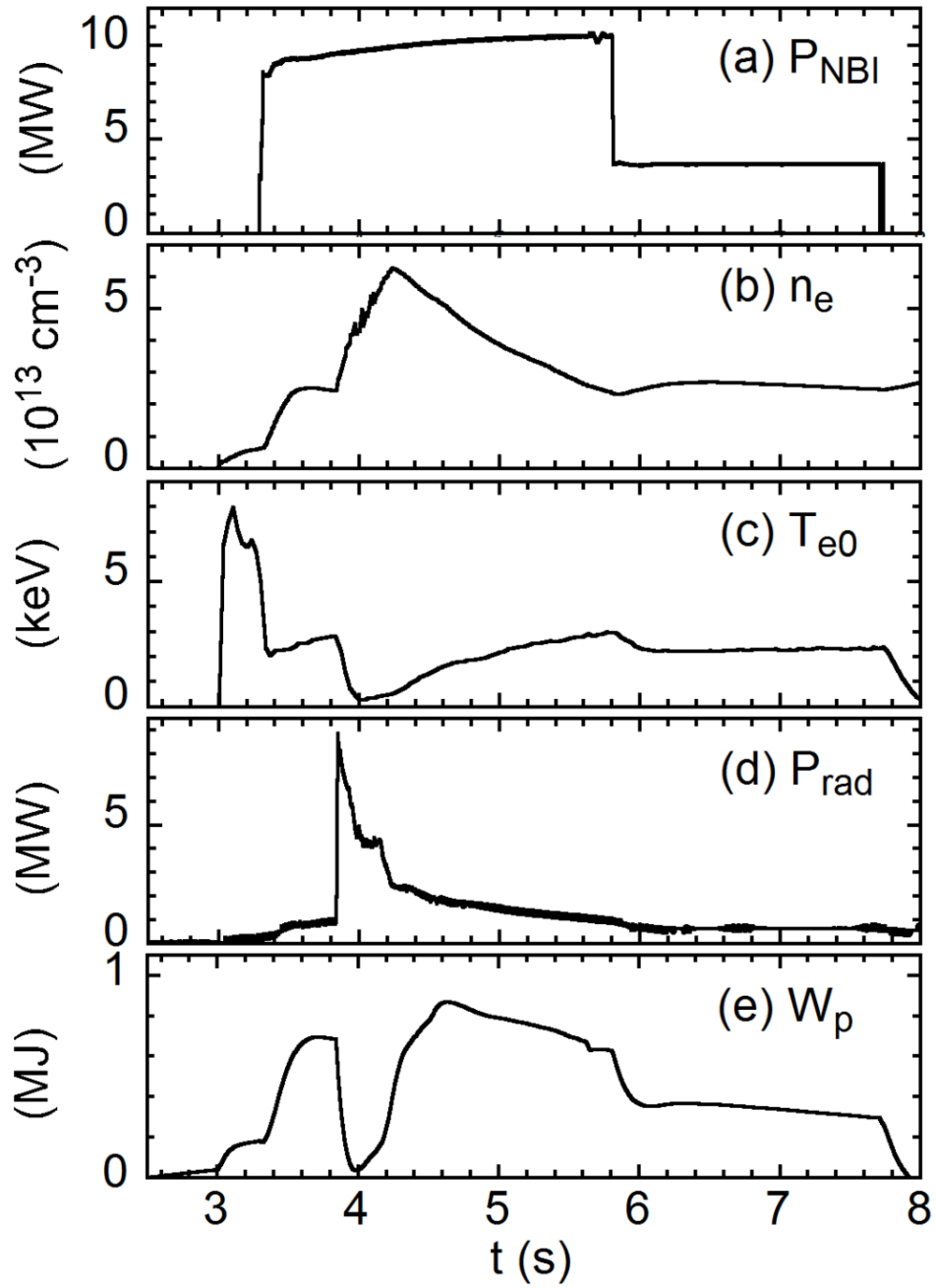

Fig. 4.5 Time behaviors of (a) NBI port-through power, (b) line-averaged electron density, (c) central electron temperature, (d) total radiation power and (e) plasma stored energy. A coaxial graphite pellet (0.6 $mm^{\phi} \times 0.6\ mm^{L}$) with tungsten wire size of 0.15 $mm^{\phi} \times 0.6\ mm^{L}$, which is the maximum size of tungsten to avoid the radiation collapse, is injected at t = 3.8 s.

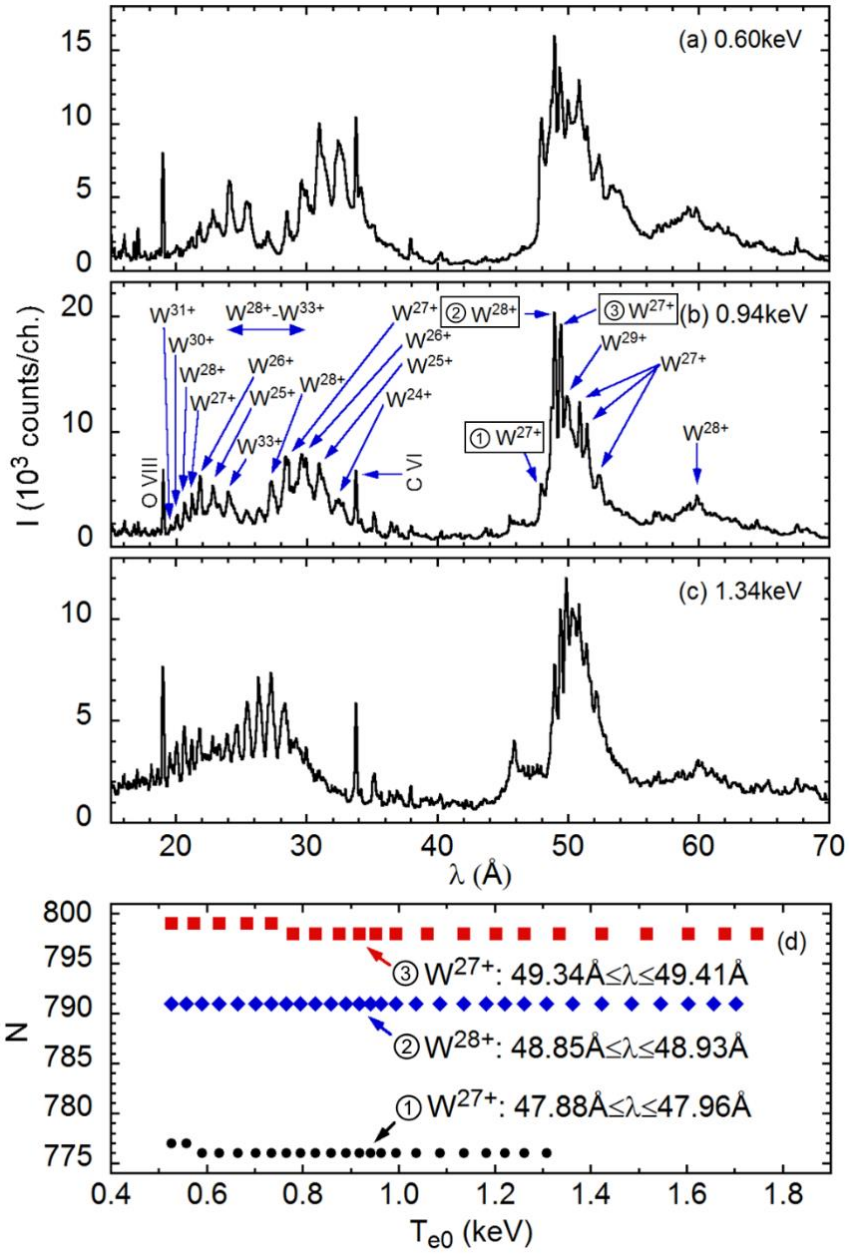

Fig. 4.6 Tungsten spectra with UTA in wavelength range of 15-70 Å at (a) t = 4.37 s (0.60 keV), (b) 4.50 s (0.94 keV) and (c) 4.67 s (1.34 keV), and (d) CCD channel number at intensity peak of three emission lines of W^{27+} at 47.88-47.96 Å (solid circles), W^{28+} at 48.85-48.92 Å (solid diamonds) and W^{27+} at 49.34-49.41 Å (solid squares) as a function of central electron temperature, T_{e0}. Ionization stages denoted at 15-45 Å and 45-70 Å are referred by LHD data [17, 34, 35] and previous studies [4, 26, 27, 30, 33]. The three UTA lines in (d) are also denoted with square boxes in (b).

The tungsten spectra in the wavelength range of 15-70 Å are measured with EUV_Short spectrometer. Typical spectra obtained during the temperature recovery phase of 4.0 s to 5.8 s after the pellet injection in Fig. 4.5 are shown in Figs. 4.6(a)-(c), which are taken at different electron temperatures of T_e = 0.60 keV (t = 4.37 s), 0.94 keV (4.50 s) and 1.34 keV (4.67 s), respectively. The UTA emissions are characterized by two wavelength intervals of 15-45 Å and 45-70 Å. A possible investigation on the ionization stage is carried out by referring the past works from CoBIT and plasma devices [4, 17, 26, 27, 30, 34, 35] for the wavelength ranges of 15-45 Å and 45-70 Å, respectively. The observed spectrum involves not only many ionization stages of tungsten ions but also different transitions [17, 35]. The UTA in the 15-45 Å range consists of 6g-4f, 5g-4f, 5f-4d and 5g-4f transitions, while the UTA in the 45-70 Å consists of 4f-4d, 4d-4p and 5d-4f transitions.

It is clear that the UTA in the 15-45 Å range moves toward shorter wavelength side with increase in the electron temperature [17]. However, it must be pointed out that the peak position of each emission group does not move in both UTA groups, even if the electron temperature changes. In order to confirm it, the peak positions in three UTA lines of W^{27+} at 47.81-48.03 Å, W^{28+} at 48.78-48.99 Å and W^{27+} at 49.20-49.41 Å are plotted as a function of central electron temperature in Fig. 4.6(d) with labels of 1, 2 and 3, respectively. Although one channel shift appears in both W^{27+} ions labeled with 1 and 3 at low temperature ranges near 0.6-0.7 keV, it seems to be within uncertainty in estimating the peak position because the intensity is weak at such a low temperature range. The both emissions from W^{27+} ions at 47.81-48.03 Å and 49.20-49.41 Å are sufficiently strong at relatively high electron temperature ranges of T_{e0} > 0.6 keV and 0.75 keV, respectively. Therefore, it is confirmed that the peak positions of UTA line emissions do not move, even if the electron temperature changes. In the following two sections, the tungsten UTA spectra in 15-45 Å and 45-70 Å are separately analyzed against the electron temperature.

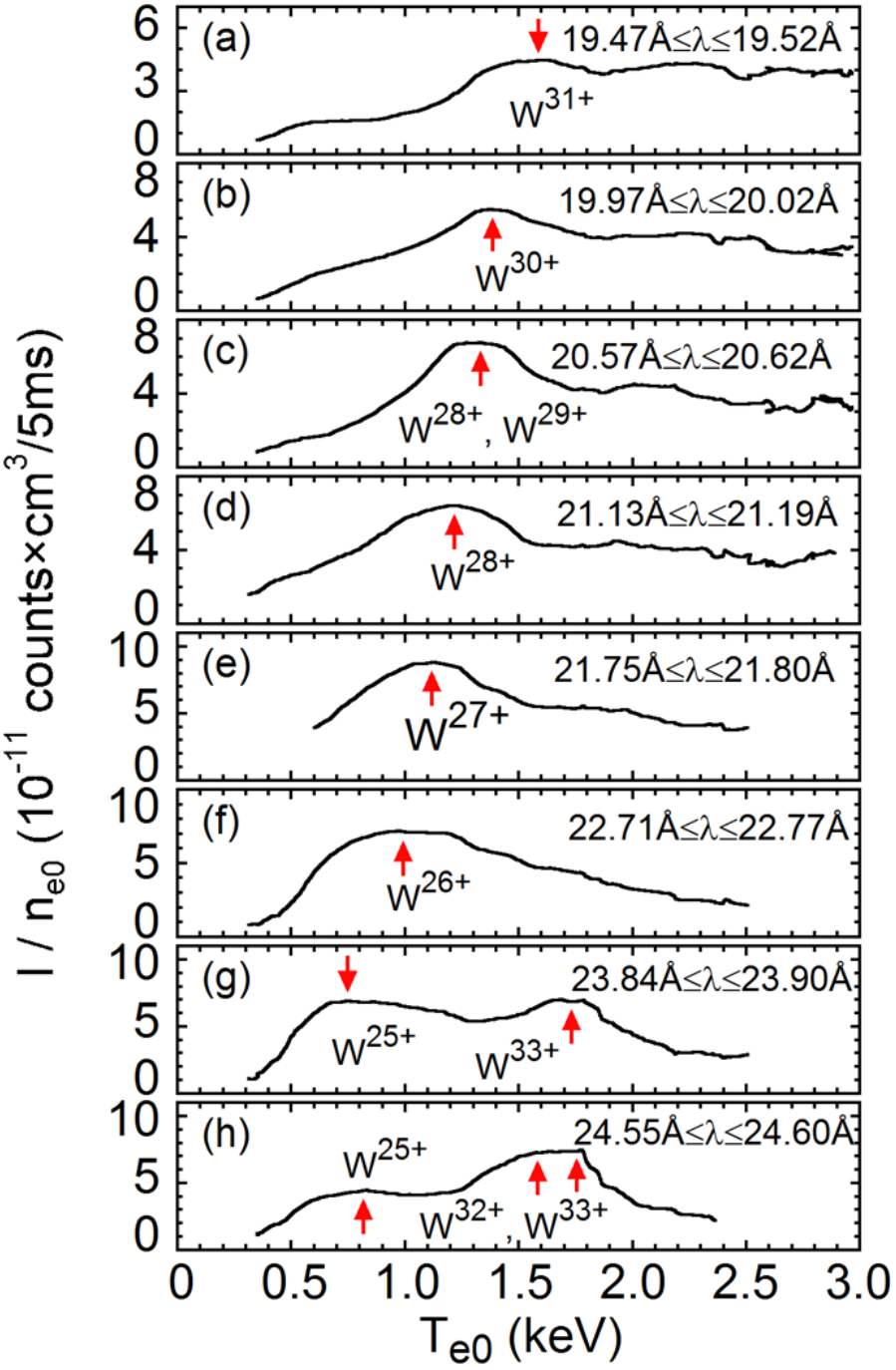

Fig. 4.7 Intensity of tungsten UTA lines at each wavelength interval of (a) to (o) in range of $19 \leq \lambda \leq 33$ Å as a function of central electron temperature, T_{e0}. The intensity is normalized to central electron density, n_{e0}. The wavelength interval is denoted at the top-right corner in each figure. The ionization stages are estimated from the electron temperature at the intensity peak denoted with vertical arrows.

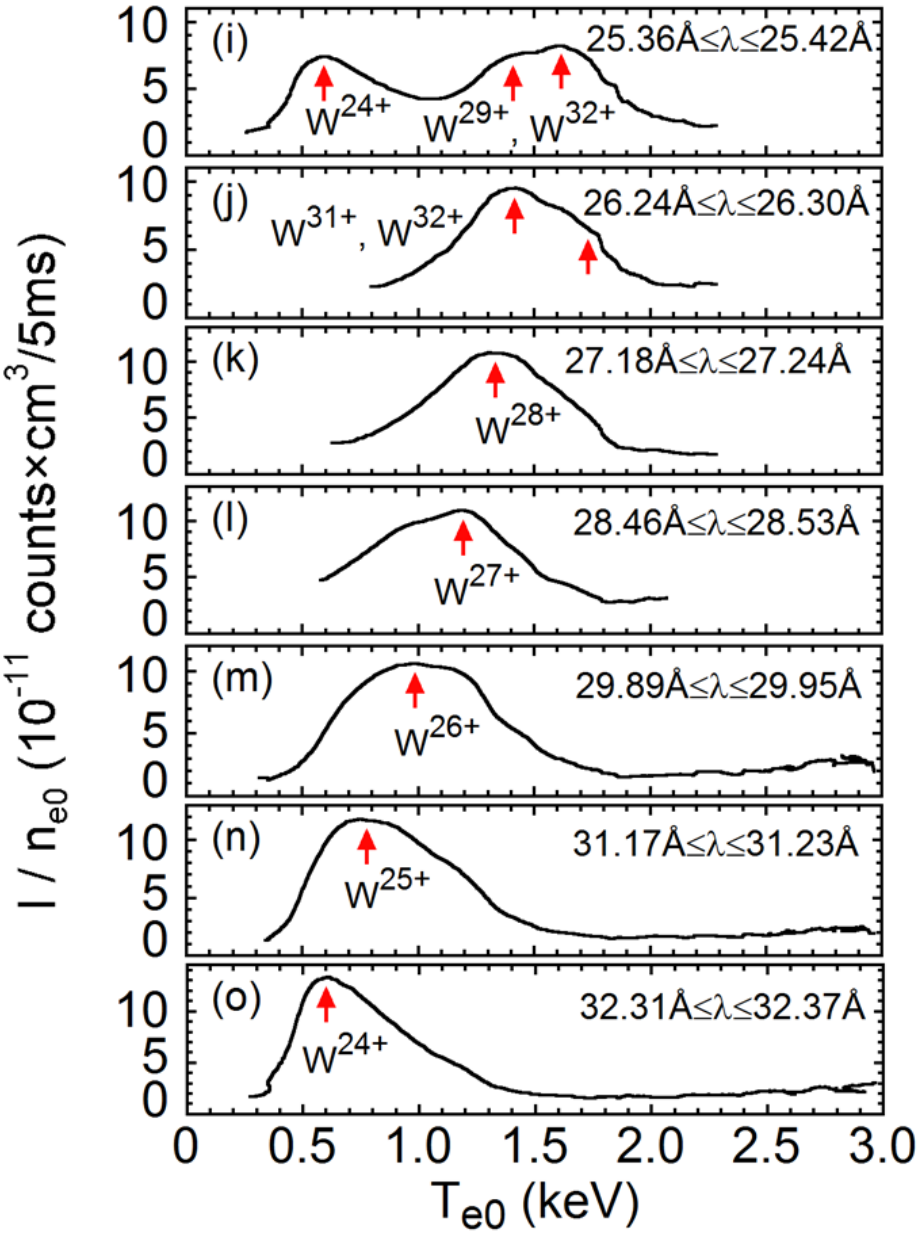

Fig. 4.7 (Continued.)

4.4.2 Analysis of tungsten UTA at 15-45 Å

The intensity of UTA lines at 15-45 Å is analyzed at the electron temperature recovery phase of 4.2 to 5.8 s shown in Fig. 4.5. A result of the analysis is shown in Fig. 4.7. The UTA intensity is normalized to the central electron density to cancel the linear effect from electron density. The UTA line intensity integrated over a certain wavelength interval, which is denoted at top-right corner of each graph, is plotted as a function of central electron temperature. It is found that the UTA line intensity has a peak value at a certain electron temperature. The ionization stage can be then estimated from the electron temperature at the peak intensity because the electron temperature is closely related to the ionization energy of tungsten ions. Previous studies on the UTA spectral analysis [11, 17, 26, 27, 30, 33] are also referred in the present estimation. The ionization stage estimated in the present study is indicated with an arrow in Fig. 4.7. When the intensity has multiple peaks for a certain wavelength interval, two or three different ionization stages estimated from the multiple peaks are denoted in Fig. 4.7, e.g. (g) 23.84-23.90 Å, (h) 24.55-24.60 Å and (i) 25.36-25.42 Å. The wavelength intervals of (a) 19.47-19.52 Å, (b) 19.97-20.02 Å, (c) 20.57-20.62 Å, (d) 21.13-21.19 Å, (e) 21.75-21.80 Å and (f) 22.71-22.77 Å in Fig. 4.7 may also consist of a few ionization stages because the intensity is distributed in a wider electron temperature range. On the other hand, five wavelength intervals in Figs. 4.7(k)-(o) only have a single peak against the electron temperature. It means the UTA line involved in the wavelength interval consists of a single ionization stage. These UTA lines at wavelength intervals of (k) 27.18-27.24 Å, (l) 28.46-28.53 Å, (m) 29.89-29.95 Å, (n) 31.17-31.23 Å and (o) 32.31-32.37 Å in Fig. 4.7 clearly show a peak value at different electron temperatures of T_{e0} = 1.35, 1.20, 1.00, 0.80 and 0.60 keV, respectively. Thus, those five wavelength intervals shown in Figs. 4.7(k)-(o) are identified as W^{28+}, W^{27+}, W^{26+}, W^{25+} and W^{24+}, respectively [17, 26, 27, 30]. These wavelength intervals can be used for the tungsten diagnostic.

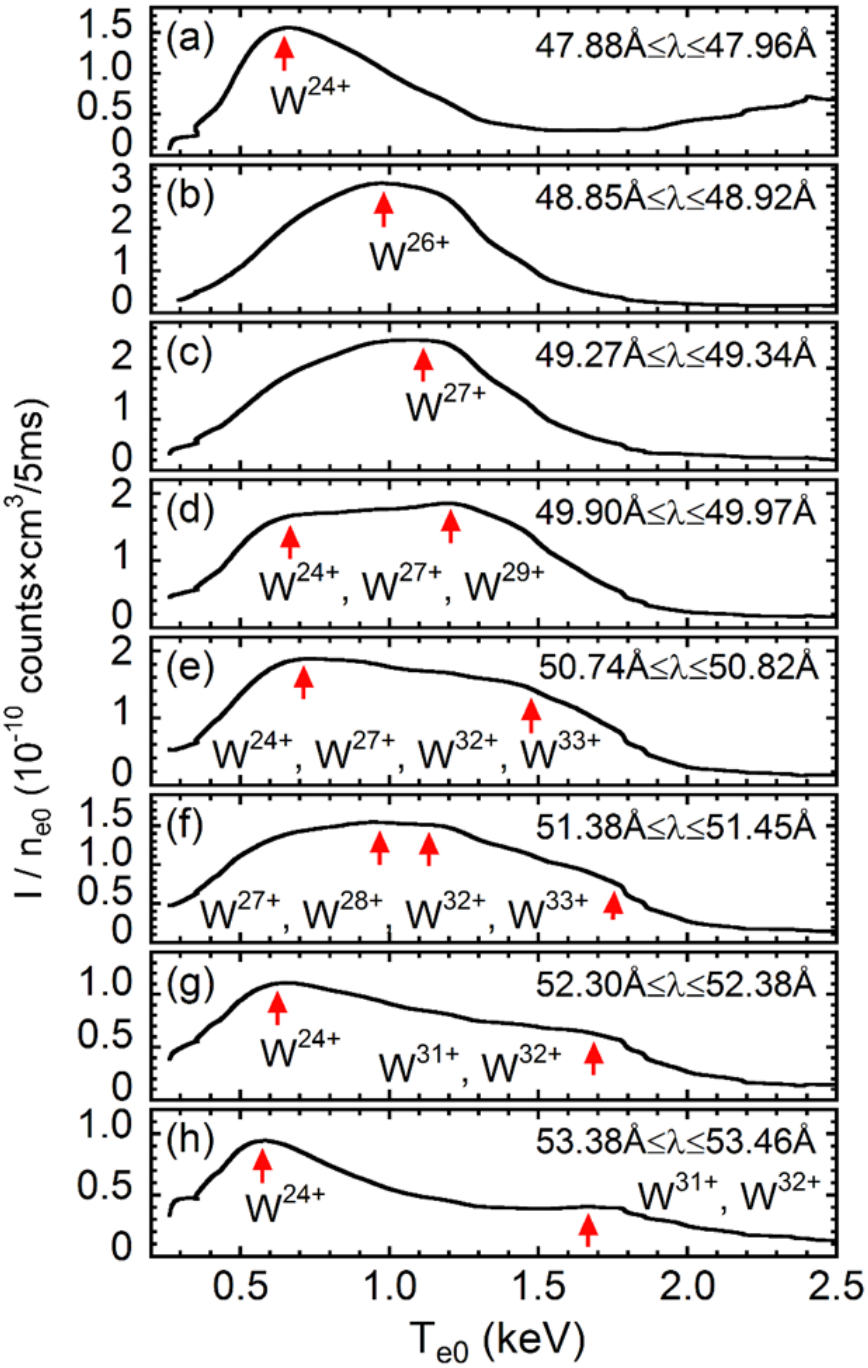

Fig. 4.8 Intensity of tungsten UTA lines at each wavelength interval of (a) to (h) in range of $47 \leq \lambda \leq 54$ Å as a function of central electron temperature, T_{e0}. The intensity is normalized to central electron density, n_{e0}. The wavelength interval is denoted at the top-right corner in each figure. The ionization stages are estimated from the electron temperature at the intensity peak denoted with vertical arrows.

4.4.3 Analysis of tungsten UTA at 45-70 Å

The intensity of tungsten UTA lines at 45-70 Å is also analyzed at the electron temperature recovery phase as a function of electron temperature as well as the former section. The result is shown in Fig. 4.8. The intensity is normalized to the central electron density as well as Fig. 4.7. As the wavelength range in which the tungsten UTA line is strong is limited around 50 Å (see Fig. 4.6), the analysis is focused on the wavelength range of 47-54 Å. Since the UTA intensity at wavelength intervals of (d) 49.90-49.97 Å, (e) 50.74-50.82 Å, (f) 51.38-51.45 Å, (g) 52.30-52.38 Å and (h) 53.38-53.46 Å in Fig. 4.8 is distributed in a wide electron temperature range, it is clear that such wavelength intervals consist of several ionization stages as denoted with arrows. On the contrary, the intensity distribution at the first three wavelength intervals of (a) 47.88-47.96 Å, (b) 48.85-48.92 Å and (c) 49.27-49.34 Å only has a single peak at 0.65, 1.0 and 1.1 keV, respectively. In the present analysis, therefore, the ionization stage at three wavelength intervals in Figs. 4.7(a)-(c) can be evaluated as W^{24+}, W^{26+} and W^{27+}, respectively.

The UTA line at wavelength interval of 47.88-47.96 Å in Fig. 4.8(a) was identified as W^{27+} in previous works [28, 33]. However, the electron temperature at which the intensity has a peak value is 0.65 keV as shown in Fig. 4.8(a). The behavior is obviously different from that at 28.46-28.53 Å evaluated as W^{27+} in Fig. 4.7(l). Since the intensity from W^{24+} ions at 32.31-32.37 Å in Fig. 4.7(o) takes a peak value around 0.6 keV, the UTA line at 47.88-47.96 Å in Fig. 4.8(a) can be also evaluated as W^{24+}. Although the UTA line at 48.85-48.92 Å was identified as W^{28+} in a previous work [33], it has peak intensity at the electron temperature of 1.0 keV as seen in Fig. 4.8(b). This result is similar to that at 29.89-29.95 Å in Fig. 4.7(m) evaluated as W^{26+}. Therefore, the UTA line in Fig. 4.8(b) can be also evaluated as W^{26+}. Since the UTA line intensity at 49.27-49.34 Å in Fig. 4.8(c) has a similar behavior to that at 28.46-28.53 Å in Fig. 4.7(l), it is evaluated as W^{27+} as well as the result in the previous paper [30, 33].

Temporal behaviors of the UTA line intensity at five wavelength intervals of 27.18-27.24 Å, 28.46-28.53 Å, 29.89-29.95 Å, 31.17-31.23 Å and 32.31-32.37 Å in Figs. 4.7(k)-(o), which are evaluated as the UTA line from a single ionization stage, are shown in Figs. 4.9(a)-(e), respectively. The intensity is normalized to the central electron density. When the electron temperature starts to recover, the UTA line from W^{24+} in Fig. 4.9(e) begins to appear at t = 4.12 s, i.e. 0.3 s after the pellet injection (see Fig. 4.5). Each UTA line reaches the peak intensity at different discharge times during the temperature recovery phase. The timing of the peak intensity denoted with vertical arrows systematically changes according to the ionization stage of tungsten ions, i.e. t = 4.27 s for W^{24+}, 4.33 s for W^{25+}, 4.38 s for

W^{26+}, 4.43 s for W^{27+} and 4.49 s for W^{28+}. Then, the figure also shows an experimental certification on the validity in the present evaluation.

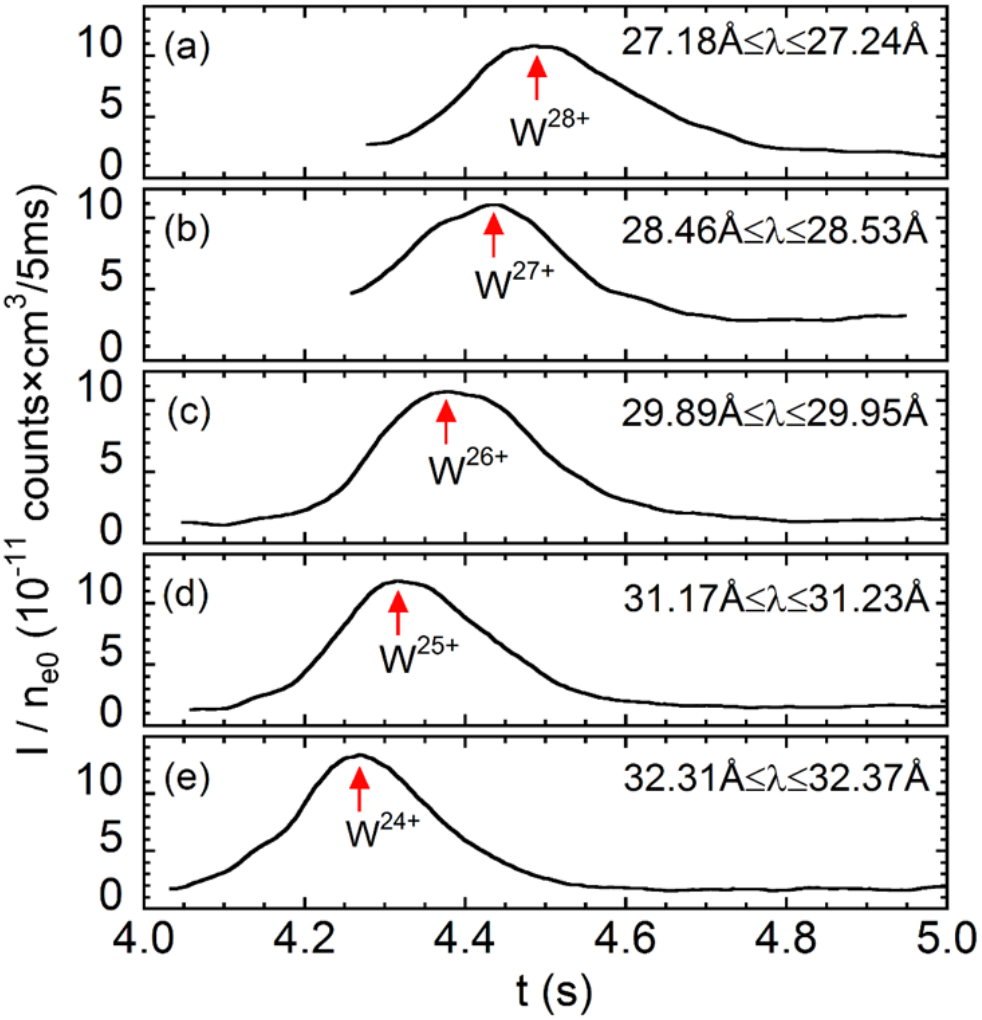

Fig. 4.9 Time behaviors of tungsten UTA line intensities at wavelength intervals of (a) 27.18 - 27.24 Å, (b) 28.46 - 28.53 Å, (c) 29.89 - 29.95 Å, (d) 31.17 - 31.23 Å and (e) 32.31 - 32.37 Å consisting of a single ionization stage of tungsten ions. The intensity is normalized to central electron density, n_{e0}. Tungsten pellet is injected at 3.82 s.

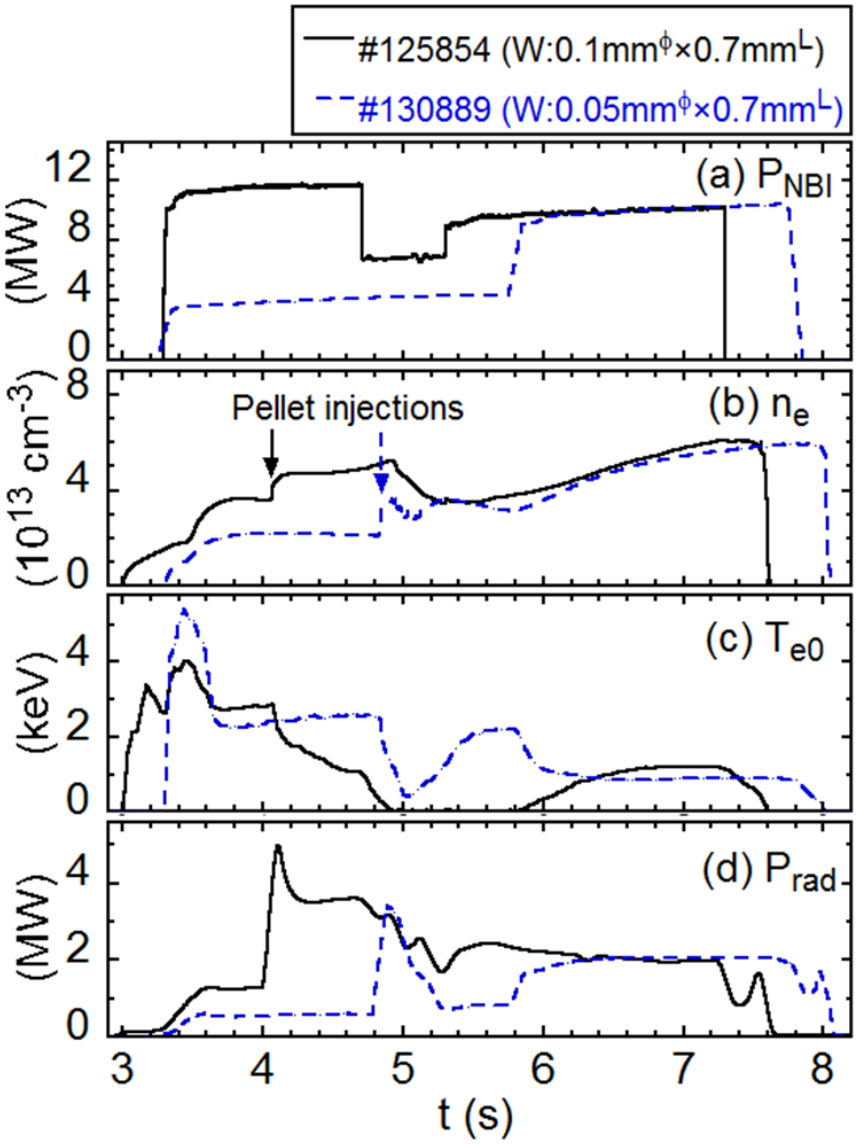

Fig. 4.10 Time behaviors of (a) NBI port-through power, (b) line-averaged electron density, (c) central electron temperature and (d) total radiation power in two discharges with different tungsten pellet sizes; #125854 (solid lines): 0.1 mm$^{\phi}$ × 0.7 mm^{L} injected at t = 4.0 s and #130889 (dashed lines): 0.05 mm$^{\phi}$ × 0.7 mm^{L} injected at t = 4.8 s.

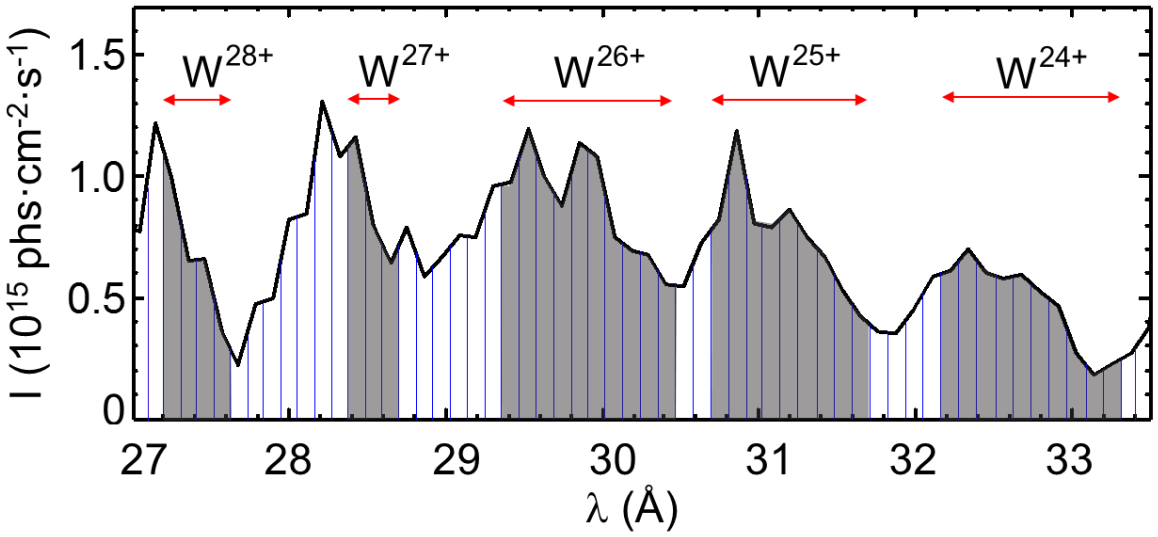

Fig. 4.11 Tungsten spectrum with UTA lines at 27 - 34 Å measured with EUV_Short2 spectrometer. Radial profile of tungsten UTA is analyzed at each wavelength interval indicated with two adjacent vertical lines. The wavelength interval is roughly 0.1 Å and exact values are listed in Table 1. Five wavelength intervals denoted with grey-hatched region are identified as UTA emission in a single ionization stage which is denoted with horizontal arrow.

4.5. Component investigation of UTA spectra based on radial profile measurement

4.5.1 Precise re-evaluation of tungsten UTA lines at 27-34 Å using radial profiles

A series of tungsten injection experiments have been also done for measuring radial profiles of tungsten UTA lines using two space-resolved EUV spectrometers, EUV_Long2 [17] and EUV_Short2 [36], with which full radial profiles at lower and upper half plasma radii are observed at horizontally elongated plasma cross section of elliptical LHD plasmas, respectively. The main aim in the radial profile measurement is to further check the validity in the present evaluation. For the purpose, the tungsten pellet is injected with different sizes in NBI discharges. The discharge waveforms of #125854 (solid lines) and #130889 (dashed lines) are plotted in Fig. 4.10. In #125854 a 0.7 mm^{ϕ} × 0.7 mm^{L} coaxial

graphite pellet with 0.1 mm^{ϕ} × 0.7 mm^{L} tungsten wire is injected at t = 4.0 s, and in #130889 the coaxial graphite pellet with 0.05 mm^{ϕ} × 0.7 mm^{L} tungsten wire is injected at t = 4.8 s. The discharge waveform is entirely affected by the tungsten size and NBI injection power, P_{NBI}. In particular, the electron temperature in the #125854 shot with large tungsten pellet closes to zero after the pellet injection due to a largely increased radiation loss (see Figs. 4.10(c) and (d)). However, the discharge starts to recover from around 1.8 s after the pellet injection, and fully recovers at 2.6 s after the pellet injection at which the temperature is roughly the same as the 130889 shot with a small tungsten pellet. Then, the data analyses in #125854 and #130889 shots are done at t = 4.3 s and 5.3 s, respectively.

In the wavelength range of 15-45 Å the profile data analysis is focused on a limited wavelength range of 27-34 Å where the tungsten UTA line with a single ionization stage has been identified in the previous chapter (see Fig. 4.7). The wavelength spectrum observed with EUV_Short2 is shown in Fig. 4.11. It is noted that the spectral resolution of EUV_Short2 is slightly worse than that of EUV_Short shown in Figs. 4.2 and 4.6, because the CCD of EUV_short2 installed perpendicularly to the wavelength dispersion direction is operated in an image mode with five pixel binning to observe the radial (or vertical) profile in every 100 ms, while the CCD of EUV_Short installed parallel to the wavelength dispersion direction is operated in the full binning mode. The vertical profile is carefully analyzed at the wavelength interval defined by two adjacent vertical solid lines in Fig. 4.11. The ionization stage is thus revaluated for all the wavelength intervals. Here, it is noted that the wavelength interval shown in Fig. 4.11 is roughly 0.1 Å.

A typical example of the radial profile analysis is shown in Fig. 4.12. Three electron temperature profiles are shown in Fig. 4.12(a) as a function of normalized plasma radius, ρ, at different central temperatures of T_{e0} = 2.15 (solid circles), 1.73 (solid triangles) and 1.38 keV (solid diamonds). The chord-integrated profile of W^{24+} UTA line at wavelength interval of 32.28-32.39 Å is also plotted in Fig. 4.12(b) for the three different temperature cases. The abscissa, Z, indicates the vertical position in upper half of LHD plasmas at horizontally elongated plasma cross section. Figure 4.12(c) indicates local emissivity profiles reconstructed from the intensity profiles using Abel inversion method. In the reconstruction, the magnetic surface modified by a plasma pressure effect is accurately calculated by VMEC code. It is clear that the emission line at the wavelength interval of 32.28-32.39 Å consists of a single ionization stage because the peak position shown in Fig. 4.12(c) is outwardly shifted with increase in the electron temperature.

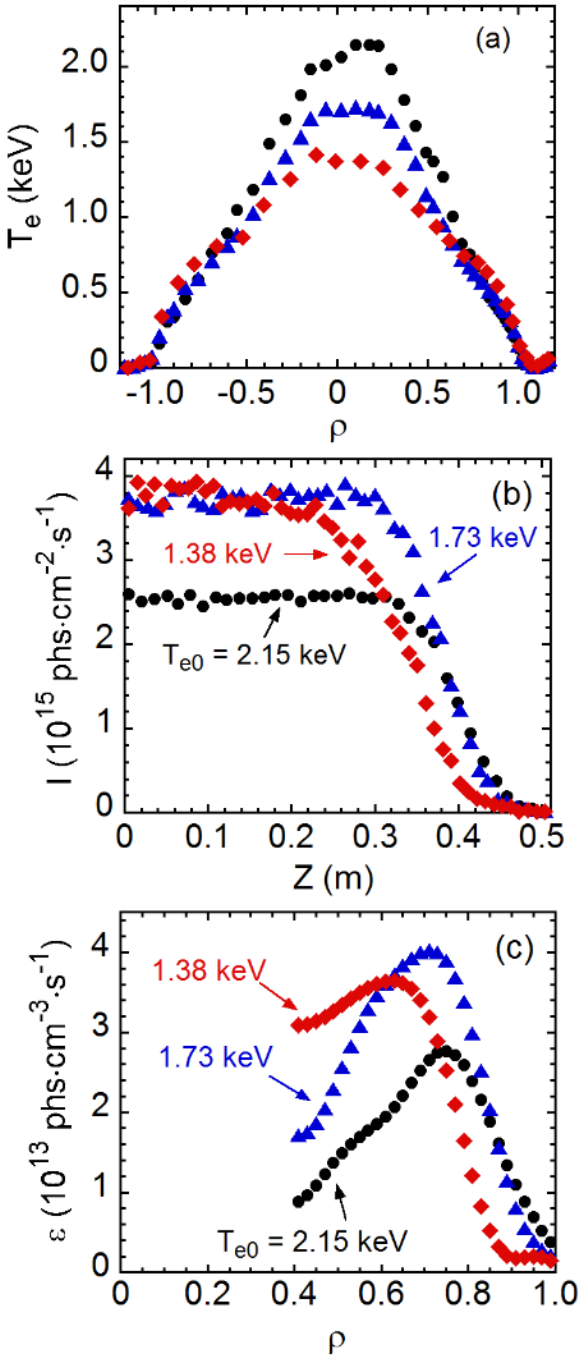

Fig. 4.12 (a) Electron temperature profiles, (b) vertical intensity profiles and (c) local emissivity profiles of tungsten UTA emission line at wavelength interval of 32.28 Å ≤ λ ≤ 32.39 Å (W^{24+}) at three different central electron temperatures of T_{e0} = 1.38 keV (solid diamonds), 1.73 keV (solid triangles) and 2.15 keV (solid circles). The value of ρ means normalized plasma radius of r / <a>, where r is the radial plasma position and <a> is the averaged plasma radius (=64cm).

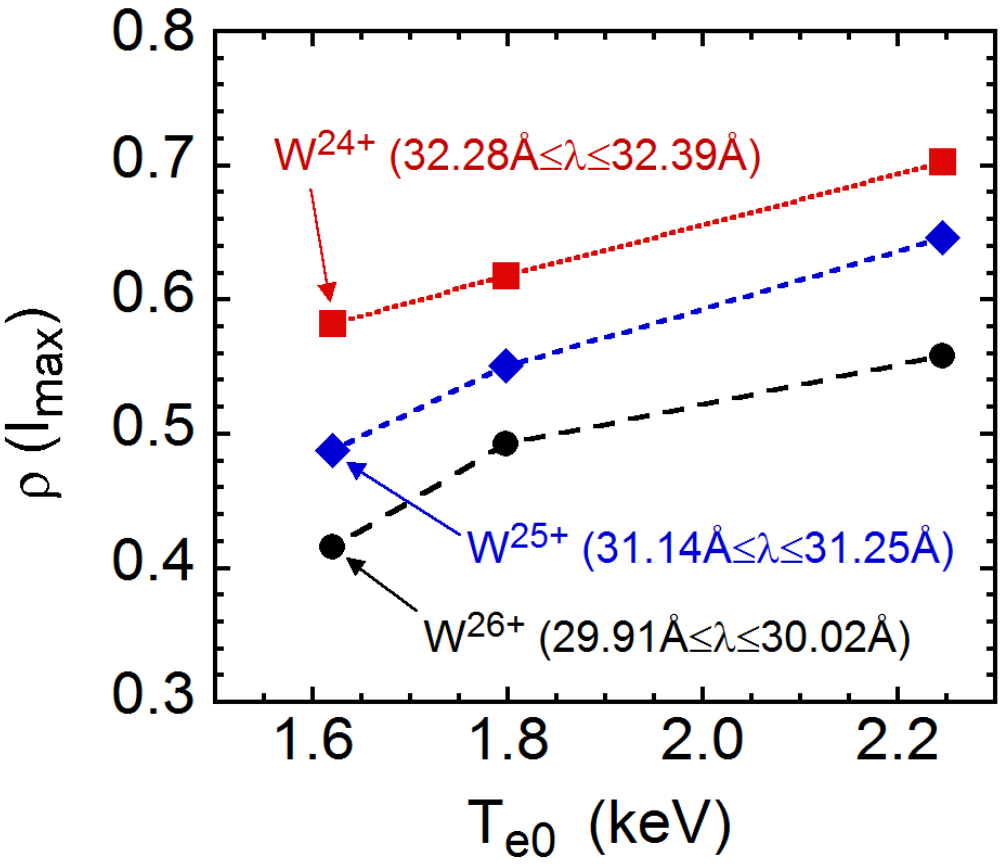

Fig. 4.13 Normalized plasma radius at peak position in vertical intensity profiles of tungsten UTA as a function of central electron temperature, T_{e0}, for three different ionization stages of tungsten ions of W^{24+} (solid squares: 32.28 Å ≤ λ ≤ 32.39 Å), W^{25+} (solid diamonds: 31.14 Å ≤ λ ≤ 31.25 Å) and W^{26+} (solid circles: 29.91 Å ≤ λ ≤ 30.02 Å).

The electron temperature dependence of the peak position can be then analyzed for three different ionization stages of W^{24+}, W^{25+} and W^{26+} at wavelength intervals of 32.28-32.39 Å (solid squares), 31.14-31.25 Å (solid diamonds) and 29.91-30.02 Å (solid circles), respectively, as shown in Fig. 4.13. The vertical axis means normalized plasma radius at the peak intensity in the local emissivity profile, i.e. ρ = 0 at plasma center and ρ = 1 at plasma edge boundary. It is understood from the figure that the tungsten ions reasonably stay at certain plasma radii according to the ionization energy of each ion. That is, the

tungsten ion in lower ionization stages stays in outer plasma region and the ion in higher ionization stages stays in inner plasma region. The result also shows an experimental certification on the validity in the present identification of tungsten UTA lines.

The tungsten UTA line re-examined at 27-34 Å based on the radial profile analysis is summarized in Table 1. The first column is the wavelength interval used for the radial profile analysis. The second column shows a dominant tungsten ionization stage within the wavelength interval denoted in the first column. When the UTA line is blended with line emissions in other ionization stages, blended ionization stages are listed in the third column. The electron temperature at a radial position where the tungsten ion listed in the second column stays is indicated in the fourth column. The electron temperature can be easily obtained from the radial position at the peak intensity in the radial profile of UTA lines, because the electron temperature profile is accurately measured every 30-40 ms with totally 140 radial measurement points in LHD. A typical range in the maximum absolute intensity of UTA lines in the radial profile, I_{max}, is also listed in the fifth column. Ionization energy of the tungsten ion listed in the second column is indicated in the sixth column. When the ionization energy is compared with the electron temperature in the fourth column, we notice that the electron temperature in the fourth column for the tungsten ion in relatively higher ionization stages, e.g. W^{28+}, is a little higher than the ionization energy. On the contrary, the electron temperature for the tungsten ion in lower ionization stages, e.g. W^{24+}, is slightly lower than the ionization energy. This may indicate an effect of the radial transport of tungsten ions [37]. However, even if the difference is due to the transport effect, the present analysis is not affected by the transport. The seventh column as 'status' indicates the availability to diagnostic use for the UTA line at the wavelength interval shown in the first column. If the UTA line consists of several ionization stages, it will not be useful to the diagnostic. The final column shows previous identifications obtained from high-temperature plasmas in tokamaks. The present results are in good agreement with the results from tokamaks, while the uncertainties in wavelengths of the previous results are relatively large.

Thus, we understand that the five wavelength intervals of 27.20-27.62 Å, 28.38-28.70 Å, 29.36-30.47 Å, 30.69-31.71 Å and 32.16-33.32 Å dominantly consist of a single ionization stage of W^{28+}, W^{27+}, W^{26+}, W^{25+} and W^{24+}, respectively. These wavelength ranges are also denoted with shaded area in Fig. 4.11. In particular, the three tungsten ions of W^{24+}, W^{25+} and W^{26+} are expected to be a good choice for the tungsten diagnostic because the shaded wavelength intervals are wide and close to 1 Å. The wide wavelength interval leads to an easy separation in the analysis of the UTA spectrum.

Table 4.1. Component analysis of tungsten UTA at each wavelength interval in 27-34 Å. A main ionization stage is listed in the second column for each wavelength interval. If the wavelength interval includes other ionization stages, those are indicated in the third column as 'blended lines'. Electron temperature at the radial position where the tungsten ion in the main ionization stage exists, maximum intensity at peak position in the radial profile, ionization energy of the main ionization stage are also listed with availability of diagnostic use. Final column shows previous results from tokamak experiments.

λ (Å)	Ionization stage	Blended lines	T_e (keV)	I_{max} (10^{15}phs·cm^{-2}·s^{-1})	Ionization energy (keV)	Status	Previous identifications λ (Å) Tokamaks
27.20-27.30	W^{28+}		1.4±0.2	2.64~3.42	1.132	available	
27.30-27.41	W^{28+}		1.4±0.2	2.30~2.91	1.132	available	
27.41-27.52	W^{28+}		1.4±0.2	2.06~2.72	1.132	available	
27.52-27.62	W^{28+}		1.4±0.2	1.82~2.32	1.132	available	
27.62-27.73	W^{27+}	W^{28+},W^{29+},W^{30+}					
27.73-27.84	W^{27+}	W^{28+},W^{29+},W^{30+}					
27.84-27.95	W^{27+}	W^{28+},W^{29+},W^{30+}					
27.95-28.05	W^{27+}	W^{28+},W^{29+},W^{30+}					
28.05-28.16	W^{27+}	W^{28+},W^{29+},W^{30+}					
28.16-28.27	W^{27+}	W^{28+},W^{29+},W^{30+}					
28.27-28.38	W^{27+}	W^{28+},W^{29+},W^{30+}					
28.38-28.48	W^{27+}		1.2±0.2	3.26~4.90	0.881	available	28.5±0.1 W^{27+} [30]
28.48-28.59	W^{27+}		1.2±0.2	3.01~4.46	0.881	available	
28.59-28.70	W^{27+}		1.2±0.2	2.09~3.09	0.881	available	
28.70-28.81	W^{26+}	W^{27+},W^{28+},W^{29+}					
28.81-28.92	W^{26+}	W^{27+},W^{28+},W^{29+}					
28.92-29.03	W^{26+}	W^{27+},W^{28+},W^{29+}					
29.03-29.14	W^{26+}	W^{27+},W^{28+},W^{29+}					
29.14-29.25	W^{26+}	W^{27+},W^{28+},W^{29+}					
29.25-29.36	W^{26+}	W^{27+},W^{28+},W^{29+}					
29.36-29.47	W^{26+}	W^{27+},W^{28+},W^{29+}					
29.47-29.58	W^{26+}		1.0±0.2	3.48~3.53	0.833	available	
29.58-29.69	W^{26+}		1.0±0.2	3.63~3.65	0.833	available	
29.69-29.80	W^{26+}		1.0±0.2	3.41~3.42	0.833	available	
29.80-29.91	W^{26+}		1.0±0.2	3.41~3.96	0.833	available	
29.91-30.02	W^{26+}		1.0±0.2	3.31~4.31	0.833	available	29.7±0.2 W^{26+} [30]
30.02-30.13	W^{26+}		1.0±0.2	2.97~3.71	0.833	available	
30.13-30.24	W^{26+}		1.0±0.2	2.86~3.64	0.833	available	
30.24-30.35	W^{26+}		1.0±0.2	2.91~3.71	0.833	available	
30.35-30.47	W^{26+}		1.0±0.2	2.74~3.36	0.833	available	
30.47-30.58	W^{26+}	W^{25+}					
30.58-30.69	W^{26+}	W^{25+}					
30.69-30.80	W^{25+}		0.8±0.2	3.38~3.88	0.784	available	
30.80-30.91	W^{25+}		0.8±0.2	4.16~4.63	0.784	available	
30.91-31.03	W^{25+}		0.8±0.2	4.31~4.74	0.784	available	30.94±0.76 W^{25+} [26]
31.03-31.14	W^{25+}		0.8±0.2	3.86~4.22	0.784	available	
31.14-31.25	W^{25+}		0.8±0.2	3.77~4.32	0.784	available	
31.25-31.37	W^{25+}		0.8±0.2	3.57~4.17	0.784	available	31.03±0.01 W^{25+} [27]
31.37-31.48	W^{25+}		0.8±0.2	3.31~3.82	0.784	available	
31.48-31.59	W^{25+}		0.8±0.2	3.20~3.58	0.784	available	
31.59-31.71	W^{25+}		0.8±0.2	3.22	0.784	available	
31.71-31.82	W^{25+}	W^{24+}					
31.82-31.94	W^{25+}	W^{24+}					
31.94-32.05	W^{25+}	W^{24+}					
32.05-32.16	W^{25+}	W^{24+}					
32.16-32.28	W^{24+}		0.6±0.2	3.38~4.18	0.734	available	
32.28-32.39	W^{24+}		0.6±0.2	3.64~4.53	0.734	available	
32.39-32.51	W^{24+}		0.6±0.2	3.50~4.62	0.734	available	
32.51-32.63	W^{24+}		0.6±0.2	3.17~4.60	0.734	available	32.43±0.94 W^{24+} [26]
32.63-32.74	W^{24+}		0.6±0.2	3.02~4.33	0.734	available	
32.74-32.86	W^{24+}		0.6±0.2	3.13~4.27	0.734	available	
32.86-32.97	W^{24+}		0.6±0.2	2.90~3.93	0.734	available	32.63±0.02 W^{24+} [27]
32.97-33.09	W^{24+}		0.6±0.2	2.84~3.58	0.734	available	
33.09-33.20	W^{24+}		0.6±0.2	3.31	0.734	available	
33.20-33.32	W^{24+}		0.6±0.2	3.16	0.734	available	

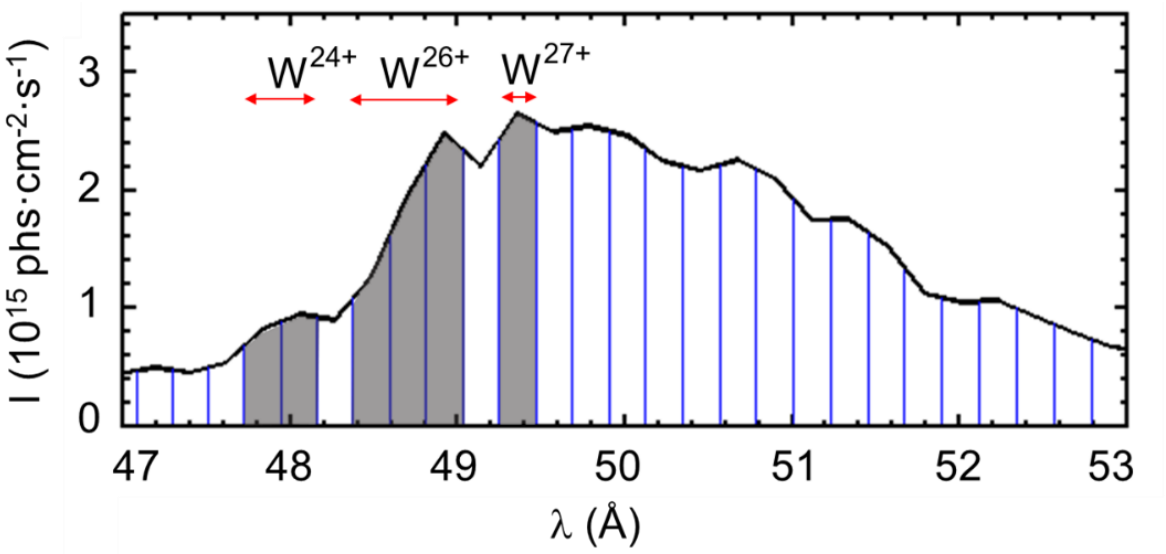

Fig. 4.14 Tungsten spectrum with UTA lines at 47 - 53 Å measured with EUV_Long2 spectrometer. Radial profile of tungsten UTA is analyzed at each wavelength interval indicated with two adjacent vertical lines. The wavelength interval is roughly 0.2 Å and exact values are listed in Table 2. Three wavelength intervals denoted with grey-hatched region are identified as UTA emission in a single ionization stage which is denoted with horizontal arrow.

4.5.2 Precise re-evaluation of tungsten UTA lines at 47-53 Å using radial profiles

The tungsten UTA wavelength spectrum at 47-53 Å is reformed from profile data taken with EUV_Long2 in the #130889 NBI discharge (see Fig. 4.10). The result is shown in Fig. 4.14. The radial profile from EUV_Long2 observed at the lower-half LHD plasma is carefully analyzed for the UTA line re-evaluation. The analysis is done at the wavelength interval defined by two adjacent solid lines as well as the former section.

A typical example on the radial profile analysis at the wavelength interval of 48.81-49.03 Å is shown in Fig. 4.15. The radial profiles of electron temperature, observed intensity and local emissivity are shown for the W^{24+} UTA line in Figs. 4.15(a), (b) and (c), respectively. The figures are plotted at three different central electron temperatures of T_{e0} = 1.30 (solid diamonds), 1.37 (solid triangles) and 1.86 keV (solid circles). In Fig. 4.15(b)

the horizontal axis shows the vertical distance from the plasma center with minus values, since the vertical profile is measured at lower half of the LHD plasma with EUV_Long2. That is, the minus values indicate the distance from the midplane at Z = 0 to plasma bottom. The local emissivity profile in Fig. 4.15(c) is obtained by the same way as Fig. 4.12(c). The peak position in the W^{24+} emissivity profile outwardly moves toward the plasma edge as the central electron temperature increases. This movement against the electron temperature exhibits the same tendency as the result in Fig. 4.13.

The result is summarized in Table 2. Meanings of each column are the same as Table 1. The final column indicates previous identifications in tokamaks and compact electron beam ion trap (CoBITs). Evaluations of the ionization stage at 47.72-48.15Å and 48.37-49.03Å are clearly different between the present and previous results, while the evaluation at 49.24-49.46Å in the present result shows a good agreement with the previous ones. The present result shows two wavelength intervals of 47.72-48.15Å and 48.37-49.03Å correspond to W^{24+} and W^{26+} ions, respectively, while the previous results show two wavelength intervals of 47.94±0.05Å and 48.93±0.05Å (or 48.91±0.01Å) correspond to W^{27+} and W^{28+} ions, respectively. In order to examine the different evaluation at the two wavelength ranges, radial profiles are carefully analyzed in next section.

In contrast to the wavelength range of 27-34 Å listed in Table 1, the wavelength interval consisting of a single ionization stage is very limited in the wavelength range of 47-53 Å. Only three narrow wavelength intervals of 47.72-48.15 Å, 48.37-49.03 Å and 49.24-49.46 Å consist of a single ionization stage of tungsten ions. All other wavelength intervals are blended with UTA lines from other ionization stages. Therefore, the spectroscopic diagnostics of W^{24+}-W^{27+} ions in the short wavelength range of 27-34 Å listed in Table 1 seems to be easier compared to the long wavelength range of 47-53 Å.

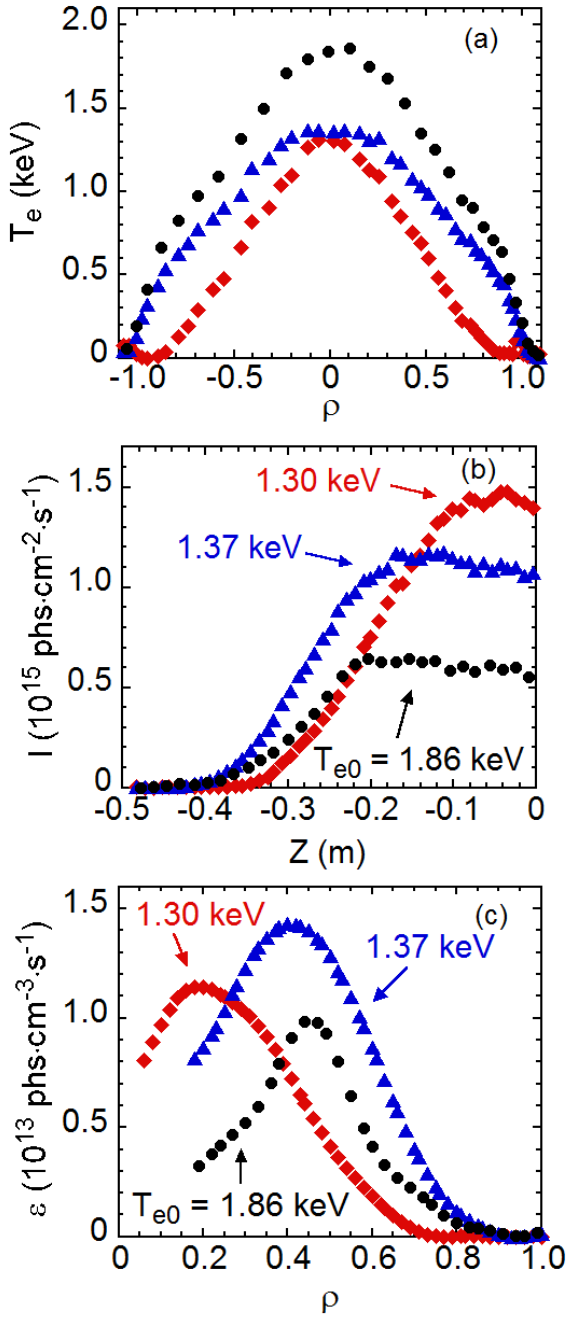

Fig. 4.15 (a) Electron temperature profiles, (b) vertical intensity profiles and (c) local emissivity profiles of tungsten UTA emission line at wavelength interval of 48.81 Å ≤ λ ≤ 49.03 Å (W^{24+}) at three different central electron temperatures of T_{e0} = 1.30 (solid diamonds), 1.37 (solid triangles) and 1.86 keV (solid circles). Meaning of ρ is the same as Fig. 4.12.

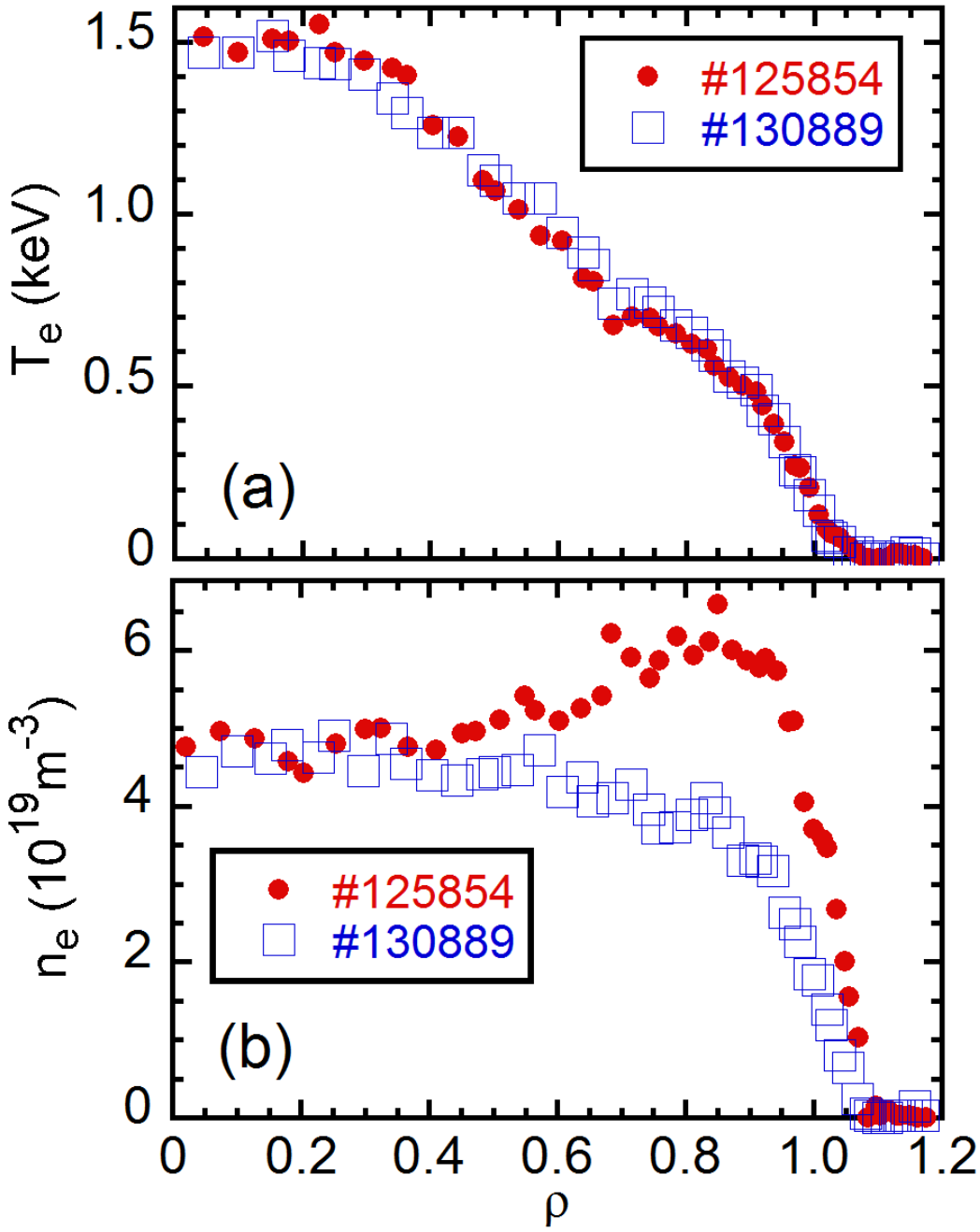

Fig. 4.16 (a) Electron temperature and (b) density profiles in #125854 at t = 4.3 s (solid circles) and # 130889 at t = 5.3 s (open squares).

Table 4.2. Component analysis of tungsten UTA at each wavelength interval in 47-53 Å. A main ionization stage is listed in the second column for each wavelength interval. If the wavelength interval includes other ionization stages, those are indicated in the third column as 'blended lines'. Electron temperature at the radial position where the tungsten ion in the main ionization stage exists, maximum intensity at peak position in the radial profile, ionization energy of the main ionization stage are also listed with availability of diagnostic use. Final column shows previous results from tokamak and CoBIT experiments.

λ (Å)	Ionization stage	blended lines	T_e (keV)	I_{max} (10^{15}phs·cm^{-2}·s^{-1})	Ionization energy (keV)	status	Previous identifications λ (Å)	
							Tokamaks	CoBITs
47.72-47.94	W^{24+}		0.6±0.2	0.37~0.55	0.734	available	47.94±0.05 W^{27+} [33]	
47.94-48.15	W^{24+}		0.6±0.2	0.40~0.62	0.734	available		
48.15-48.37	W^{24+}	W^{26+}						
48.37-48.59	W^{26+}		1.0±0.2	0.62	0.833	available	48.93±0.05 W^{28+} [33]	48.91±0.01 W^{28+} [34]
48.59-48.81	W^{26+}		1.0±0.2	0.95	0.833	available		
48.81-49.03	W^{26+}		1.0±0.2	1.13	0.833	available		
49.03-49.24	W^{26+}	W^{27+}						
49.24-49.46	W^{27+}		1.2±0.2	1.21	0.881	available	49.37±0.05 W^{27+} [33]	48.4±0.01 W^{27+} [34]
49.46-49.68	W^{24+}	W^{27+},W^{29+}						
49.68-49.90	W^{24+}	W^{27+},W^{29+}						
49.90-50.12	W^{24+}	W^{27+},W^{29+}						
50.12-50.34	W^{24+}	W^{27+},W^{29+}						
50.34-50.56	W^{27+}	W^{24+},W^{32+},W^{33+}						
50.56-50.79	W^{27+}	W^{24+},W^{32+},W^{33+}						
50.79-51.01	W^{27+}	W^{24+},W^{32+},W^{33+}						
51.01-51.23	W^{27+}	W^{24+},W^{32+},W^{33+}						
51.23-51.45	W^{27+}	W^{28+},W^{32+},W^{33+}						
51.45-51.67	W^{27+}	W^{28+},W^{32+},W^{33+}						
51.67-51.90	W^{27+}	W^{28+},W^{32+},W^{33+}						
51.90-52.12	W^{24+}	W^{31+},W^{32+}						
52.12-52.35	W^{24+}	W^{31+},W^{32+}						
52.35-52.57	W^{24+}	W^{31+},W^{32+}						
52.57-52.79	W^{24+}	W^{31+},W^{32+}						

4.5.3 Comparison of radial profiles of UTA lines between two different wavelength ranges of 27-34 Å and 47-53 Å

In order to carefully examine the evaluated ionization stage of UTA lines, the radial intensity profile of UTA lines at 27-34 Å wavelength range observed with EUV_Short2 are compared with that at 47-53 Å observed with EUV_Long2. Two discharges with identical electron temperature profiles are chosen for the comparison. The electron temperature profiles in #125854 (solid circles) and #130889 (open squares) shots are plotted in Fig.

4.16(a). It is clear that the two profiles show an entirely identical distribution in the electron temperature. Although the electron density profiles of the two discharges, plotted in Fig. 4.16(b), show a clear difference in the outer plasma region, it does not give any serious effect on the following comparison because the tungsten UTA line emissions are located in the central region of plasmas in such low temperature discharges.

At first, the radial chord-integrated intensity profile of W^{27+} UTA line is compared between two different wavelength intervals of 28.38-28.48 Å and 49.24-49.46 Å. The result is shown in Fig. 4.17(a). The vertical profiles at 27-34 Å from EUV_Short2 and 47-53 Å from EUV_Long2 are measured at different vertical positions of upper and lower half plasmas, respectively. In order to examine the apparent difference, the lower-half profile is superimposed on the upper-half profile. Differences in the length of observation chords passing through the LHD plasma and the vertical angle between EUV_Short2 and EUV_Long2 spectrometer systems are negligibly small along Z direction [38]. Thus, it is found both profiles are entirely identical. Similar comparison is also made for the W^{26+} and W^{24+} UTA lines. In Fig. 4.17(b) the W^{26+} UTA line at the wavelength interval of 29.80-29.91 Å is compared with that at 48.81-49.03 Å and in Fig. 4.17(c) the W^{24+} UTA line at the wavelength interval of 32.28-32.39 Å is compared with that at 47.94-48.15 Å. These two vertical profiles for W^{26+} and W^{24+} ions also show an entire overlapping between two different wavelength intervals. These results clearly indicate that the present evaluation of the tungsten UTA lines is correct.

The UTA lines at 28.38-28.48 Å and 49.24-49.46 Å were identified as a single ionization stage of W^{27+} ions in the previous works [17, 30, 33]. The present result in Fig. 4.17(a) shows a good agreement with the previous works. The UTA line at 29.80-29.91 Å in Fig. 4.17(b) was identified as W^{26+} in the previous works [17, 30] and the UTA emission line at 48.81-49.03 Å was identified as W^{28+} [4, 33]. Since the vertical profiles of both emission lines are identical as shown in Fig. 4.17(b), it is confirmed through the present work that the UTA lines at 29.80-29.91 Å and 48.81-49.03 Å have the same ionization stage of W^{26+} ions. The UTA line at 47.94-48.15 Å was identified as a single ionization stage from W^{27+} ions in the previous work [33], while the UTA emission line at 32.28-32.39 Å was identified as W^{24+} in the previous works [17, 26, 27]. In the present work, it is also found that both the UTA lines at 32.28-32.39 Å and 47.94-48.15 Å shown in Fig. 4.17(c) have the same ionization stage of W^{24+} ions.

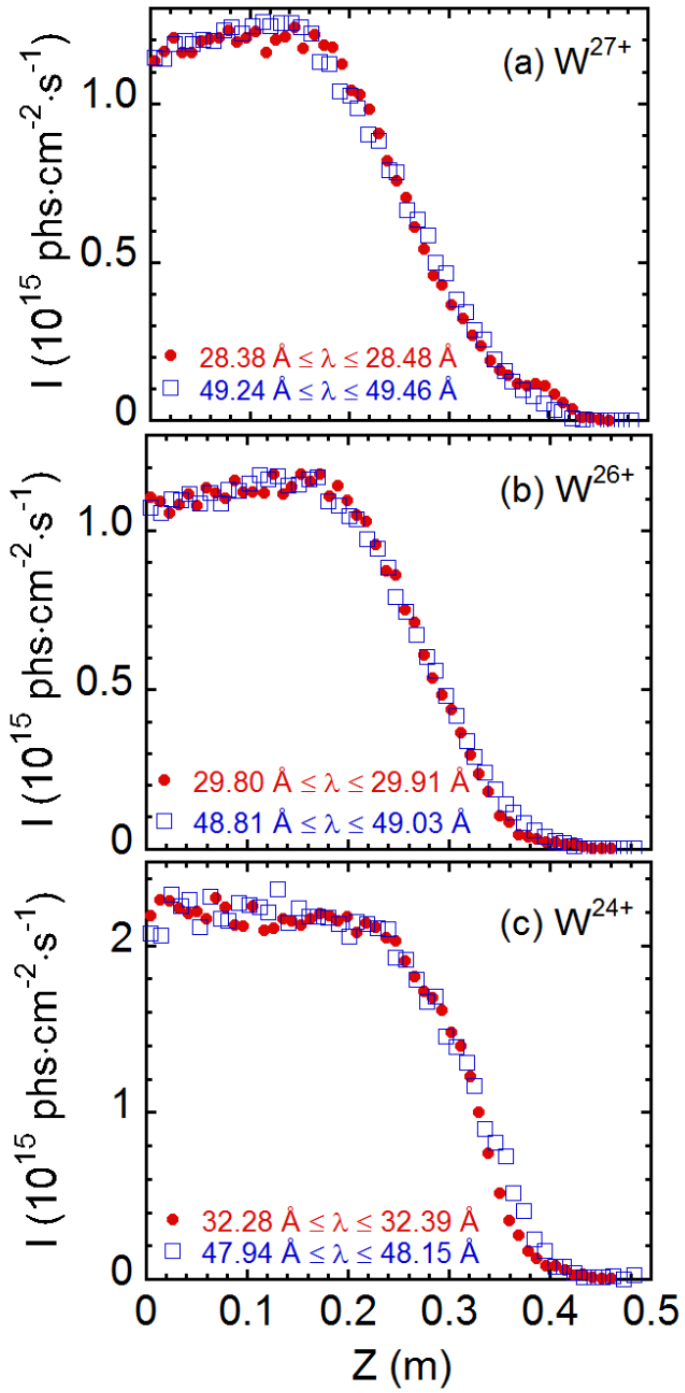

Fig. 4.17 Vertical intensity profiles of (a) W^{27+} emissions at 28.38 Å ≤ λ ≤ 28.48 Å (solid circles) and 49.24 Å ≤ λ ≤ 49.46 Å (open squares), (b) W^{26+} emissions at 29.80 Å ≤ λ ≤ 29.91 Å (solid circles) and 48.81 Å ≤ λ ≤ 49.03 Å (open squares) and (c) W^{24+} emissions at 32.28 Å ≤ λ ≤ 32.39 Å (solid circles) and 47.94 Å ≤ λ ≤ 48.15 Å (open squares).

4.6. Summary

A series of experiments on the study of tungsten spectra have been carried out in LHD with tungsten pellet injection to investigate a wavelength interval in the tungsten UTA spectrum applicable to the diagnostic use. For the tungsten spectral analysis, accurate wavelength positions in the tungsten UTA spectrum measured by EUV_Short spectrometer are carefully determined based on the diffraction grating principle equation and cubic polynomial fitting. Ten well-known emission lines are used for the cubic polynomial fitting. The maximum deviation between experimentally determined wavelengths, λ_{exp}, and theoretically calculated wavelengths, λ_{cal}, is roughly 0.025 Å. Two UTA groups are observed in the tungsten spectrum at 15-70 Å. UTA group at 15-45 Å consists of four transitions of 6g-4f, 5g-4f, 5f-4d and 5g-4f, and the other UTA group at 45-70 Å consists of three transitions of 4f-4d, 4d-4p and 5d-4f. The tungsten UTA is then analyzed for each group.

At first, the UTA line intensity is examined at every narrow wavelength interval, which corresponds to the size of a single CCD pixel, as a function of central electron temperature during the temperature recovery phase after the pellet injection. It is found that several wavelength intervals have a single intensity peak at a certain electron temperature. As a result, it is evaluated that the UTA lines at wavelength intervals of 27.18-27.24 Å, 28.46-28.53 Å, 29.89-29.95 Å, 31.17-31.23 Å, 32.31-32.37 Å, 47.88-47.96 Å, 48.85-48.92 Å and 49.27-49.34 Å consist of a single ionization stage of tungsten ions.

Next, the radial profiles measured with two space-resolved EUV spectrometers are also analyzed at every narrow wavelength interval for further spectral evaluation. For the purpose, the ionization stage of tungsten ions is revaluated with the local emissivity profile reconstructed from the chord-integrated intensity profile. The results on the spectral and profile analyses of UTA lines are summarized in two tables for all wavelength intervals at 27-34 Å and 47-53 Å. The wavelength intervals composing of a single ionization stage of tungsten ions are selected for the diagnostic application.

The radial location of UTA lines is also studied against the electron temperature. It is certificated that the radial location outwardly moves with the electron temperature. The radial intensity profile of UTA lines is compared between two different wavelength intervals. As a result, it is found that the radial profiles at two different wavelength intervals in the UTA spectra are entirely overlapped when the two wavelength intervals consist of the same ionization stage of tungsten ions. These results experimentally certify the validity in the present evaluation on the ionization stage of UTA lines. Three sets of

wavelength intervals, i.e. 28.38-28.48 Å and 49.24-49.46 Å, 29.80-29.91 Å and 48.81-49.03 Å, 32.28-32.39 Å and 47.94-48.15 Å, are newly evaluated as W^{27+}, W^{26+} and W^{24+} with high accuracy, respectively. The present evaluation on the ionization stage of tungsten UTA lines is applicable to the tungsten diagnostic in high-temperature plasmas.

References

[1] G.F. Matthews et al., Phys. Scr. T128, 137 (2007).
[2] R.A. Pitts et al., Phys. Scr. T138, 014001 (2009).
[3] R. Neu et al., Fusion Eng. Des. 65, 367 (2003).
[4] K. Asmussen et al., Nucl. Fusion 38, 967 (1998).
[5] J. Clementson et al., Phys. Scr. 81, 015301 (2010).
[6] J. Yanagibayashi et al., J. Phys. B: At. Mol. Opt. Phys. 43, 144013 (2010).
[7] H. Zhang et al., Jpn. J. Appl. Phys. 54, 086101 (2015).
[8] H.A. Sakaue et al., J. Phys.: Conf. Ser. 163, 012020 (2009).
[9] K. Mori et al., At. Data Nucl. Data Tables 23, 195-294 (1979).
[10] S. Morita et al., Nucl. Fusion 53, 093017 (2013).
[11] A. Kramida et al., NIST Atomic Spectra Database (ver. 5.2) [Online] Available: http://physics.nist.gov/asd [3 September 2017] (2014).
[12] E.J. Doyle et al., Nucl. Fusion 47, S18 (2007).
[13] ITER Physics Expert Group on Divertor, Nucl. Fusion 39, 2391 (1999).
[14] J.W. Coenen et al., J. Nucl. Mater. 463, 78-84 (2015).
[15] A. Geier et al., Plasma Phys. Control. Fusion 44, 2091-2100 (2002).
[16] A. Thoma et al., Plasma Phys. Control. Fusion 39, 1487-1499 (1997).
[17] S. Morita et al., AIP Conf. Proc. 1545, 143-152 (2013).
[18] T. Nakano and the JT-60 Team, J. Nucl. Mater. 415, S327 (2011).
[19] R. Dux et al., J. Nucl. Mater. 390-391, 858-863 (2009).
[20] G.J. Van Rooij et al., J. Nucl. Mater. 438, S42-S47 (2013).
[21] V. Bobkov et al., J. Nucl. Mater. 438, S160-S165 (2013).
[22] T. Oishi et al., Phys. Scr. 91, 025602 (2016).
[23] T. Pütterich et al., Plasma Phys. Control. Fusion 50, 085016 (2008).
[24] T. Pütterich et al., J. Phys. B: At. Mol. Opt. Phys. 38, 3071-3082 (2005).
[25] R. Radtke and C. Biedermann, Phys. Rev. A 64, 012720 (2001).
[26] M. Finkenthal et al., Phys. Lett. A 127, 255 (1988).

[27] Y.A. Podpaly et al., Can. J. Phys. 89, 591 (2011).
[28] M.B. Chowdhuri et al., Plasma Fusion Res. 2, S1060 (2007).
[29] C.S. Harte et al., J. Phys. B: At. Mol. Opt. Phys. 45, 205002 (2012).
[30] C.S. Harte et al., J. Phys. B: At. Mol. Opt. Phys. 43, 205004 (2010).
[31] C.Suzuki et al., J. Phys. B: At. Mol. Opt. Phys. 44, 175004 (2011).
[32] J. Sugar and V. Kaufman, Phys. Rev. A 21, 2096 (1980).
[33] R.C. Isler et al., Phys. Lett. 63A, 295-297 (1977).
[34] H.A. Sakaue et al., Phys. Rev. A 92, 012504 (2015).
[35] I. Murakami et al., Nucl. Fusion 55, 093016 (2015).
[36] X.L. Huang et al., Rev. Sci. Instrum. 85, 11E818 (2014).
[37] C.F. Dong et al., Plasma Sci. Tech. 13, 140 (2011).
[38] Y. Liu et al., Rev. Sci. Instrum. 87, 11E308 (2016).

Chapter 5

Density evaluation of tungsten W^{24+}, W^{25+} and W^{26+} ions using unresolved transition array at 27-34 Å

5.1. Introduction

Since the edge electron temperature of ITER plasmas is estimated to range in $0.2 \leq T_e \leq 4$ keV [1, 2], pseudo-continuum tungsten spectra from unresolved transition array (UTA) emitted at extreme ultraviolet (EUV) wavelength ranges of 18-33 Å and 44-64 Å are very important for studying the edge tungsten behavior in ITER. In LHD, then, the tungsten UTA spectrum has been extensively investigated by injecting a coaxial graphite pellet included a thin tungsten wire [3], which can easily penetrate a thick stochastic magnetic field layer [4] having the capability of enhancing the impurity screening in the plasma edge [5]. A spectral structure of the UTA has been studied by analyzing an electron temperature dependence of the UTA line intensity at each wavelength interval and measuring the peak position of radial profiles of the UTA line. In a previous result, it has been found that the tungsten UTA line at wavelength intervals of 32.16-33.32 Å, 30.69-31.71 Å and 29.47-30.47 Å is composed of a single ionization stage of W^{24+}, W^{25+} and W^{26+}, respectively [6].

In the present study, the tungsten ion density is evaluated as the first attempt based on the previous study on the tungsten UTA line. At first, a vertical intensity profile of the UTA line is measured with a space-resolved EUV spectrometer in LHD for the W^{24+}, W^{25+} and W^{26+} ions at wavelength intervals mentioned above. A local emissivity profile is reconstructed from the intensity profile using Abel inversion method. Next, a photon emission coefficient is calculated with a collisional-radiative (CR) model developed for the UTA spectrum analysis in which two effects of inner-shell excitation and configuration interaction are newly considered [7]. The tungsten ion density can be thus evaluated from the local emissivity profile and photon emission coefficient in addition to the electron temperature and density profiles measured with high accuracy. A total tungsten density is also estimated from the analyzed W^{24+} ion density profile in the vicinity of $\rho = 0.7$ based on the fractional abundance in ionization equilibrium calculated with ADAS code [8].

5.2. Experimental results

5.2.1 Typical discharge with tungsten pellet injection

A series of experiments with tungsten pellet injection have been carried out in LHD for tungsten spectroscopy. A typical discharge with a coaxial tungsten pellet (tungsten wire: 0.05 mm in diameter × 1.0 mm in length, graphite cylinder: 0.7 mm in diameter × 0.7 mm in length) injected at horizontal mid-plane is shown in Fig. 5.1. The discharge is sufficiently maintained by three negative-ion-source-based neutral beams (n-NBI#1, #2 and #3) with energy of 180 keV during 3.6-6.2 s. A tungsten pellet with a relatively large amount of tungsten is injected at t = 4.3 s. The line-averaged electron density, n_e, gradually increases from 3.0×10^{13} cm^{-3} to 5.2×10^{13} cm^{-3} during the whole n-NBI phase after a quick increase at the pellet injection. The number of particles injected by the pellet is $N_C = 2.7 \times 10^{19}$ for carbon and $N_W = 1.2 \times 10^{17}$ for tungsten. If the carbon and tungsten ions are uniformly distributed in the whole LHD plasma volume of 30 m^3, we obtain a local density of $n_C = 8.9 \times 10^{11}$ cm^{-3} for carbon and $n_W = 4.1 \times 10^9$ cm^{-3} for tungsten. The small density rise at t = 4.3 s just after the pellet injection is mainly brought by the carbon. However, the continuous density increase appearing from t = 4.3 s to t = 6.3 s originates in a reduction of the edge particle screening due to the edge temperature reduction because the density increase brought by the tungsten ionization is negligibly small. The central electron temperature, T_{e0}, after the pellet injection gradually decreases reflecting increases in the

total radiation power, P_{rad}, and the electron density. The UTA line intensity from W^{24+} (32.16-33.32 Å), W^{25+} (30.69-31.71 Å) and W^{26+} (29.36 -30.47 Å) ions are plotted in Figs. 5.1(f), 5.1(g) and 5.1(h), respectively. It is noticed that the UTA line from W^{24+}, W^{25+} and W^{26+} ions reach the peak intensity in sequence, since the electron temperature continuously decreases.

The electron temperature and density profiles during t = 4.2-6.2 s are shown in Figs. 5.2(a) and 5.2(b), respectively. The horizontal axis means a normalized plasma radius, i.e. $\rho = 0$ at plasma center and $\rho = 1.0$ at LCFS (last closed flux surface). A steep electron temperature profile at t = 4.2 s before the pellet injection gradually changes to a flatter profile after the pellet injection due to the enhanced radiation loss. On the contrary, the electron density profile does not change so much before and after the pellet injection, while the density itself continuously increases during the n-NBI phase.

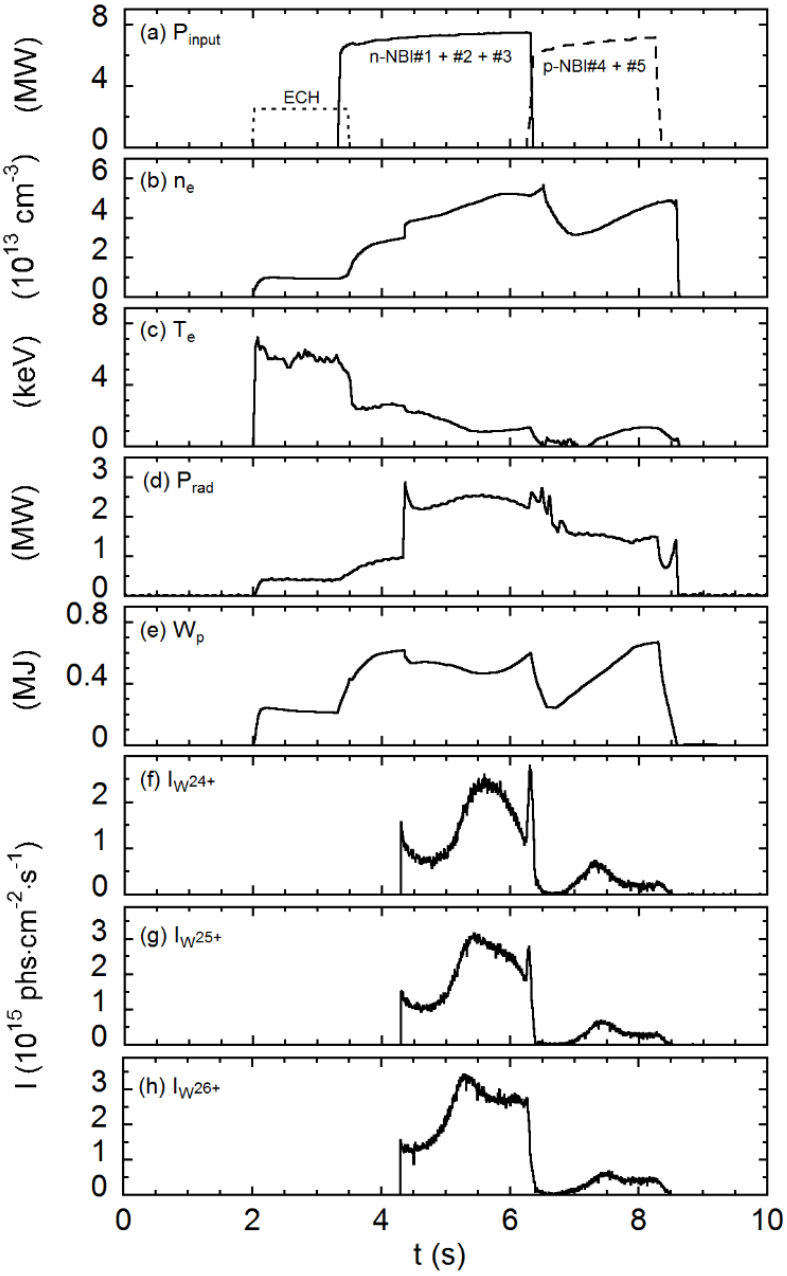

Fig. 5.1 Discharge waveform with tungsten pellet injected at 4.3 s; (a) NBI input power, (b) line-averaged electron density, (c) central electron temperature, (d) total radiation power, (e) plasma stored energy, (f) emission intensity from W^{24+} ions at wavelength interval of 32.18-33.34 Å, (g) intensity of W^{25+} emission line at wavelength interval of 30.69-31.71 Å, and (h) intensity of W^{26+} emission line at wavelength interval of 29.36-30.47 Å. A coaxial graphite pellet (0.7 mm^{ϕ} × 0.7 mm^{L}) with a tungsten wire size of 0.05 mm^{ϕ} × 1.0 mm^{L} is injected at t = 4.3 s.

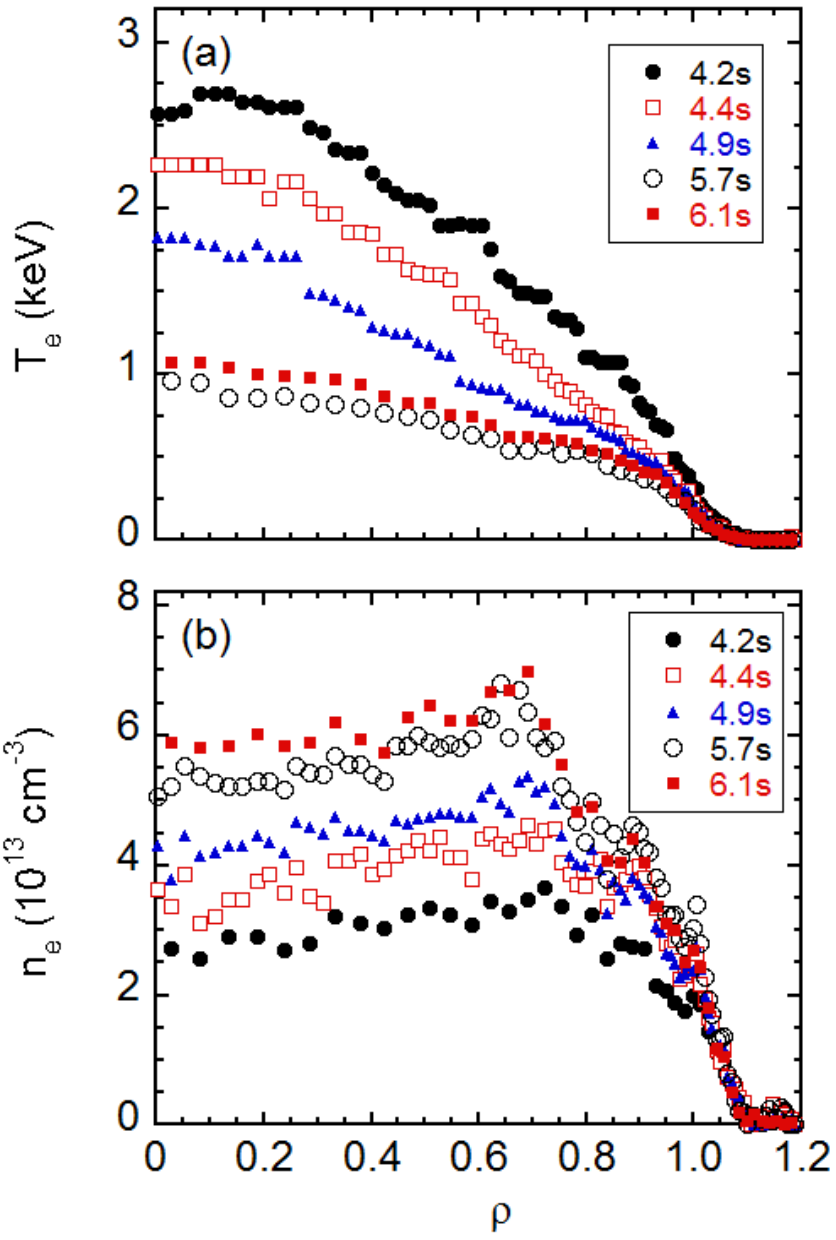

Fig. 5.2 (a) Electron temperature and (b) density profiles at t = 4.2 (just before pellet injection), 4.4 (just after pellet injection), 4.9, 5.7 and 6.1 s.

The tungsten spectrum in the wavelength range of 18-36 Å is measured with EUV_Short spectrometer at Δt = 0.9 s after the pellet injection, as shown in Fig. 5.3. The ionization stage of UTA lines in each peak group is estimated by referring the previous work from CoBIT [9] and plasma device [10]. As shown in the figure, the tungsten UTA spectrum is composed of many ionization stages of tungsten ions, e.g. from W^{24+} to W^{33+} in the present spectrum. These UTA lines are basically formed by four transitions of 6g-4f, 5g-4f, 5f-4d and 5g-4f. In our previous work [6], the UTA line at wavelength intervals of 27.20-27.62 Å, 28.38-28.70 Å, 29.36-30.47 Å, 30.69-31.71 Å and 32.16-33.32 Å indicated with hatched regions is found to be composed of a single ionization stage of W^{28+}, W^{27+}, W^{26+}, W^{25+} and W^{24+}, respectively. In the present study three UTA lines at 29.36-30.47 Å, 30.69-31.71 Å and 32.16-33.32 Å are used to evaluate the tungsten density of W^{26+}, W^{25+} and W^{24+} ions, respectively, since such wavelength intervals are relatively wider, resulting in higher reliability of the UTA line identification and larger signal to noise ratio.

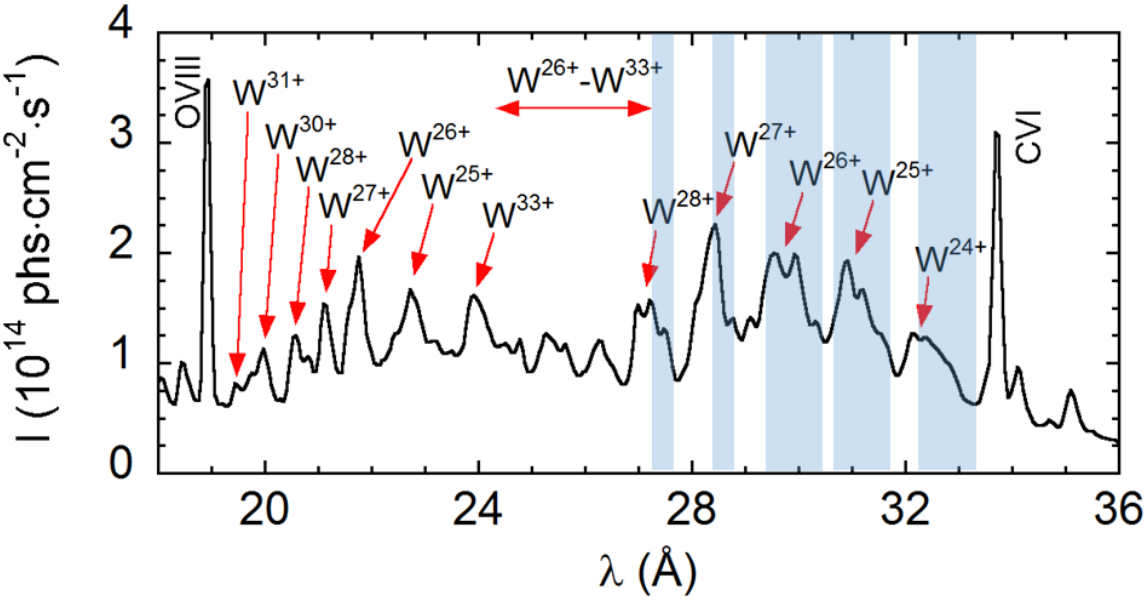

Fig. 5.3 Tungsten UTA spectrum at wavelength range of 18-36 Å measured by EUV_Short. Shaded area indicates a wavelength interval in which UTA emission lines are composed of a single ionization stage.

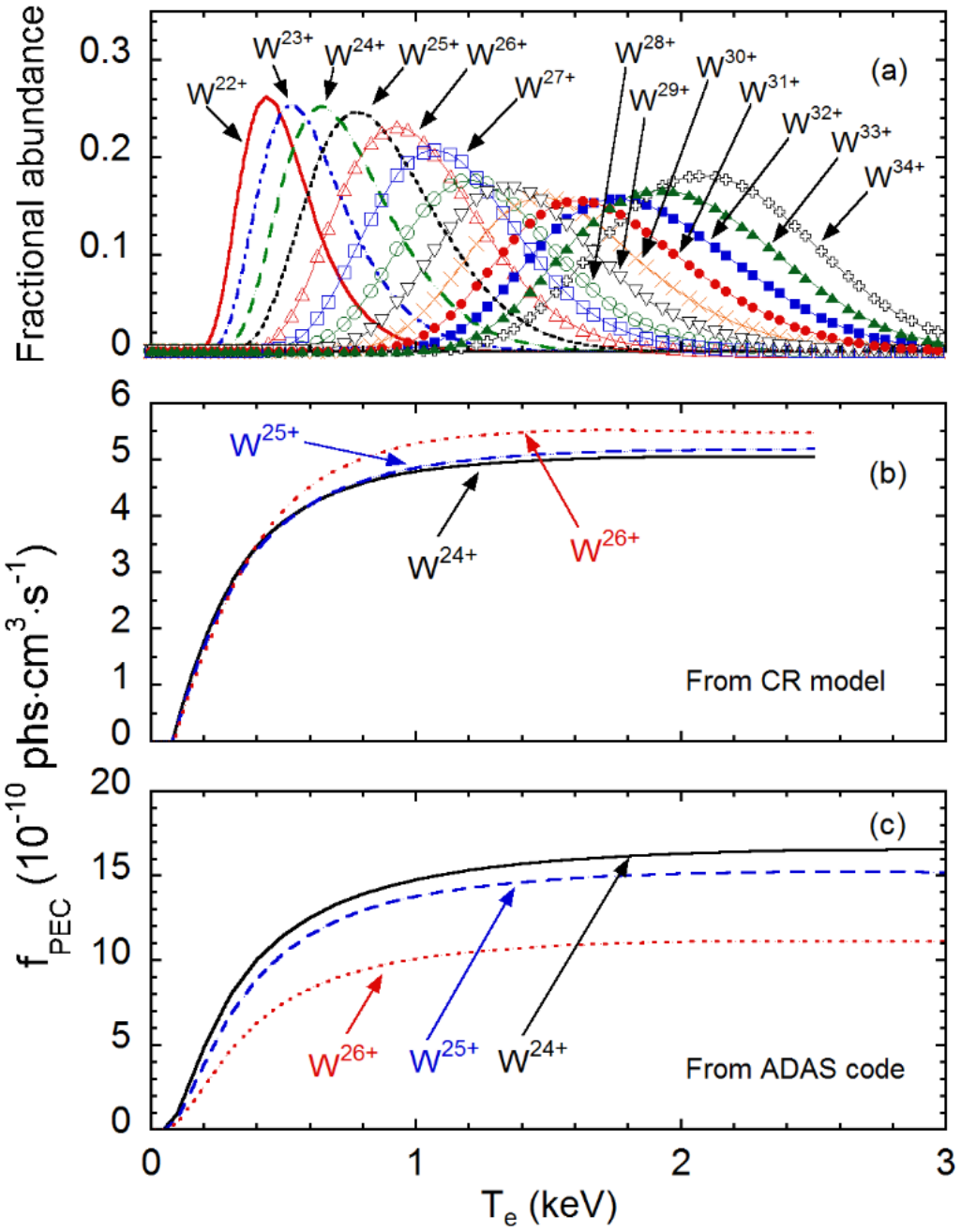

Fig. 5.4 (a) Fractional abundance of W^{22+}-W^{34+} calculated with ADAS code at $n_e = 4 \times 10^{13}$ cm^{-3}, and total photon emission coefficient of W^{24+} (32.16-33.32 Å: solid line), W^{25+} (30.69-31.71 Å: dashed line) and W^{26+} (29.47-30.47 : dotted line) calculated with (b) the present CR model and (c) ADAS code.

5.2.2 Calculation of photon emission coefficients

The fractional abundance of W^{22+}-W^{34+} ions in ionization equilibrium is calculated at $n_e = 4 \times 10^{13}$ cm^{-3} using ADAS code, as shown in Fig. 5.4(a). Since the ionization energy of tungsten ion becomes large with the ionization stage, the electron temperature range where a certain tungsten ion exists also becomes wide with the ionization stage. Three sequential tungsten ions of the W^{24+}, W^{25+} and W^{26+} having a relatively narrow electron temperature window take the maximum abundance at similar temperatures of 0.64, 0.77 and 0.93 keV, respectively. In the toroidal plasma, then, the radial position where the three tungsten ions exist is close to each other, when the electron temperature is sufficiently high (see Fig. 5.2(a)).

Total photon emission coefficients of W^{24+}, W^{25+} and W^{26+} at wavelength intervals of 32.16-33.32, 30.69-31.71 and 29.47-30.47 Å are calculated with CR model developed for analysis of the tungsten UTA spectrum [7]. In the CR model, principal quantum number up to n = 7 and 11753, 13772 and 7515 J-resolved fine-structure levels are taken into account for W^{24+}, W^{25+} and W^{26+} ions, respectively, and 19-27 electron configurations are considered for one ion. Effects of inner-shell excitation and configuration interaction are also considered in addition to general atomic processes. The photo emission coefficient at each wavelength interval then includes a lot of transitions. In practice, there are more than 100 thousands emission lines at each wavelength interval.

The result of the modeling is plotted in Fig. 5.4(b). The total photon emission coefficient, f_{PEC}, of W^{26+} (dotted line) is clearly larger than that of W^{24+} (solid line) and W^{25+} (dashed line). The emission coefficient is approximately constant at $T_e \geq 0.8$ keV, while it is much sensitive to the electron temperature at $T_e \leq 0.4$ keV. In the toroidal plasma, however, such tungsten ions always stay at a fixed narrow temperature window because the electron temperature largely changes along the plasma radial direction (see Fig. 5.2(a)). Therefore, the emission intensity is not so sensitive to the central electron temperature, if the central electron temperature is not so low that the tungsten ions stay at the plasma center. As the central electron temperature after the tungsten pellet injection is maintained above 1 keV, the W^{24+}-W^{26+} ions always exist in a certain radial location during the whole n-NBI phase (see Figs. 5.1 and 5.2(a)).

In Fig. 5.4(c), the photon emission coefficient of W^{24+}, W^{25+} and W^{26+} at 32.16-33.32, 30.69-31.71 and 29.47-30.47 Å is calculated with ADAS code (CL version, e.g. data file "arf40_cl#w24.dat"). In this version 28-29 electron configurations are considered, while an energy level splitting among sublevels is not taken into consideration. The photon

emission coefficient of the W^{24+} ion obtained from ADAS code is three times larger than that from the present CR model. A cascade process from higher excited levels may enhance the photon emission coefficient in the ADAS code calculation. The photon emission coefficient of the W^{26+} ion is considerably different from other two coefficients. In the ADAS calculation the number of tungsten lines is only one for the W^{24+} ion at 32.16-33.32 Å, while it is two for the W^{25+} and W^{26+} ions at 30.69-31.71 and 29.47-30.47 Å, respectively.

The photon emission coefficients of W^{24+}-W^{26+} at wavelength intervals of 32.16-33.32, 30.69-31.71 and 29.47-30.47 Å from the present CR model are replotted as a function of normalized plasma radius in Fig. 5.5 with solid, dashed and dotted lines, respectively The plot is done for the electron temperature profile at t = 4.7 s in Fig. 5.1. It is clear that the value of f_{PEC} is not so sensitive to T_e, at least, at $\rho \leq 0.85$.

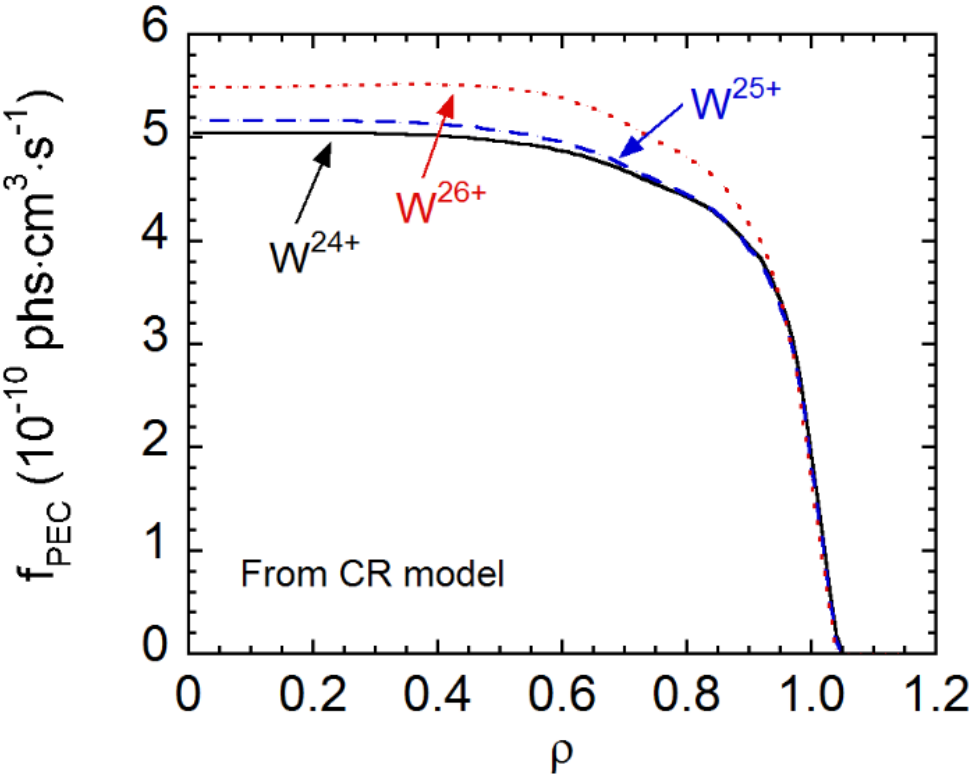

Fig. 5.5 Photon emission coefficients of W^{24+} (32.16-33.32 Å), W^{25+} (30.69-31.71 Å) and W^{26+} (29.47-30.47 Å) from the present CR model against normalized radius at t = 4.7 s in Fig. 5.2.

5.2.3 Error estimation in local emissivity profile analysis

Abel inversion method is applied to reconstruct the local emissivity profile from the measured vertical intensity profile. In LHD it has been experimentally certificated that the intensity of line emissions from tungsten ions behaves as a function of the magnetic surface and any up-down asymmetry has not been observed in the tungsten spectrum [11]. Then, the magnetic surface necessary for the reconstruction is calculated with three-dimensional equilibrium code, Variational Moments Equilibrium Code (VMEC) [12]. The local emissivity profile is expressed by the following matrix;

$$\varepsilon(\rho) = L^{-1}I(Z), \qquad (1)$$

where $\varepsilon(\rho)$, L and I(Z) are the local emissivity profile [photons$\cdot$cm$^{-3}\cdot$s^{-1}], a matrix of chord length [cm] and the vertical intensity profile [photons$\cdot$cm$^{-2}\cdot$s^{-1}], respectively.

At the first step of Abel inversion, an appropriate set of magnetic surfaces is determined with the VMEC calculation so that the electron temperature profile along major plasma radius can be symmetric against a derived normalized radius, ρ, between inboard and outboard sides, since the magnetic surface structure is a function of pressure profile. The most appropriate magnetic surface structure is then determined by adjusting the pressure profile and by minimizing the difference between two temperature profiles at inboard and outboard sides.

It is important to estimate the uncertainty in the local emissivity profile calculated with Abel inversion method in evaluating the tungsten ion density. Figures 5.6(a)-(c) show an example of the vertical intensity of W^{24+} emission at 32.16-33.32 Å, the chord length of sight lines and the local W^{24+} emissivity as a function of the normalized radius at plasma axis of R_{ax} = 3.6 m. Here, the pressure profile of $P(\rho) = P_0(1-\rho^8)(1-\rho^2)$, which is expressed by '(8020)', is used for the calculation with volume-averaged beta of 0.44%, where P_0 is the central plasma pressure. In addition, the magnetic surface at $\rho > 1.0$ outside LCFS is assumed in a usual way, i.e. a simple expansion of the magnetic surface contour at $\rho = 1.0$.

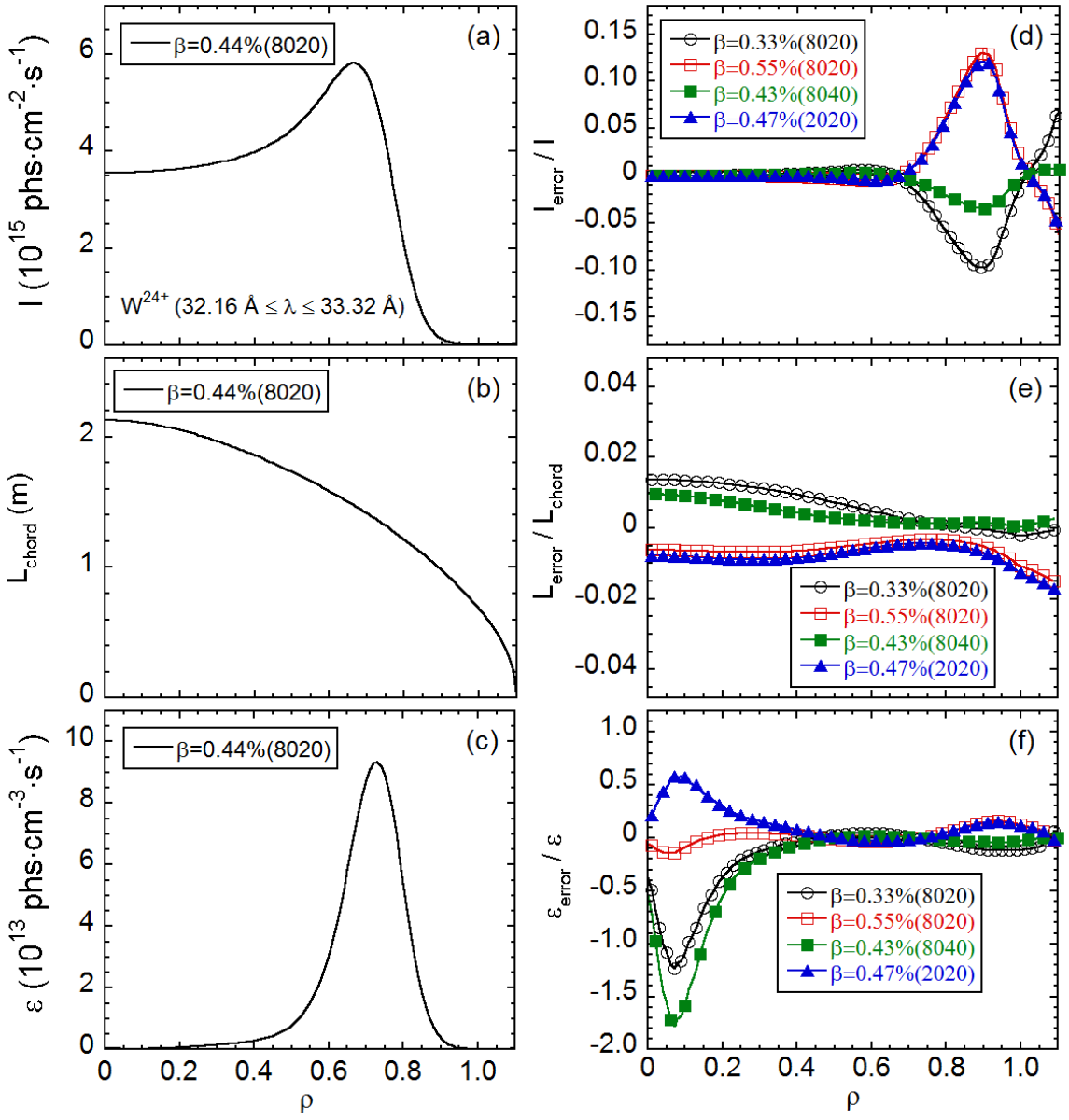

Fig. 5.6 (a) Line-integrated vertical intensity at 32.16-33.32 Å taken at Δt = 0.3 s after tungsten pellet (tungsten wire: 0.05 mm^{ϕ} × 1.0 mm^{L}) injection, (b) observation chord length, (c) local emissivity after Abel inversion for β = 0.44% (8020) at R_{ax} = 3.60 m, and normalized errors of (d) line-integrated vertical intensity, I_{error}/I, (e) observation chord length, L_{error}/L_{chord} and (f) local emissivity, $\varepsilon_{error}/\varepsilon$ for different β and pressure profiles. Notation of "β = 0.44% (8020)" means pressure profile of $P(\rho)=P_0(1-\rho^8)(1-\rho^2)$ with volume-averaged beta of 0.44%, where P_0 is central pressure.

The uncertainty of the intensity profile, I(0.44%_8020), in Fig. 5.6(a) analyzed with β = 0.44% and pressure profile of (8020) is estimated by comparing with an intensity profile, I(β_P), analyzed with different β value and pressure profile. Then, the uncertainty is obtained by

$$(I(\beta\_P) - I(0.44\%\_8020)) / I(0.44\%\_8020) = I_{error} / I(0.44\%\_8020), \qquad (2)$$

where, I_{error} is defined as a difference between two intensity profiles at β = 0.44% (8020) in Fig. 5.6(a) and at other magnetic surface structures with different β value and pressure profile. The result is shown in Fig. 5.6(d). From the figure, it is found that the uncertainty is bigger at a radial location where the intensity rapidly changes. It is also found that the value of I_{error} / I has a different sign at different β values with the same pressure profile of (8020) and at different pressure profiles with similar β values. It indicates the present choice, i.e. β = 0.44% and (8020) pressure profile, is adequate for analyzing the profile.

The definition in the uncertainty estimation of chord length, L, and local emissivity profile is also the same as the intensity profile, of which the result is shown in Figs. 5.6(e) and 5.6(f), respectively. The value of L_{error} / L_{chord} in Fig. 5.6(e) shows a relatively small difference in the whole radial location for all the cases with different β values and pressure profiles. It means the L_{chord} does not bring any significant effect on the local emissivity profile. On the contrary, the value of ε_{error} / ε in Fig. 5.6(f) has a large error in the vicinity of plasma center except for the case of β = 0.55% and (8020) pressure profile. It strongly suggests the choice of an adequate magnetic surface structure is extremely important to reduce the uncertainty in analyzing the local emissivity profile. Thus, the uncertainty in the local emissivity profile analyzed from the measured intensity profile can be estimated to be $\pm$17% as the maximum value in the vicinity of $0.5 \le \rho \le 1.0$ where the W^{24+} ion exists.

5.2.4 Evaluation of W^{24+}-W^{26+} ion density profiles

The vertical intensity profile of UTA lines at 32.16-33.32 Å from the W^{24+} ion, which is measured with EUV_Short2 spectrometer, is plotted in Fig. 5.7(a) for three different central electron temperatures of T_{e0} = 2.19 (dashed line), 1.95 (solid line) and 1.82

keV (dotted line) at t = 4.6 s, 4.8 s and 4.9 s, respectively. As a function of time the peak intensity near Z = 0.32 m decreases and the peak position moves inside toward the plasma center. The local emissivity profile reconstructed from the vertical intensity profile is shown in Fig. 5.7(b). Dependence of the peak position in the local emissivity profile on the electron temperature is clearly seen in the figure.

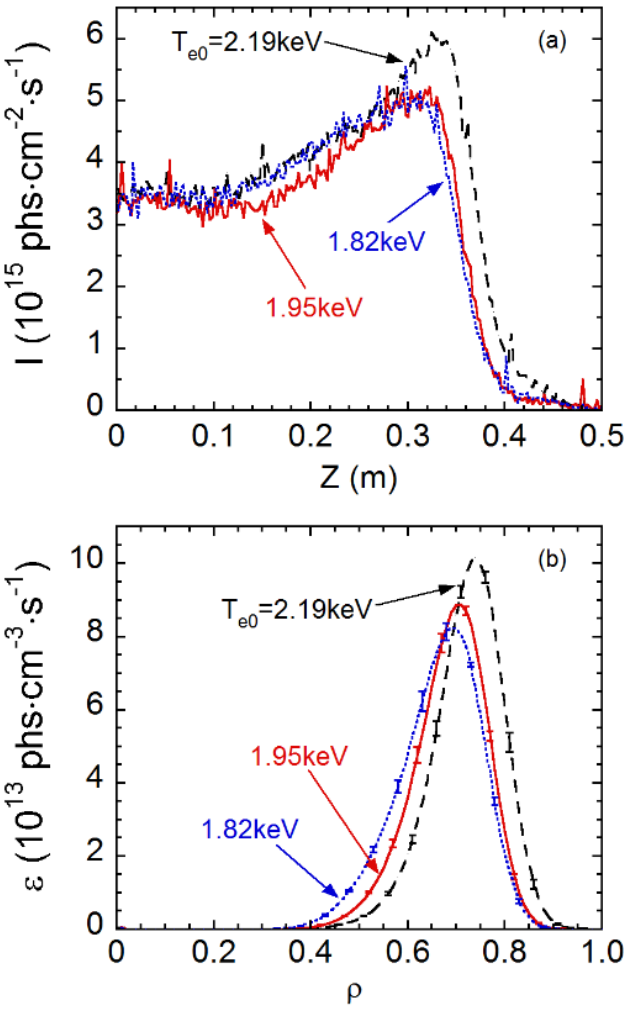

Fig. 5.7 (a) Vertical intensity and (b) local emissivity profiles of W^{24+} at wavelength interval of 32.16-33.32 Å plotted at different central electron temperatures of T_{e0} = 2.19 (dashed line), 1.95 (solid line) and 1.82 keV (dotted line).

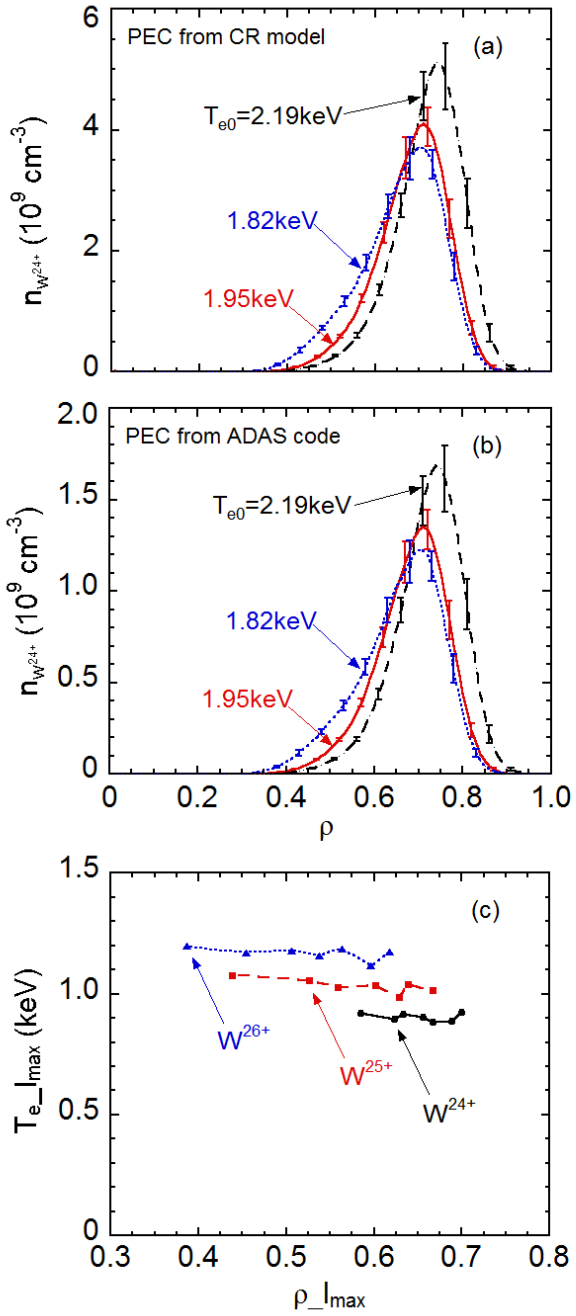

Fig. 5.8 Density profiles of W^{24+} ions at T_{e0} = 2.19 (dashed line), 1.95 (solid line) and 1.82 keV (dotted line) using photon emission coefficient calculated with (a) the present CR model and (b) ADAS code. (c) Electron temperature where the vertical intensity profile of W^{24+} (32.16-33.32 Å), W^{25+} (30.69-31.71 Å) and W^{26+} (29.47-30.47 Å) takes the maximum value as a function of normalized radius at the intensity maximum.

Based on the local emissivity profile, the density profile of W^{24+} ions, $n_w24+(\rho)$, can be then calculated by an equation of

$$n_w24+(\rho) = \varepsilon(\rho) / (n_e(\rho) \times f_{PEC}(T_e, n_e)), \quad (3)$$

where $n_e(\rho)$ is the electron density profile, and $f_{PEC}(T_e, n_e)$ is calculated with the present CR model shown in Fig. 5.4(b). The W^{24+} ion density profiles analyzed at T_{e0} = 2.19 (dashed line), 1.95 (solid line) and 1.82 keV (dotted line), which are the same as the case of Fig. 5.7, are shown in Fig. 5.8(a). The W^{24+} ion density distributes in range of 3-5 $\times$ 10^9 cm^{-3}. The density profile of W^{24+} ions is also analyzed using $f_{PEC}(T_e, n_e)$ from ADAS code shown in Fig. 5.4(c). The result is plotted in Fig. 5.8(b). It is obvious that the W^{24+} ion density in Fig. 5.8(a) is roughly three times larger than that in Fig. 5.8(b), reflecting the difference in the photon emission coefficient.

In Fig. 5.8(c), the electron temperature where the vertical intensity profile of W^{24+} (32.16-33.32 Å), W^{25+} (30.69-31.71 Å) and W^{26+} (29.47-30.47 Å) takes the maximum value is plotted against the peak position in the vertical intensity profile. The data point in the figure is taken at 4.5-5.1 s in Fig. 5.1. It is clear that the electron temperature at the intensity peak in the vertical profile is almost unchanged, even if the peak position moves inwardly reflecting the temporal electron temperature decrease. This fact reduces the uncertainty due to the temperature dependence of the photon emission coefficient.

Based on the analyzed W^{24+} ion density profile, the total tungsten density, $n_w(\rho)$, is estimated from an equation of

$$n_w(\rho) = n_w24+(\rho) / f_{ab}(T_e, n_e), \quad (4)$$

where $f_{ab}(T_e, n_e)$ is the fractional abundance of W^{24+} shown in Fig. 5.4(a). Here, the total tungsten density is estimated only in the vicinity of ρ = 0.7 where the W^{24+} ion exists. The result is shown in Figs. 5.9(a) and (b) for the f_{PEC} from the present CR model (solid line) and ADAS code (dashed line), respectively. A constant value of $f_{ab}(T_e, n_e)$ at the temperature where the W^{24+} ion has the maximum abundance, i.e. $f_{ab}(T_e, n_e)$ = 0.25 at T_e = 0.64 keV, is used in the estimation. It is shown in the figure that the total tungsten density continuously decreases after the tungsten pellet injection (t = 4.3 s), while the reduction becomes slower as a function of time.

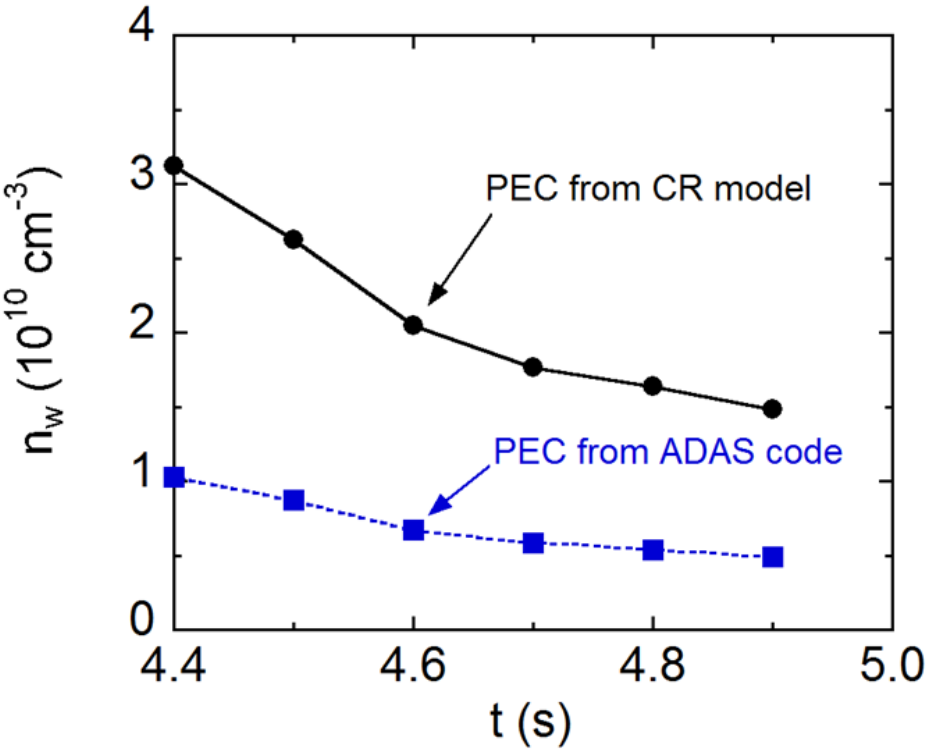

Fig. 5.9 Time trace of total tungsten density in the vicinity of $\rho = 0.7$ calculated at peak value of W^{24+} ion density profile (solid circles: the present CR model, solid squares: ADAS code).

From the profile measurement of EUV line emissions in several tungsten ionization stages, the tungsten ion slowly expands in the radial direction toward the plasma center. The result in Fig. 5.9 indicates such an expansion process. In the present case the tungsten ion almost completes the expansion at $\Delta t = 0.5$ s after the pellet injection, i.e. $t = 4.8$ s in Fig. 5.9. If all the tungsten ions are uniformly distributed in the LHD plasma, we obtain $n_W = 4.1 \times 10^9$ cm^{-3} from the number of tungsten particles injected by the pellet. The n_W from f_{PEC} with the present CR model is 3.6 times larger than the n_W estimated from the pellet size. If it is compared with n_W based on f_{PEC} from ADAS code, the n_W from ADAS code is 1.2 times larger than the n_W from the pellet size. At present, however, it is difficult to discuss on the accuracy in the f_{PEC} because another model in the ADAS code has entirely different values for the f_{PEC} due to different number of electron configurations in the model. In addition, the present CR model includes possible all atomic processes and J-resolved

levels, while the dielectric recombination is not included. We need further efforts for quantitatively and accurately understanding the UTA line intensity.

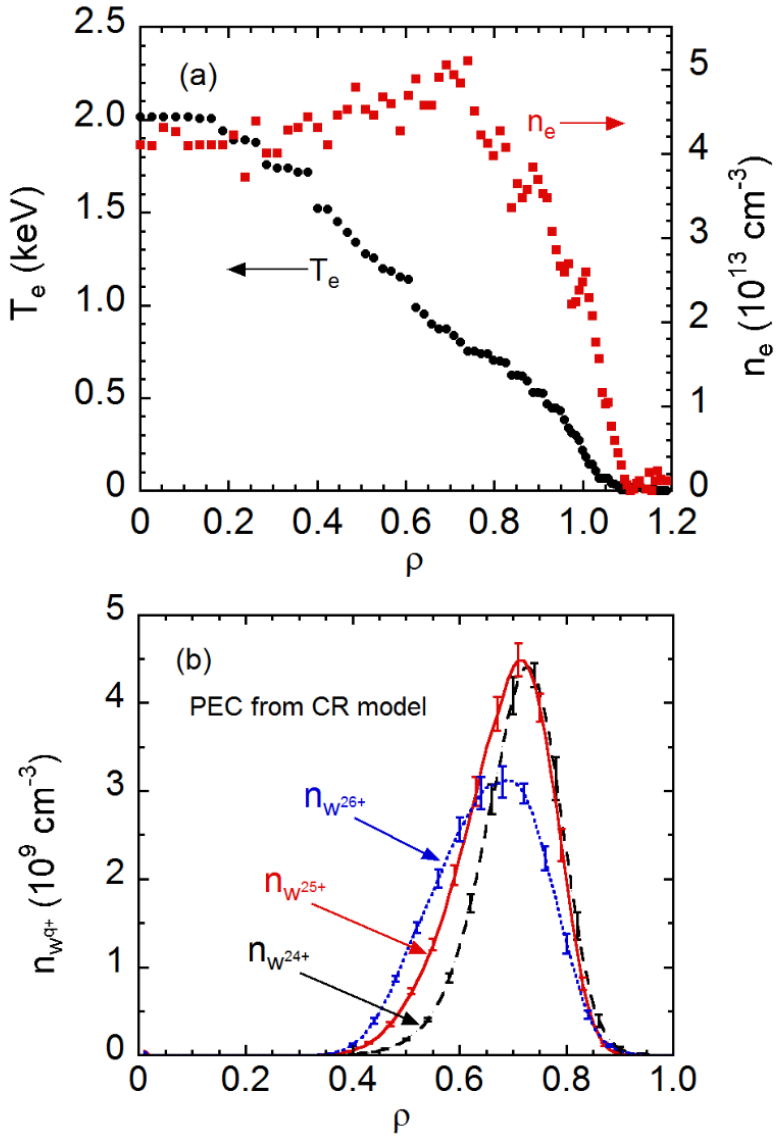

Fig. 5.10 (a) Electron density (solid squares) and temperature (solid circles) profiles and (b) tungsten density profiles of W^{24+} (dashed line), W^{25+} (solid line) and W^{26+} (dotted line) ions at t = 4.7 s in Fig. 5.2.

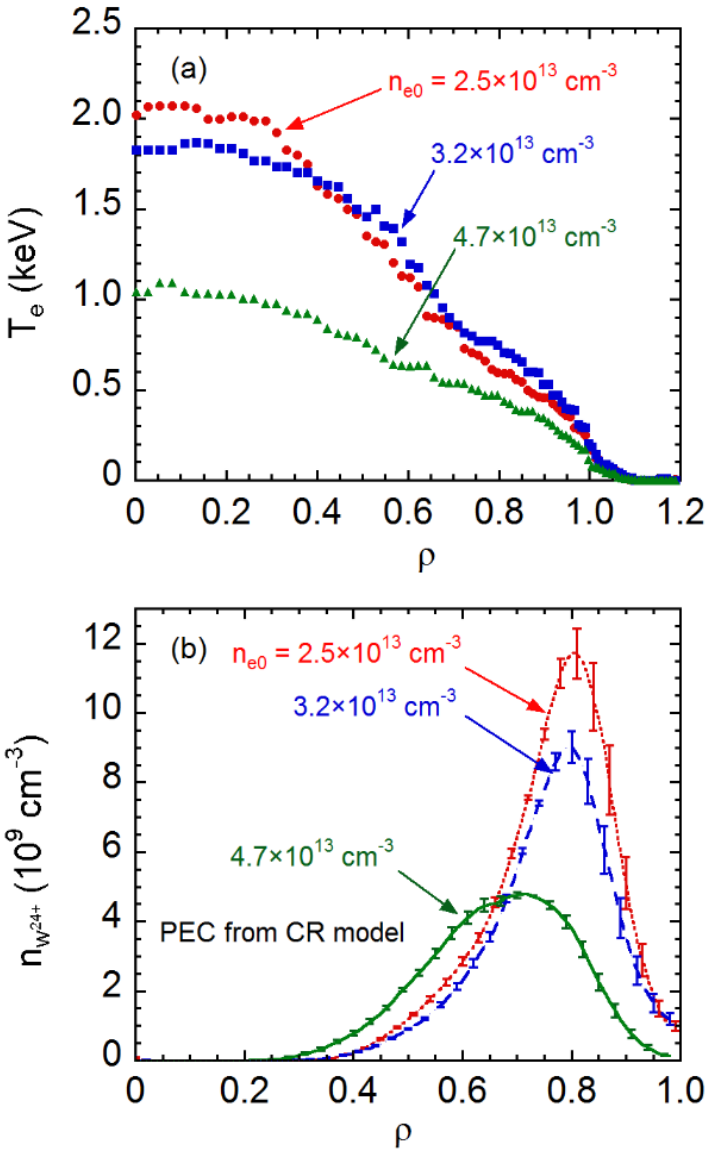

Fig. 5.11 (a) Electron temperature and (b) W^{24+} ion density profiles at Δt = 0.1 s after pellet injection (0.06 mm^{ϕ} × 1.0 mm^{L}) in different electron densities of 2.5 × 10^{13} cm^{-3} (dotted line), 3.2 × 10^{13} cm^{-3} (dashed line) and 4.7 × 10^{13} cm^{-3} (solid line).

The tungsten ion density profile of W^{24+}, W^{25+} and W^{26+} ions is analyzed at t = 4.7 s, as shown in Fig. 5.10(b) with dashed, solid and dotted lines, respectively. The electron density and temperature used for the analysis are also shown in Fig. 5.10(a). It is found that the peak density in the W^{26+} ion density profile is clearly smaller than those in the W^{24+} and W^{25+} ion density profiles. Since the W^{26+} ion abundance has a wider distribution against the electron temperature compared to the W^{24+} and W^{25+} ions, more ionization stages of tungsten ions exist at the temperature range of the W^{26+} ion. Then, the total tungsten density is calculated from the three density profiles in Fig. 5.10(b) using f_{PEC} from the present CR model. The value of n_W is reasonably similar to each other in the vicinity of ρ = 0.7, i.e. $n_W=1.7 \times 10^{10}$ cm^{-3} from W^{24+}, $n_W=1.8 \times 10^{10}$ cm^{-3} from W^{25+} and $n_W=1.4 \times 10^{10}$ cm^{-3} from W^{26+}. It indicates that the coefficient of f_{PEC} from the present CR model is sufficiently accurate in the relative value among three wavelength intervals of the UTA line.

5.3. Discussions on the tungsten ion density

In order to examine the electron density dependence of W^{24+} ion density, the tungsten pellet (tungsten wire size: 0.06 mm^{ϕ} × 1.0 mm^{L}) has been injected in NBI discharges at different densities of 2.5, 3.2 and 4.7 × 10^{13} cm^{-3} . The number of particles included in the pellet is $N_W = 1.7 \times 10^{17}$ for tungsten. The electron temperature profile at Δt = 0.1 s after the pellet injection is plotted in Fig. 5.11(a). The central electron temperature decreases from 2 keV to 1 keV when the density increases. The W^{24+} ion density profile analyzed for the three density cases in the same way as before is plotted in Fig. 5.11(b). The W^{24+} ion density in the discharge with $n_e = 4.7 \times 10^{13}$ cm^{-3} is clearly smaller than that in lower density discharges because the tungsten density decay after the pellet injection is quicker in higher density discharges. The W^{24+} ion density decay rate is 9 × 10^9 cm^{-3}/s for $n_e = 2.5 \times 10^{13}$ cm^{-3}, 15 × 10^9 cm^{-3}/s for $n_e = 3.2 \times 10^{13}$ cm^{-3} and 24 × 10^9 cm^{-3}/s for $n_e = 4.7 \times 10^{13}$ cm^{-3}.

The tungsten pellet with different tungsten wire sizes of 0.03 mm^{ϕ} × 1.0 mm^{L}, 0.05 mm^{ϕ} × 1.0 mm^{L} and 0.06 mm^{ϕ} × 1.0 mm^{L} has been also injected in NBI discharges with n_e = 2.2, 3.0 and 3.2 × 10^{13} cm^{-3}, respectively. The central electron temperature before the pellet injection has a similar value of 2.6 keV for three discharges. The electron

temperature profile at Δt = 0.1 s after the pellet injection is shown in Fig. 5.12(a). The electron temperature at the small pellet (0.03 mm^{ϕ}) injection is obviously lower than that at large pellets (0.05 mm^{ϕ} and 0.06 mm^{ϕ}). Since the speed of a tungsten pellet injected with pressurized He gas is higher at smaller tungsten wire size, such a high-speed pellet is radially deposited at deeper position. The tungsten ionization from the pellet cloud then becomes quicker because the electron temperature is high at the pellet evaporation and resultantly the radiation from tungsten ions rapidly increases in the smaller tungsten pellet.

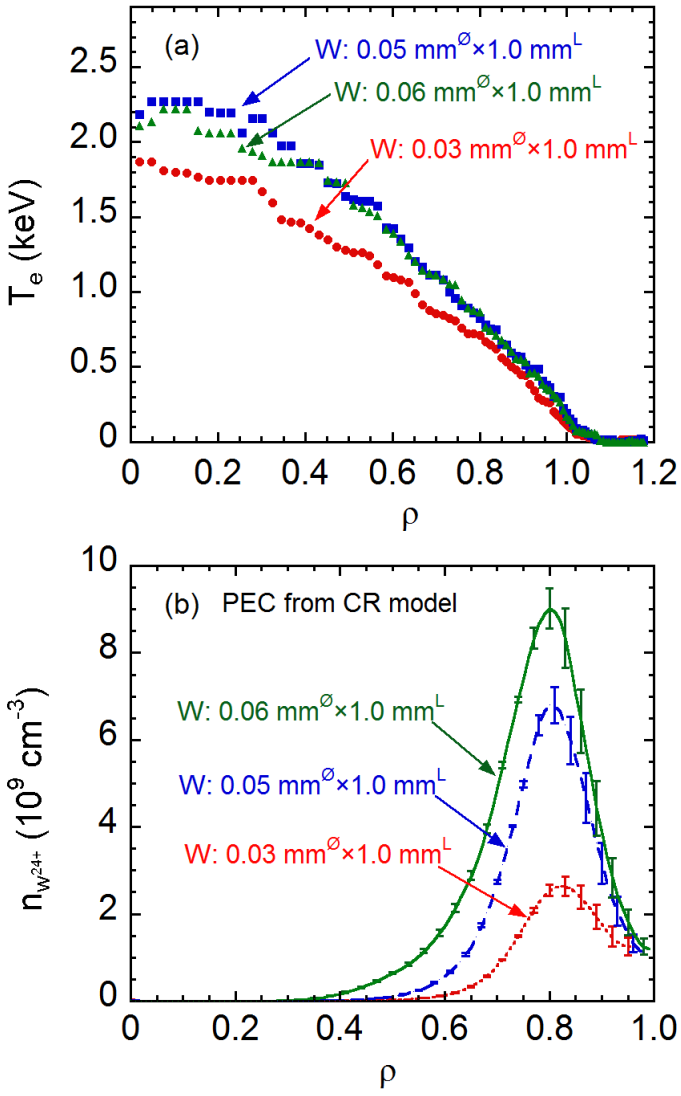

Fig. 5.12 (a) Electron temperature and (b) W^{24+} ion density profiles at Δt = 0.1 s after pellet injection with different tungsten pellet seizes of 0.03 mm^{ϕ} × 1.0 mm^{L} (dotted line), 0.05 mm^{ϕ} × 1.0 mm^{L} (dashed line) and 0.06 mm^{ϕ} × 1.0 mm^{L} (solid line).

The W^{24+} ion density profile analyzed at $\Delta t = 0.1$ s for three cases is shown in Fig. 5.12(b). The peak position of the W^{24+} ion density profile locates in a similar radial location near $\rho \sim 0.8$ because the target discharge is almost identical for the three cases. The tungsten W^{24+} ion density changes according to the tungsten wire size. Here, we evaluate a ratio of the total tungsten density to the injected number of tungsten particles, n_W / N_W. The ratio is 2.4×10^{-7} for 0.03 mm^{ϕ}, 2.2×10^{-7} for 0.05 mm^{ϕ} and 2.0×10^{-7} for 0.06 mm^{ϕ}. We understand that all the ratios have similar values. Therefore, it indicates all injected tungsten particles are fairly well confined in the plasma after the ablation of the tungsten pellet.

5.4. Summary

A series of experiments on tungsten spectroscopy are conducted in LHD by injecting a tungsten pellet to attempt an evaluation of a tungsten ion density. The fractional abundance of W^{22+}-W^{34+} ions is calculated with ADAS code and a photon emission coefficient for W^{24+} , W^{25+} and W^{26+} ions at wavelength intervals of 32.16-33.32, 30.69-31.71 and 29.47-30.47 Å is calculated with CR model which is developed for the analysis of UTA spectra. Uncertainty in a local emissivity profile of the W^{24+} ion at 32.16-33.32 Å is evaluated with magnetic surface structures which are deformed as a function of a plasma pressure profile. The result indicates an importance on the use of an adequate magnetic surface to reduce the uncertainty.

The W^{24+} ion density is then evaluated from electron density and temperature profiles, the local emissivity profile and the photon emission coefficient. The error of W^{24+} density is evaluated from the errors of the local emissivity profile, electron density and photon emission coefficients. Then, the total tungsten density in the vicinity of $\rho = 0.7$ is calculated from a peak value of the W^{24+} ion density profile based on the fractional abundance at an electron temperature at which the W^{24+} abundance takes the maximum value. The tungsten density calculated with the photon emission coefficient from the present CR model is roughly four times bigger than the tungsten density estimated from the pellet size, while the density calculated from a CL version of ADAS code is considerably closer to the density from the pellet size, i.e. within two times. However, the present result does not indicate inaccuracy in the present CR model because it includes possible all the atomic processes and a huge number of J-resolved sublevels, while it does not include

dielectronic recombination. We need further efforts to qualitatively understand the UTA spectrum in both fields of experiment and modeling.

References

[1] E.J. Doyle et al., Nucl. Fusion **47**, S18 (2007).
[2] A.W. Leonard et al., J. Nucl. Mater. **266**, 109 (1999).
[3] X.L. Huang et al., Rev. Sci. Instrum. **85**, 11E818 (2014).
[4] T. Morisaki et al., Contrib. Plasma Phys. 40, 266 (2000).
[5] S. Morita et al., Nucl. Fusion **53**, 093017 (2013).
[6] Y. Liu et al., J. Appl. Phys. **122**, 233301 (2017).
[7] I. Murakami et al., Nucl. Fusion **55**, 093016 (2015).
[8] H.P. Summers, The ADAS User Manual, version 2.6 http://www.adas.ac.uk (2004).
[9] H.A. Sakaue et al., Phys. Rev. A **92**, 012504 (2015).
[10] S. Morita et al., AIP Conf. Proc. 1545, 143 (2013).
[11] Y. Liu et al., Rev. Sci. Instrum. **87**, 11E308 (2016).
[12] S.P. Hirshman et al., Comput. Phys. Commun. **43**, 143 (1986).

Chapter 6

Effect of neutron and γ-ray on charge-coupled device for vacuum/extreme ultraviolet spectroscopy in deuterium discharges of Large Helical Device

6.1. Introduction

In fusion research, charge-coupled device (CCD) has been commonly used for spectroscopic diagnostic systems [1-9]. Since deuterium (D) gas is usually used for fueling in the fusion experiment to maintain the discharge, a lot of neutrons with energy of 2.45 MeV are produced during the D-D operation. Tritons (T) generated by the D-D reaction have a subsequent reaction with the deuteron, i.e., D-T reaction, and yield a neutron with higher energy of 14.1 MeV. It is well known such neutrons cause serious problems to the CCD system, including a background noise. In addition, γ-rays produced through the neutron capture are emitted from plasma facing components and laboratory structural materials, which also create a huge background noise on the CCD [10-12]. These noises lower the CCD capability of measuring a high-quality spectrum, e.g. significant decrease in

signal-to-noise ratio. In the worst case, the neutron brings a permanent defect to the CCD pixel.

In Large Helical Device (LHD), a deuterium experiment was initiated in March 2017 and continued for the following four months under an operational constraint of annual neutron yield limited to 2.1×10^{19} [13]. Then, the D- D experiment over four months has been controlled not to exceed the annual regulation value. During the D-D experiment, totally 3.7×10^{18} neutrons have been yielded mainly through a beam-target reaction. The γ-ray energy distribution is simulated for the D-D experiment of LHD [14]. The result indicates that the γ-ray flux is dominant at $E_\gamma \leq 1$ MeV, while the γ-ray energy distributes in a wide range of 0.01-12.0 MeV.

Many CCDs are equipped on vacuum spectrometers working in vacuum ultraviolet (VUV), extreme ultraviolet (EUV) and X-ray ranges. Although these CCDs are located at different toroidal positions and different distances from the plasma center of LHD, a large amount of noise caused by neutrons and γ-rays have been observed in all CCDs during the D-D experiment. An effect of neutrons and γ-rays on the CCD is then examined against the CCD location. In addition, two special shielding boxes made of polyethylene contained 10% boron and lead are used to make a quantitative analysis on the CCD background noise by changing the shielding material.

6.2. Experimental setup

In LHD, VUV, EUV and X-ray spectrometers are used in vacuum condition by directly connecting to a diagnostic port. The same back-illuminated CCD (Andor DO420-BN and DO920-BN) is used for all the spectrometers reported here. All the CCDs are operated at -20 °C for reducing thermal noise. The size of the CCD image area is 26.6×6.7 mm^2 and the number of pixels is 1024×255 (26×26 μm^2/pixel). The arrangement of these spectrometers in LHD is shown in Fig. 6.1. Impurity behavior in LHD plasmas has been routinely measured with an impurity monitor system installed on #10-O port. Several VUV and EUV spectrometers are arranged at a backside square port (size: 30×220 cm^2) of the impurity monitor system. A distance from the plasma center (R_{ax} = 3.60 m) of LHD to the CCD is roughly 9.5 m for all the spectrometers at the impurity monitor system. Three 20 cm normal incidence VUV spectrometers named 109LVUV, 106RVUV and 102RVUV mainly monitor the line spectrum from light impurities in the wavelength range of 300-

1050 Å, 1000-1850 Å and 1550-2400 Å, respectively [5]. Temporal evolutions of the VUV spectrum are observed every 5 ms in a full-binning mode operation of the CCD. In addition, two grazing-incidence EUV spectrometers called EUV_Short and EUV_Long mainly monitor the line spectrum from metallic impurities in the wavelength range of 10-130 Å and 50-500 Å, respectively. The spectrum is also sequentially obtained every 5 ms as well as the VUV spectrometer.

In the 10-O port, in addition, the CCD of a space-resolved EUV spectrometer called EUV_Long2 is placed at a distance of 9.5 m away from the plasma center of LHD.

A Johann-type x-ray crystal spectrometer (XCS) [9] is installed on #3-O port for monitoring the ion temperature at plasma core by measuring the Doppler broadening of He-like resonance line of ArXVII. The ion temperature is monitored every 5 ms in a full binning mode of the CCD. The CCD is placed at a distance of 7 m away from the plasma center of LHD.

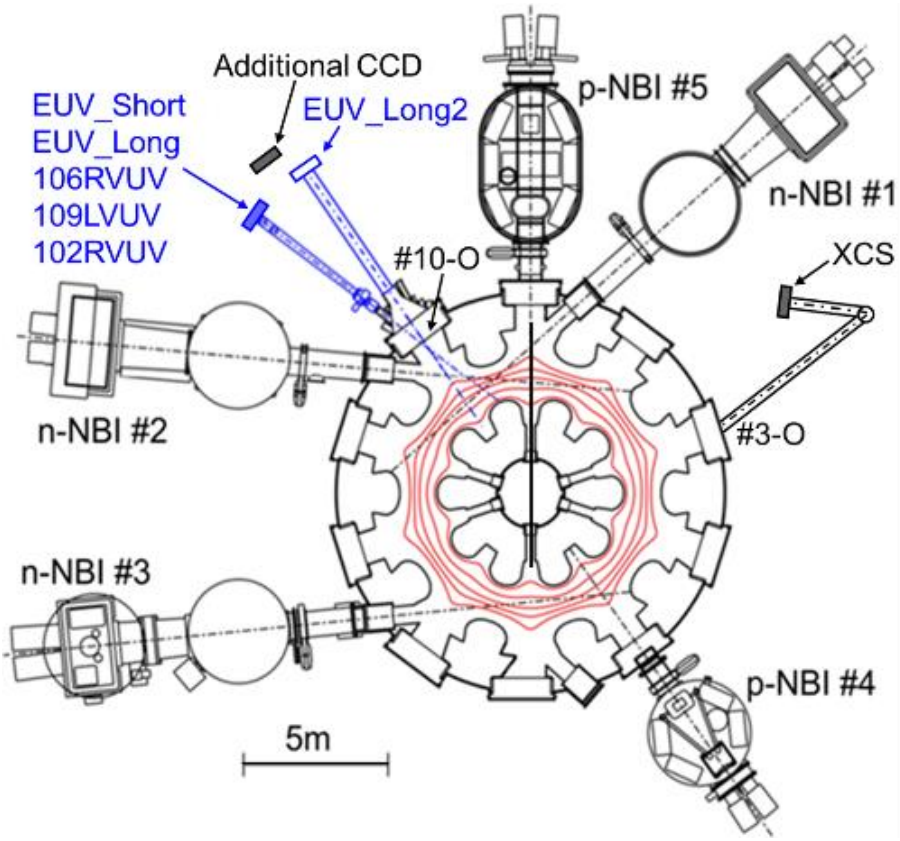

Fig. 6.1. Arrangement of two EUV spectrometers (EUV_Short and EUV_Long), three VUV spectrometers (106RVUV, 109LVUV and 102RVUV), one Johann-type x-ray crystal spectrometer (XCS) and one additional CCD in LHD.

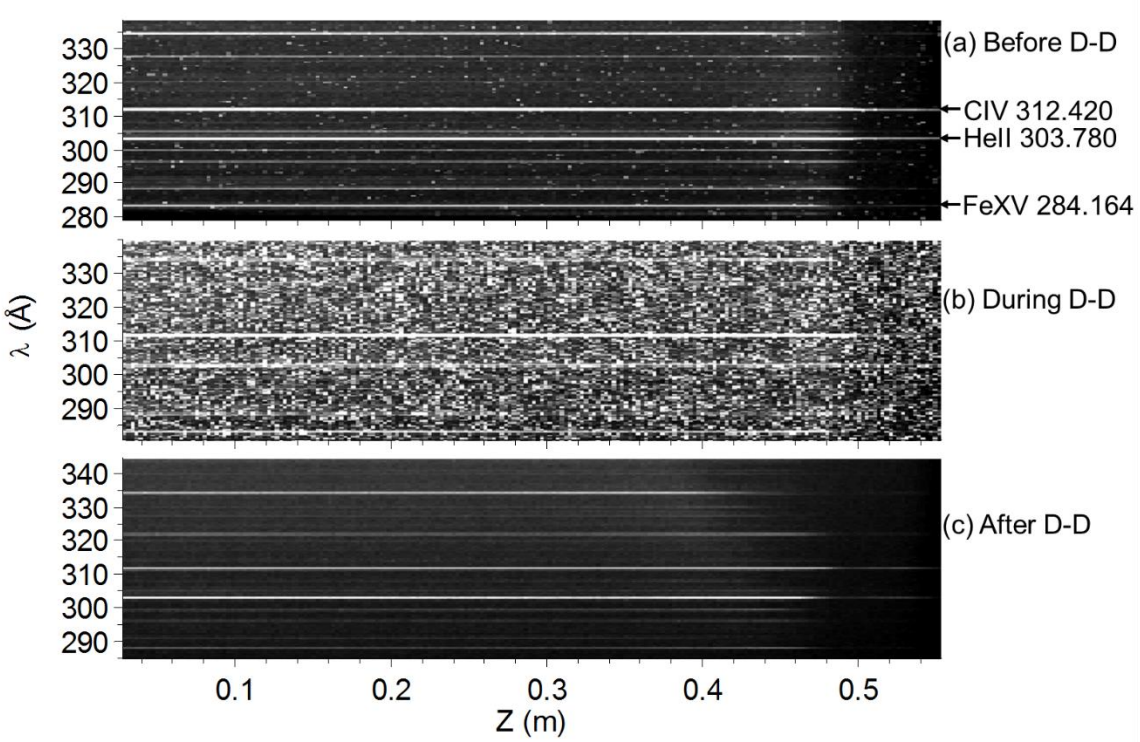

Fig. 6.2 CCD images taken from EUV_Long2 in (a) NBI discharge before D-D experiment with exposure time of 61.48 ms (#130543: N_{CCD} = 0.1 × 10^8 counts/s, T_e=1.2 keV, n_e=3.5 × 10^{13} cm^{-3}, P_{NBI}=18.7 MW), (b) NBI deuterium discharge during D-D experiment with exposure time of 61.21 ms (#138430: N_{CCD}=1.5 × 10^8 counts/s, S_n=1.2 × 10^{15} n/s, T_e=3.4 keV, n_e=2.1 × 10^{13} cm^{-3}, P_{NBI}=15.1 MW) and (c) hydrogen ECH discharge after D-D experiment with exposure time of 61.21 ms (#143782: N_{CCD}=0, T_e=1.8 keV, n_e=4.5 × 10^{13} cm^{-3} ,

6.3. Experimental results

6.3.1 Signal noise on CCDs of VUV, EUV and X-ray spectrometers during D-D experiment

Three CCD images measured with EUV_Long2 are shown in Figs. 6.2(a)-6.2(c), which are taken from hydrogen discharge before the D-D experiment, deuterium discharge

during the D-D experiment and hydrogen discharge after the D-D experiment, respectively. In these three discharges, the line-of-sight of EUV_Long2 is fixed to observe the upper-half LHD plasma at horizontally elongated plasma cross section. The horizontal and vertical axes of the CCD image represent the vertical direction of LHD plasma and the wavelength direction, respectively. The CCD sampling time is the same for all three images, i.e., 0.1 s. In Fig. 6.2(b), the CCD image is taken from NBI discharge with a neutron rate of $S_n = 1.2 \times 10^{15}$ n/s. Electron temperature and density and NBI port-through power at the CCD image acquisition are $T_e = 3.4$ keV, $n_e = 2.1 \times 10^{13}$ cm^{-3} and $P_{NBI} = 15.1$ MW, respectively. Two strong emission lines appeared in the middle of image are from HeII at 303.780 Å and CIV at 312.420 Å. Many noises are observed in Fig. 6.2(b) with white spots which are dominantly caused by neutrons and γ-rays. The total noise count rate, which is defined as the noise count multiplied for all CCD pixels divided by an exposure time of 61.21 ms, N_{CCD}, is 1.5×10^8 counts/s in the image of Fig. 6.2(b).

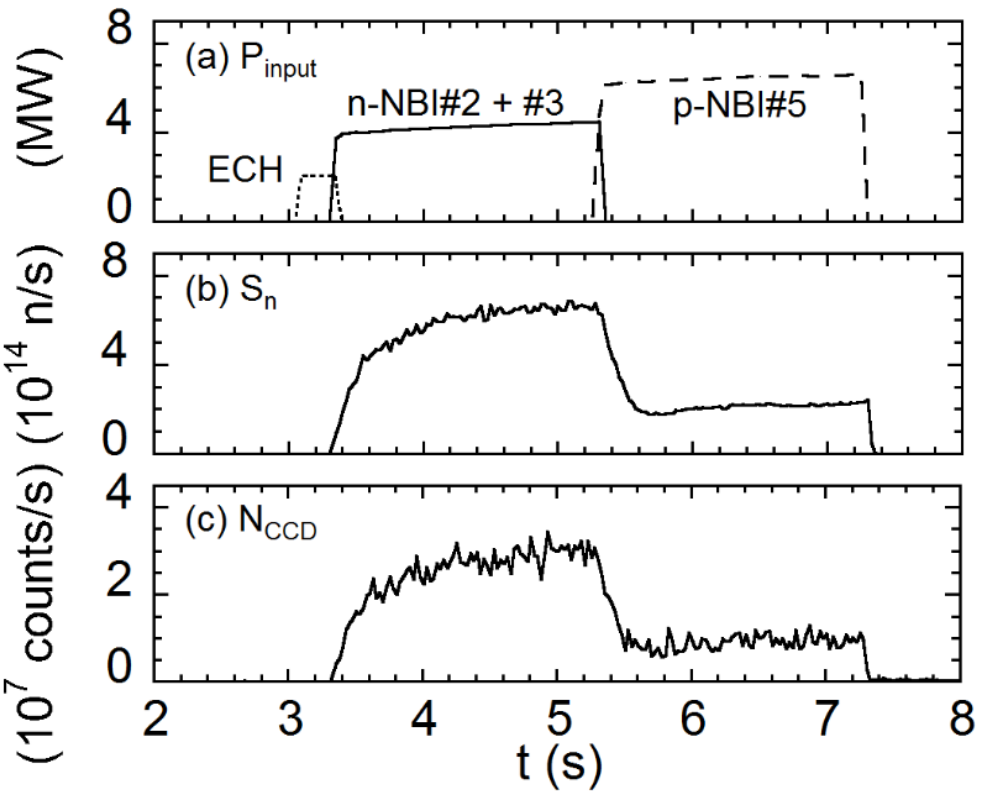

Fig. 6.3. Time behaviors of (a) input power of NBI and ECH, (b) neutron production rate and (c) total noise count rate in the additional CCD.

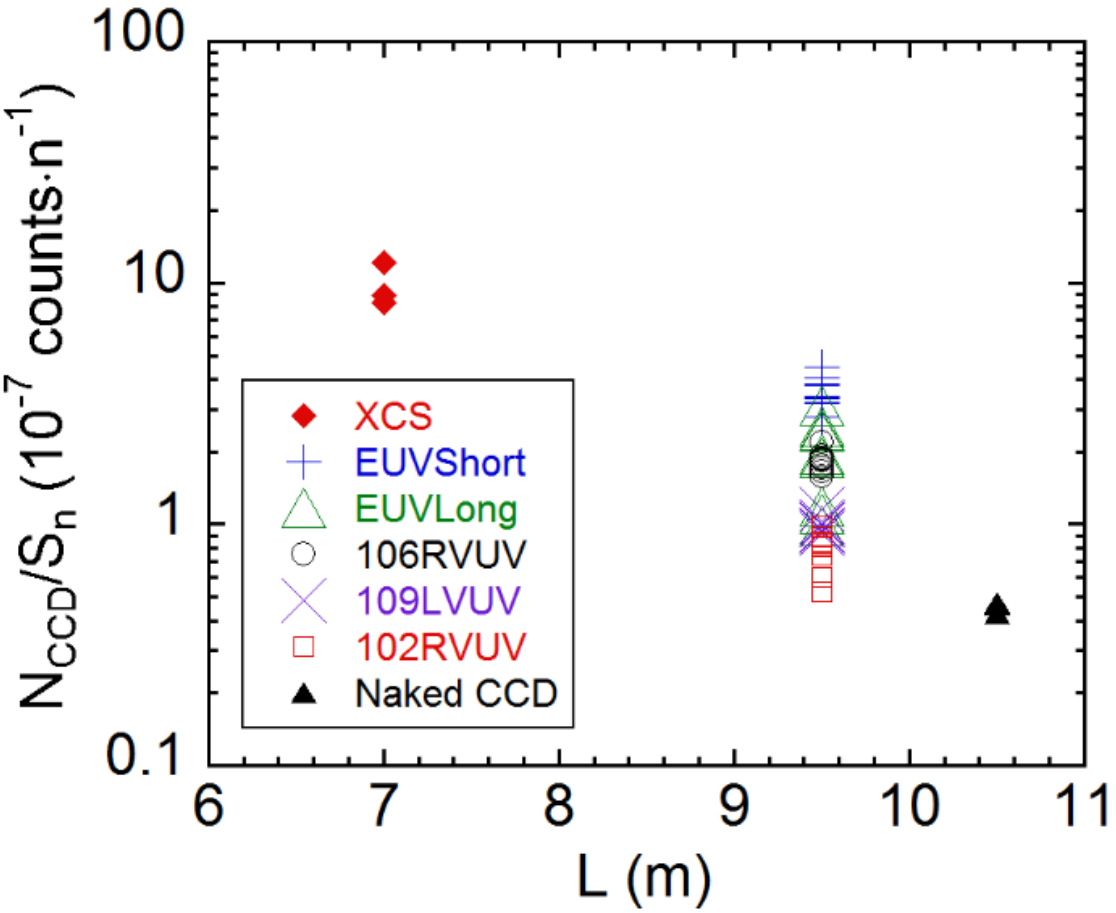

Fig. 6.4 Total noise count rate normalized by neutron production rate, N_{CCD} / S_n, against distance from CCD to plasma center (R_{ax}=3.60m) of LHD, L, for XCS, EUVShort, EUVLong, 106RVUV, 109LVUV, 102RVUV and additional CCD without shielding denoted with Naked CCD.

The CCD image in Figs. 6.2(a) and 6.2(c) is taken from hydrogen discharges with NBI (T_e = 1.2 keV, n_e = 3.5 × 10^{13} cm^{-3} and P_{NBI} = 18.7 MW) before the D-D experiment and ECH (T_e = 1.8 keV, n_e = 4.5 × 10^{13} cm^{-3} and P_{ECH} = 2.5 MW) after the D-D experiment over four months, respectively. It is noted here that the wavelength range in Fig. 6.2(c) is slightly different from other two figures. Then, the FeXV at 284.164 Å is invisible in Fig. 6.2(c). The noise detected in these images are extremely weak, while the noise from high-energy neutral particles originated in NBI fast ions[15] can be seen in Fig. 6.2(a) with small white spots[16]. The total noise count from the hydrogen NBI discharge in Fig. 6.2(a) is N_{CCD} = 0.1 × 10^8 counts/s, while the N_{CCD} from the hydrogen ECH discharge in Fig. 6.2(c) is

basically zero. No permanent damage has been observed on this CCD after the D-D experiment.

The noise during the D-D experiment is analyzed for six CCDs, i.e., three for VUV, two for EUV and one for X-ray, which are operated in the full-binning mode for measuring the spectrum as mentioned before. All these CCDs are operated without any shielding during the four-month D-D experiment. Meanwhile, an additional CCD is placed at 10.5 m away from the plasma center of LHD as shown in Fig. 6.1. It is also operated in the full-binning mode without any shielding. A typical deuterium discharge is shown in Fig. 6.3. Time behaviors of input power of NBI and ECH, neutron production rate and total noise count rate obtained in the additional CCD are displayed in Figs. 6.3(a)-(c), respectively. The CCD noise is analyzed for these seven CCDs by accumulating 200 frames during NBI heating period, e.g., 4.0-5.0 s. For the analysis, a similar plasma parameter phase is chosen for ten deuterium discharges with plasma axis position of R_{ax} = 3.60 m. The result is plotted in Fig. 6.4. The abscissa, L, indicates a distance from the CCD to the plasma center of LHD. In the vertical axis, the total noise count rate in the CCD, N_{CCD} (counts/s), is normalized by the neutron production rate, S_n (neutrons/s), because the neutron production rate is different in these ten deuterium discharges. Therefore, the value of N_{CCD}/S_n should be basically proportional to the number of incident γ-rays and neutrons, if the energy distribution of neutrons and γ-rays is unchanged at these locations where seven CCDs are placed. Then, the result in Fig. 6.4 seems to indicate that the number of neutrons and/or γ-rays decreases with the distance from the plasma. Anyway, the N_{CCD}/S_n is large for the XCS CCD which is closely placed to the LHD plasma and is small for the additional CCD denoted "Naked CCD" which is placed at the furthest position from the LHD plasma center. The value of N_{CCD}/S_n differs at least by one order of magnitude between the XCS CCD at L = 7 m and the Naked CCD at L = 10.5 m, while the noise level is still large even in the Naked CCD.

All CCDs used for the D-D experiment have been carefully checked to find certain damage. However, no permanent defect can be found in the CCD pixel as well as the result in Fig. 6.2. Only in the XCS CCD it is found that the background noise permanently increases by three times for a few pixels, which never disappear even if the CCD cooling temperature is decreased. Although it is unclear whether the damage on the XCS CCD is caused by the D-D experiment, such a negligibly small damage does not influence the actual use at all.

6.3.2 Examination of signal noise induced by neutron and γ-ray using shielding CCD

The effect of γ-rays and neutrons is then examined in four different ways using the additional CCD, as shown in Fig. 6.5. At first, the CCD is exposed to neutrons and γ-rays without any shielding (see Fig. 6.5(a)). Next, the noise is individually examined for the CCD shielded by only 1.5 cm thick lead (see Fig. 6.5(b)) and by only 10 cm thick polyethylene (see Fig. 6.5(c)). Finally, the noise is examined for the CCD shielded by both the 1.5 cm thick lead and 10 cm thick polyethylene. External dimensions of lead and polyethylene boxes are 40 cm × 30 cm ×30 cm in height and 60 cm × 50 cm ×50 cm in height, respectively. The polyethylene plate used here contains 10% boron for an effective capture of thermal neutrons after losing the energy.

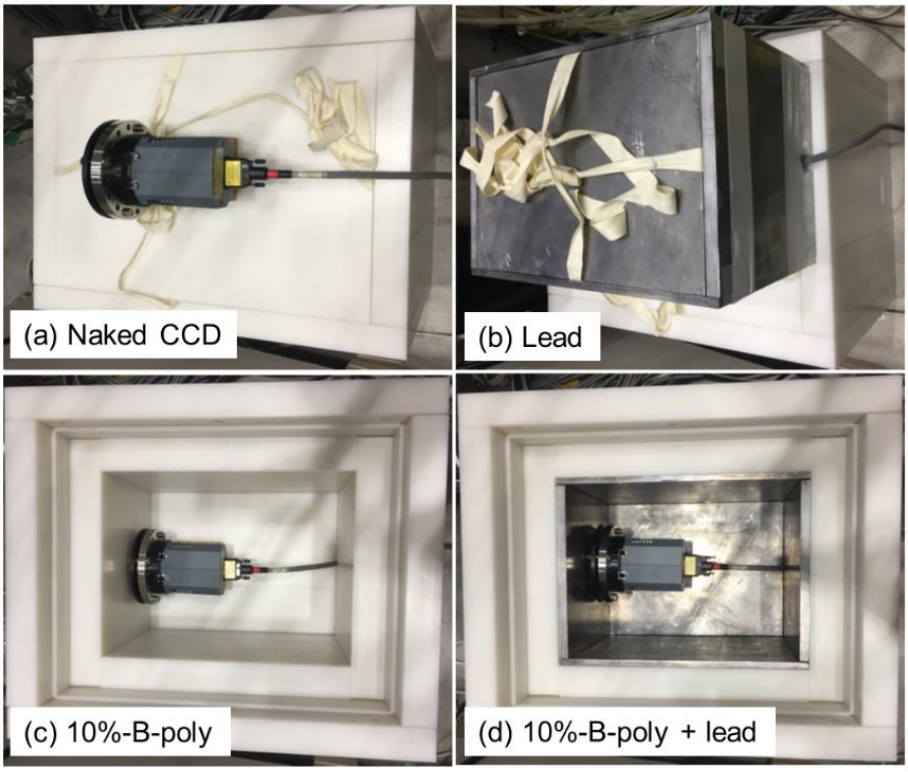

Fig. 6.5 (a) CCD without shielding, (b) CCD with lead, (c) CCD with polyethylene contained 10% boron and (d) CCD with polyethylene contained 10% boron and lead. External dimensions of lead and polyethylene boxes are 40 cm × 30 cm ×30 cm in height with a thickness of 1.5 cm and 60 cm × 50 cm ×50 cm in height with a thickness of 10 cm, respectively.

As well as Fig. 6.4, the noise count, N_{CCD}/S_n, is plotted against the total neutron rate in Fig. 6.6. The relative error for each value is less than 5%. It is found that the shielding effect of lead is clearly more effective than that of polyethylene. In order to estimate the effect of neutrons and γ-rays individually, the attenuation ratio of γ-ray, I / I_0, is calculated by the following equation of

$$I / I_0 = e^{-\mu\rho t}, \qquad (1)$$

where I_0 and I are the γ-ray flux before and after passing through the shielding material, respectively, and μ, ρ and t are the mass absorption coefficient, the density of shielding material and the thickness, respectively. The mass absorption coefficient of lead and polyethylene for γ-rays is taken from NIST Database [17]. Although the γ-ray energy distribution measurement has been attempted in LHD, the signal is always affected by many noises. Then, the γ-ray energy distribution from the simulation [14] is used for the present analysis. The analysis indicates that the averaged attenuation ratio of γ-rays in lead is 0.1914. The attenuation ratio of fast neutron against 1.5 cm thick lead is calculated to be 0.8383 based on the removal cross section [18]. Here, a shielding efficiency ratio is defined as K / K_0, where K and K_0 mean the total noise count with and without shielding, respectively. The value of K can be written by

$$K = N_{CCD} / S_n. \qquad (2)$$

From Fig. 6.6, the ratio of K / K_0 can be experimentally determined to be 57% for lead, 81% for polyethylene and 29% for lead plus polyethylene.

The lead is quite ineffective to reduce the neutron energy due to the large mass and can simply attenuate the-γ-ray. In the case of polyethylene with 10% boron, on the other hand, the reaction process with neutrons is a little complicated. The neutron mainly reduces the energy through a collision with the boron and hydrogen, while a low-energy neutron captured by the boron and hydrogen emits a γ-ray with energy of 0.48 MeV and 2.2 MeV, respectively. Meanwhile, a low-energy γ-ray can be partly attenuated by the polyethylene. Here, it is attempted to estimate the effect of γ-rays on the CCD quantitatively based on the present data. If the noise count per γ-ray and neutron can be defined by η(γ) and η(n), respectively, the shielding efficiency is expressed by

$$K_0 = I_0(\gamma) \times \eta(\gamma) + I_0(n) \times \eta(n), \qquad (3)$$

where $I_0(\gamma)$ and $I_0(n)$ are the flux of γ-rays and neutrons, respectively. When the CCD is shielded by lead, the equation is rewritten by

$$K = I(\gamma) \times \eta(\gamma) + I(n) \times \eta(n), \qquad (4)$$

where $I(\gamma)$ and $I(n)$ are the flux of γ-rays and neutrons for the CCD shielded by lead.

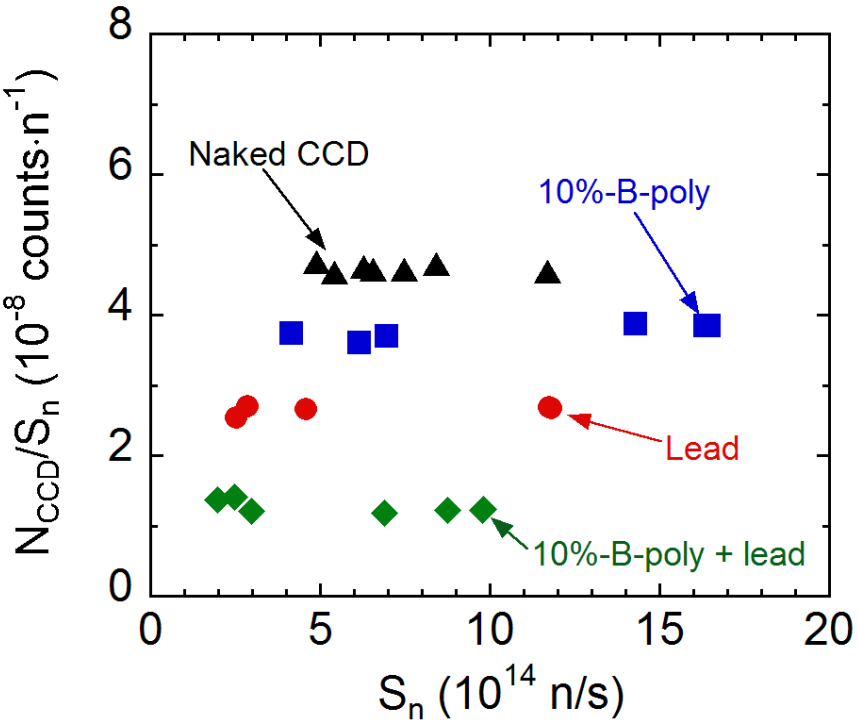

Fig. 6.6 Total noise count rate normalized by neutron production rate, N_{CCD} / S_n, against neutron production rate, Sn, for CCD without shielding (solid triangles) and shielded with lead (solid circles), polyethylene contained 10% boron (solid squares) and polyethylene plus lead (solid diamonds).

The attenuation of γ-rays is then calculated from the eq. (1) as

$$I(\gamma) = 0.19 \times I_0(\gamma). \qquad (5)$$

If the neutron has no collision in the lead, we obtain a relation of

$$I(n) = 0.84 \times I_0(n). \qquad (6)$$

The shielding efficiency ratio for lead is already obtained from the experiment as

$$K / K_0 = 0.5749. \qquad (7)$$

From the eqs. (3)-(7), thus, the ratio of noise count caused by γ-rays to the total noise count, $I_0(\gamma) \times \eta(\gamma) / K_0$, is determined to be 41% ± 5.5% and the ratio for neutrons, $I_0(n) \times \eta(n) / K_0$, is 59% ± 5.5%.

6.3.3 Reduction of signal noise

A lot of noise appears for all CCDs placed in the LHD laboratory during the D-D experiment. A reduction of the noise from the spectrum is attempted by the following method. A raw EUV spectrum at wavelength range of 270-320 Å from a single frame (5 ms exposure time) of the CCD data is shown in Fig. 6.7(a), which is measured with EUV_Long at t = 4.5 s in a deuterium discharge. It is not easy to identify an impurity emission line from the spectrum. When the spectrum is accumulated during t = 4.3-4.7 s as shown in Fig. 6.7(b), the randomly appeared noise can be averaged and a few impurity lines with relatively strong intensity become visible. For the comparison, a single frame spectrum measured at the same wavelength range in a hydrogen discharge is shown in Fig. 6.7(c). It is clear that both spectra are basically identical. Therefore, if the impurity line intensity is relatively strong, the present signal accumulation method is fairly effective for reducing the noise.

A reduction of the noise is also possible for the profile measurement with the sub-image mode CCD operation. A vertical profile of HeII at wavelength interval of 303.56 Å $\leq \lambda \leq$ 304.03 Å measured with EUV_Long2 at t = 4.5 s in a deuterium discharge is shown in Fig. 6.7(d). Many spike noises appear in the vertical profile. Figure 6.7(e) shows the same profile after removing the spike noise with a simple software programming by

directly connecting two nearby channels with local minimum counts. For the comparison, the HeII vertical profile at the same wavelength interval measured in a hydrogen discharge is also plotted in Fig. 6.7(f).

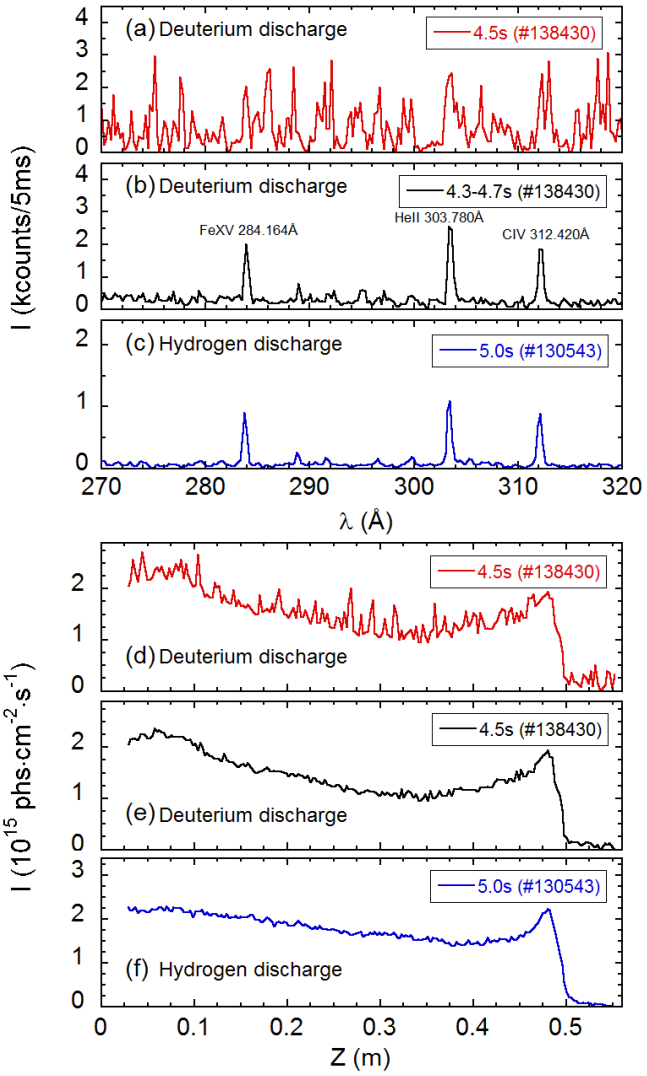

Fig. 6.7 (a) Raw EUV spectrum from a single CCD frame (5ms exposure) measured with EUV_Long at t = 4.5 s in deuterium discharge (#138430), (b) EUV spectrum averaged with 80 CCD frames during 4.3-4.7 s (#138430), (c) raw EUV spectrum from a single CCD frame measured at t = 5.0 s in hydrogen discharge (#130543), (d) vertical profile of HeII at 303.780 Å measured with EUV_Long2 at t = 4.5 s in deuterium discharge (#138430), (e) vertical HeII profile with software noise removal modified from (d) and (f) vertical HeII profile measured in hydrogen discharge (#130543).

6.4. Summary

An effect of noise caused by neutrons and γ-rays on CCD is examined in deuterium plasma experiments of LHD. The noise is analyzed for seven CCDs installed on VUV, EUV and X-ray spectrometers which are located at a different distance (7 m ≤ L ≤ 10.5 m) from the plasma center of LHD. The result indicates that the noise count per neutron decreases with the distance. The noise is also quantitatively examined using a special CCD placed in a shielding box made of 1.5 cm thick lead and 10 cm thick polyethylene containing 10% boron. Analyzing the noise obtained by changing the shielding material, it is found that the neutron contribution to the total CCD noise is larger than the γ-ray contribution, i.e., 59% for the neutron and 41% for the γ-ray. The radial profile measurement is not significantly affected by the noise because the intensity gradually changes against the radial position. The noise effect becomes more serious in the spectrum measurement. However, the spectrum with random spike noises can be improved, if several CCD frames are accumulated. Finally, we can conclude that the CCD used in the present study has entirely no permanent damage, at least, for the D-D experiment with totally 3.7×10^{18} neutron yields.

References

[1] R. Reimer et al., Rev. Sci. Instrum. 84, 113503 (2013).
[2] K.H. Burrell et al., Rev. Sci. Instrum. 72, 1 (2001).
[3] L. Zhang et al., Rev. Sci. Instrum. 86, 123509 (2015).
[4] W.H. Ko, H. Lee, D. Seo and M. Kwon, Rev. Sci. Instrum. 81, 10D740 (2010).
[5] T. Oishi et al., Plasma Fusion Res. 10, 3402031 (2015).
[6] M. B. Chowdhuri, S. Morita and M. Goto, Appl. Opt. 47, 135-146 (2008).
[7] M. B. Chowdhuri, S. Morita and M. Goto, Rev. Sci. Instrum. 78, 023501 (2007).
[8] C. Dong, S. Morita, M. Goto, and H. Zhou, Rev. Sci. Instrum. 81, 033107 (2010).
[9] S. Morita and M. Goto, Rev. Sci. Instrum. 74, 2375 (2003).
[10] P.A. Jaanimagi, R. Boni and R.L. Keck, Rev. Sci. Instrum. 72, 801 (2001).
[11] C. Hagmann et al., Proc. SPIE 8144, 814408 (2011).
[12] A. Huber et al., Fusion Eng. Des. 123, 669 (2017).

[13] M. Osakabe et al., Fusion Sci. Technol. 72, 199-210 (2017).
[14] T. Nishitani et al., Nucl. Sci. Technol., under progress.
[15] T. Ozaki et al., Rev. Sci. Instrum. 74, 1878 (2003).
[16] X. Huang et al., Rev. Sci. Instrum. 85, 043511 (2014).
[17] J.H. Hubbell and S.M. Seltzer, National Inst. of Standards and Technology-PL, Gaithersburg, MD (United States). Ionizing Radiation Div., 1995
[18] F.A.R. Schmidt, No. ORNL-RSIC--26. Oak Ridge National Lab., Tenn., 1970.

Chapter 7

Summary and Conclusion

ITER (International Thermonuclear Experimental Reactor), which is now under construction at Cadarache in France, is a next-generation tokamak device for fusion research aimed at carrying out D-T burning plasma experiments and the first operation is now scheduled in 2025. Materials for plasma-facing components (PFCs) in ITER must have a good capability of tolerating an extremely large thermal heat load, in addition to capabilities of reducing the erosion and tritium retention rates. Then, tungsten with a large atomic number of 74 is used as the most suitable material for the PFCs in the ITER tokamak instead of carbon materials which have been used for many years in toroidal devices. However, the line radiation loss from tungsten ions is very huge because of the large atomic number. Once the tungsten concentration exceeds a certain threshold level in the core plasma, the plasma performance is significantly degraded. In addition, heavy impurities such as tungsten tend to accumulate in the central plasma region due to the neoclassical effect. In the ITER operation, therefore, the tungsten density, n_W, must be maintained at a low level against the electron density, n_e, e.g., $n_W/n_e<10^{-5}$. The tungsten transport study is extremely important for controlling the tungsten accumulation in the plasma core and the tungsten influx in the plasma edge.

On the other hand, the tungsten diagnostics is also important for controlling the

tungsten buildup and accumulation. At present, however, understanding of the tungsten spectrum, which can provide unique information for the tungsten diagnostics and transport study, is still insufficient, while the spectrum and related atomic data for medium-Z impurities such as iron are well understood in conducting the impurity diagnostics based on numerous past works which have been done in both fields of plasma spectroscopy and atomic physics. Thus, the study on tungsten spectroscopy has been motivated in Large Helical Device (LHD) with graphite divertor plates and stainless steel first wall. Since the LHD discharge is totally tolerant for the impurity buildup due to the absence of the plasma current, the LHD experiment is possible over a wide range of tungsten concentrations. It resultantly leads to a high-brightness plasma source of tungsten line emissions. In LHD, the tungsten spectrum is observed by injecting a coaxial graphite pellet with a narrow tungsten wire because the use of a traditional laser-blow-off method is difficult due to the presence of a thick stochastic magnetic field layer surrounding the core plasma, by which the impurity screening is largely enhanced in the plasma peripheral region and the impurity flux toward the main plasma is reduced.

As a basis of the present thesis, tungsten spectra in extreme ultraviolet (EUV) range of 10-500 Å have been observed in LHD to identify the line emissions. All the tungsten spectra in the present thesis have been measured in neutral-beam-heated discharges using two grazing incidence EUV spectrometers called EUV_Short and EUV_Long working in wavelength ranges of 10-130 Å and 30-500 Å, respectively. A lot of tungsten lines from low-ionized ions of W^{4+}, W^{6+} and W^{7+} are observed for the first time in the toroidal device in addition to tungsten lines from highly ionized ions of W^{41+} - W^{45+}. Measured line emissions are carefully identified based on the NIST (National Institute of Standards and Technology) atomic spectra database and the wavelengths are accurately determined. The result is summarized in a table with information on line intensity and blended lines which is obtained by measuring the radial profile and analyzing the shape and peak position of the radial profile. The wavelength determined in the present study shows a good agreement with the NIST atomic spectra database.

Two space-resolved EUV spectrometers, called EUV_Short2 and EUV_Long2, have been utilized to observe the full vertical profile of tungsten line emissions by simultaneously measuring the vertical profile at upper- and lower-half plasmas of LHD, respectively. The radial profile of local emissivity is reconstructed from the measured vertical profile in the overlapped wavelength range of 30-130 Å. Up-down asymmetry is then examined against the local emissivity profiles of WXXVIII existing in the unresolved transition array (UTA) spectrum. The result shows a nearly symmetric profile, suggesting a good availability in the present diagnostic method for the impurity asymmetry study, while the up-down and in-out asymmetries have been observed for argon, nickel, tungsten, etc., in JET and Alcator C-mod

tokamaks. It is obviously confirmed from the observation of symmetric tungsten line emission profiles that the tungsten profile data obtained in LHD can be analyzed as a function of magnetic surfaces.

A series of experiments on tungsten spectroscopy have been carried out in LHD with tungsten pellet injection to study the tungsten spectra and to develop a method for the tungsten diagnostics. In particular, pseudo-continuum tungsten spectra called unresolved transition array (UTA) are very important for the diagnostics and transport study of tungsten ions in edge plasmas of ITER. However, understanding of the UTA spectra is still insufficient due to the complicated spectral structure. For the purpose, EUV spectra of UTA observed in the wavelength range of 15 Å to 70 Å are observed and analyzed at two different wavelength ranges of 15-45 Å and 45-70 Å, which mainly consist of $\Delta n = 1$, 2 and $\Delta n = 0$ transitions for $n = 4$ partially ionized tungsten ions, i.e. W^{18+}-W^{45+}, respectively. At first, the UTA line intensity is analyzed against central electron temperature at temperature recovery phase after the pellet injection to examine the presence of blended lines. Next, vertical profiles measured with two space-resolved EUV spectrometers are analyzed against electron temperature profiles for further precise investigation of the UTA spectra. For the analysis the local emissivity profiles are obtained from the measured vertical intensity profiles with Abel inversion method based on magnetic surface structures calculated by VMEC (Variational Moments Equilibrium Code) code. It is then possible to investigate the ionization stage of tungsten ions composing the UTA. As a result, it is found that the wavelength intervals of 49.24 Å $\leq \lambda \leq$ 49.46 Å, 48.81 Å $\leq \lambda \leq$ 49.03 Å and 47.94 Å $\leq \lambda \leq$ 48.15 Å, which are identified as W^{27+}, W^{26+} and W^{24+}, respectively, are applicable to the tungsten diagnostics. The result of the line component analysis on the tungsten UTA is summarized in tables.

Based on the radial profile measurement of W^{24+} (32.16-33.32 Å), W^{25+} (30.69-31.71 Å) and W^{26+} (29.47-30.47 Å) of which the wavelength interval is composed of only a single ionization stage, the ion density is evaluated. In order to evaluate the ion density, a photon emission coefficient for the W^{24+}, W^{25+} and W^{26+} ions is calculated using a collisional-radiative (CR) model. The chord-integrated radial profile of UTA lines is converted to the local emissivity profile based on Abel inversion technique. The tungsten density profile of W^{24+}, W^{25+} and W^{26+} ions is thus obtained from the local emissivity profile and the photon emission coefficient in addition to the temperature and density profiles. A detailed analysis of the obtained profile is done for the W^{24+} ion by investigating dependences on the electron density and the number of tungsten particles injected by the pellet. A total tungsten ion density, n_W, near $\rho = 0.7$ where the W^{24+} ion locates is also estimated from the W^{24+} ion density based on the fractional abundance in ionization equilibrium calculated with ADAS (Atomic Data and Analysis Structure) code. The tungsten density calculated with the photon

emission coefficient from the present CR model is roughly five times bigger than the tungsten density estimated from the pellet size, while the density calculated from a CL version of ADAS code is fairly close to the density estimated from the pellet size, i.e. difference within two times. A cascade process from higher excited levels may enhance the photon emission coefficient in the ADAS code calculation and resultantly the tungsten density calculated with the ADAS code is smaller.

As the supplement study, effects of neutrons and γ-rays on charge-coupled device (CCD), which is widely used as a detector of vacuum spectrometers in fusion devices, have been examined in deuterium plasma experiments of LHD. Totally 3.7×10^{18} neutrons have been yielded with energies of 2.45 MeV (D-D neutrons) and 14.1 MeV (D-T neutrons) during the deuterium experiment over four months. Meanwhile, the γ-rays are radiated from plasma facing components and laboratory structural materials in a wide energy range, i.e. 0.01-12.0 MeV, through the neutron capture. It is well known that these neutrons and γ-rays bring serious problems to the CCD system. Then, several CCDs of vacuum ultraviolet (VUV) / EUV / X-ray spectrometers installed at different distances from LHD plasma center are examined to study the effect of neutrons and γ-rays on CCD. An additional CCD placed in a special shielding box made of 10 cm thick polyethylene contained 10% boron and 1.5 cm thick lead is also used for the detailed analysis. As a result, it is found that the CCD has no damage in the present neutron yield of LHD, while the background signal noise integrated for all pixels of CCD largely increases, i.e. $1\text{-}3\times10^{8}$ counts/s. The data analysis of CCD in the shielding box shows that the background signal noise caused by the γ-ray is a little smaller than that caused by the neutron, i.e. 41% from γ-rays and 59% from neutrons. It is also found that the signal noise can be partly removed by an accumulation of CCD frames or a software programming.

In conclusion, EUV spectra from low-ionized tungsten ions, i.e. W^{4+}, W^{6+} and W^{7+}, are newly found in wavelength range of 260-500Å and tungsten UTA spectra are qualitatively and quantitatively investigated in detail. It is found that the wavelength interval of 32.16-33.32 Å, 30.69-31.71 Å and 29.47-30.47 Å is composed of a single ionization stage of W^{24+}, W^{25+} and W^{26+}, respectively. Tungsten density of these ions is demonstratively evaluated based on the radial profile measurement at the wavelength interval. Evaluated tungsten ion densities shows a good agreement with the tungsten density estimated from the pellet size. The result on tungsten spectroscopy in EUV range obtained through the present thesis study makes a valuable contribution to the edge tungsten diagnostics in ITER.

Acknowledgements

The doctoral thesis is the study result during three years at National Institute for Fusion Science (NIFS), Toki, Japan. The thesis is successfully completed with enormous helps from many people who I have met during my study. I would like to take this opportunity to deeply thank all these people.

First of all, I would like to express my deepest and most sincere gratitude to my supervisor, Prof. Shigeru Morita. His excellent guidance leads me to the field of the study on tungsten spectroscopy. His insightful suggestions frequently let me create new ideas when I do not find how to continue the study. His continuous encouragements make me firmly carry out my study plan. He has taught me the knowledges and skills in plasma experiments and scientific writings. I really appreciate all his suggestions and encouragements which really help me a lot. It has been a great fortune and happiness for me to study under his guidance, for example, always telling me to carry out the research study carefully and step-by-step. Furthermore, I am very thankful for his generous help in my private life in Japan. Without these help, I could hardly focus my attention on the study. At my whole life I will be benefited from his diligence and dedication in both work and life.

I am deeply grateful to Dr. Tetsutarou Oishi for his help in experimental works and suggestions for correcting my careless mistakes. He has also helped me in moving a heavy furniture to my apartment, and lent me an electric motorcycle. I wish to thank Prof. Izumi Murakami for a series of lectures on atomic physics. She has taught me how to use ADAS code and kindly helped me a method of calculating the photon emission coefficients of tungsten based on CR model which is extremely important for the tungsten density evaluation in my thesis work. I am sincerely thankful to Prof. Daiji Kato for his lectures on atomic physics. He has taught me the usage of HULLAC code, and calculated the photon emission coefficients of tungsten for comparison with those from ADAS code and CR model. I am also thankful to Prof. Motoshi Goto for his help during my experiment for examining the effect of neutrons and γ-rays on additional CCD.

I am sincerely thankful to my tutor, Dr. Hongming Zhang, for his help in my daily life during the first year in Japan, discussions on plasma spectroscopy and usage of several software programs for the analysis of experimental data. I also thank Dr. Xianli Huang for his help. He has told me a common sense in conducting experiments and usage of Andor

CCD software for controlling our spectroscopic instruments. He has kindly given me many suggestions in my study and daily life. I would also like to thank all my Chinese friends in NIFS for their friendships.

I wish to express my thanks to all members of LHD experiment group for their technical supports in LHD experiments on the impurity transport study. I also want to express my great thanks to staffs of NIFS and the Graduate University for Advanced Studies (SOKENDAI) for their supports.

Finally, I want to thank my parents and sister. Their supports and encouragements could give me great motivation to accomplish the present thesis work.

Publications

[1] "Up-down asymmetry measurement of tungsten distribution in large helical device using two extreme ultraviolet (EUV) spectrometers"
Y. Liu, S. Morita, X. L. Huang, T. Oishi, M. Goto and H.M. Zhang
Review of Scientific Instruments, **87** (2016) 11E308.

[2] "Component investigation of ionization stages on tungsten unresolved transition array spectra for plasma diagnostics based on space-resolved extreme-ultra violet spectroscopy in large helical device"
Y. Liu, S. Morita, X. L. Huang, T. Oishi, M. Goto and H. M. Zhang
Journal of Applied Physics, **122** (2017) 233301.

[3] "Observation of tungsten line emissions in wavelength range of 10 - 500Å in Large Helical Device"
Y. Liu, S. Morita, T. Oishi, M. Goto and X. L. Huang
Plasma and Fusion Research, **13** (2018) 3402020.

[4] "Effect of neutron and γ-ray on charge-coupled device for vacuum/extreme ultraviolet spectroscopy in deuterium discharges of Large Helical Device"
Y. Liu, S. Morita, T. Oishi and M. Goto
To be published in Review of Scientific Instruments.

[5] "Density evaluation of tungsten W^{24+}, W^{25+} and W^{26+} ions using unresolved transition array at 27-34 Å in Large Helical Device"
Y. Liu, S. Morita, I. Murakami, T. Oishi, M. Goto and X. L. Huang
To be published in Japanese Journal of Applied Physics.

[6] "Evaluation of tungsten cooling rate based on radial profiles of tungsten line emissions in EUV range of 10 to 500 Å"
Y. Liu, S. Morita, I. Murakami, T. Oishi, M. Goto and X. L. Huang
To be submitted to Nuclear Fusion